

Annual Report

Period Covered: January 1, 1981 through December 31, 1981

STUDY PROGRAM FOR ENCAPSULATION MATERIALS INTERFACE
FOR FLAT-PLATE SOLAR ARRAY

To

Jet Propulsion Laboratory
California Institute of Technology

for the

Encapsulation Task of the Flat-Plate
Solar Array Project

The JPL Flat-Plate Solar Array Project is sponsored by the U.S. Department of Energy and forms part of the Solar Photovoltaic Conversion Program to initiate a major effort toward the development of flat-plate solar arrays. This work was performed for the Jet Propulsion Laboratory, California Institute of Technology by agreement between NASA and DOE.

This report contains information proposed by the Science Center, Rockwell International, under JPL Subcontract 954739.

This report was prepared as an account of work sponsored by the United States Government. Neither the United States nor the United States Department of Energy, nor any of their employees, nor any of their contractors, subcontractors, or their employees, makes any warranty, express or implied, or assumes any legal liability or responsibility for the accuracy, completeness or usefulness of any information, apparatus, product or process disclosed, or represents that its use would not infringe privately-owned rights.

February, 1982

D.H. Kaelble, F.B. Mansfeld, M. Kendig

Science Center
Rockwell International
1049 Camino Dos Rios
Thousand Oaks, California 91360



Rockwell International
Science Center

N94-70575

Unclas

Z9/44 0185920

(NASA-CR-194273) STUDY PROGRAM FOR
ENCAPSULATION MATERIALS INTERFACE
FOR FLAT-PLATE SOLAR ARRAY Annual
Report, 1 Jan. - 31 Dec. 1981
(Rockwell International Science
Center) 112 p

of 112

TABLE OF CONTENTS

	<u>Page</u>
ABSTRACT.....	1
1.0 OBJECTIVES.....	2
2.0 SUMMARY.....	3
2.1 Atomic and Molecular Properties.....	3
2.2 Polymer Chemistry and Physical Properties.....	3
2.3 Polymer Chemistry and Mechanical Properties.....	4
2.4 Atmospheric Corrosion Models and Monitors for Solar Arrays...	4
2.5 AC Impedance Evaluation of Solar Cell and Module Properties.....	4
3.0 INTRODUCTION.....	6
4.0 ANALYTICAL MODELS.....	8
4.1 Atomic and Molecular Properties Model.....	8
4.2 Polymer Chemistry and Physical Properties Model.....	9
4.3 Polymer Chemistry and Mechanical Properties Model.....	9
5.0 EXPERIMENTAL.....	11
5.1 Atmospheric Corrosion Model and Monitor for Solar Arrays.....	11
5.2 Evaluation of Solar Cell and Module Properties by AC Impedance Measurement.....	11
6.0 CONCLUSIONS.....	13
7.0 RECOMMENDATIONS.....	14
8.0 NEW TECHNOLOGY.....	15
9.0 REFERENCES.....	16
ACKNOWLEDGEMENTS.....	17

TABLE OF CONTENTS

APPENDIX I:	Relations Between Atomic and Molecular Properties.
APPENDIX II:	Relations Between Polymer Chemistry and Physical Properties.
APPENDIX III:	Relations Between Polymer Chemistry and Mechanical Properties.
APPENDIX IV:	Atmospheric Corrosion Model and Monitor for Solar Arrays.
APPENDIX V:	Evaluation of Solar Cell and Module Properties by AC Impedance Measurements.

ABSTRACT

The early validation of a 20 year service integrity for the bonded interface in solar cell modules is an important requirement in the Low Cost Solar Array (LSA) project.

The first annual report (Science Center Report No. SC5106.22AR) outlines and implements a physical/chemical evaluation program for solar cell encapsulants. The results of computer controlled ultrasonic and optical/ellipsometric mapping for interfacial defect characterization in solar modules is summarized in the second annual report (SC5106.49AR). The development and validation of an atmospheric corrosion model and test plan for LSA outdoor service at the Mead, Nebraska, test site is presented in the third annual report (SC5106.86AR). Development of AC impedance as a method of evaluating solar cell and module properties and further development of corrosion models is summarized in the fourth annual report (SC5106.104AR).

In the present fifth phase of study summarized here emphasis is placed on the development of materials selection criteria for encapsulant bond integrity and more fully validating AC impedance methods for detecting early electrical malfunction in solar modules.

1.0 OBJECTIVES

The general objective of this phase of the program is to develop materials selection criteria and tests for corrosion protection and environmental durability of encapsulant interfaces in the Flat Plate Solar Array (FSA) project. The two specific objectives included in the present study are stated as follows:

1. Develop computer aided methods for materials selection and verify these methods relative to current corrosion and environmental durability models.
2. Complete development and verification of AC impedance methods for evaluating corrosion and early electrical degradation of solar cells and modules.

2.0 SUMMARY

2.1 Atomic and Molecular Properties

Computer aided methods are presented for estimating the energies of ionic-covalent chemical bonding, properties of the molecular crystalline state, and acid-base properties, surface interaction, and molecular dipoles. The primary objective of this atomic to molecular properties model is to provide direct numeric estimation of the chemical, environmental, and corrosion stability of metals, their oxides and protective encapsulants. The analysis of ionic-covalent bonding includes chemical bond energy, percent ionic character, and bond lengths. The molecular analysis includes calculation of heats of formation, molecular weight, molar and specific volumes. The analysis of acid-base interactions includes surface isoelectric point (in pH units), Coulomb adsorption energies, and surface dipole moments. This analysis includes new estimates for the bond energies of metallic elements. The adhesion and hydrophobic or hydrophilic properties of metal oxides is related to their acid-base character and consequent orientation effects on chemisorbed films.

2.2 Polymer Chemistry and Physical Properties

Methods are presented for computer assisted estimations of polymer specific volume V_p , solubility parameter δ , glass temperature T_g , and molecular weight between entanglements M_e . These properties are computed from 33 functional groups, ranging from methylene to sulfone, which can be combined to described the main chain and side chain structures of model linear polymers. The additional effects of molecular weight and cross linking upon glass transition temperature are computationally defined. The functional group properties are stored in computer memory and recalled by an interactive computer program which permits construction of the polymer repeat unit chemistry for both main chain and side chain structures. The computation then describes the above four physical properties for the infinite linear polymer in its amor-

phous glass state. This monomer-polymer prediction program is self-instructive and useful in qualitative exploration of chemical structure effects on polymer processability and performance.

2.3 Polymeric Chemistry and Mechanical Properties

A computer model is presented for direct estimation of time dependent modulus, strength, extensibility, and fracture toughness of polymers based on a description of chemical structure. The model analyses the above mechanical properties in simple shear and tension. Polymer-diluent interactions are defined and properties can be computed for varied temperature and time conditions of mechanical loading. Polymer density, solubility parameter, glass temperature, and interchain entanglement molecular weight are computed from functional group structures of the polymer repeat unit. Assignment of polymer molecular weight and crosslink density permits computation of the time dependent modulus functions for shear and tension. Appropriate integration of variable modulus and strain produces the computed stress vs strain curve and the fracture condition. The energy integral of the stress versus strain curve defines the fracture energy of the unnotched specimen.

2.4 Atmospheric Corrosion Model and Monitor for Solar Arrays

An atmospheric corrosion model and corrosion monitoring system has been developed for low cost solar arrays (LSA). The corrosion model predicts that corrosion rate is the product of the surface condensation probability of water vapor and the diffusion controlled corrosion current. This corrosion model is verified by simultaneous monitoring of weather conditions and corrosion rates at the solar array test site at Mead, Nebraska.

2.5 AC Impedance Evaluation of Solar Cell and Module Properties

It has been observed that AC impedance measurements made over a wide frequency range can be used to determine the electrical properties of photovoltaic solar cells. The occurrence of a distribution of time constants for

an array of cells indicates that one or more cells deviate significantly from the values of cells which operate properly. In some cases, such deviations have resulted from failure of leads. A model for the AC impedance of solar cells and validating experimental results are presented. AC impedance measurements show promise as an NDE technique for quality control of solar cell arrays.

3.0 INTRODUCTION

Several recent reports^{1,2} describe the current progress and challenges in photovoltaic encapsulation. As discussed in the Summary, this annual report presents five interconnected subject discussions with each subject documented as a self-contained technical article in the appendices to this report.

A major study effort this year has been development of a detailed materials selection criteria for encapsulant bonding and 20 year corrosion protection. This study has taken advantage of the previous modeling studies which are summarized in the previous annual report.³ This report presents these new analytical models which provide computer-aided methods for materials selection and property optimization. These three computer-aided models are developed as general purpose modules which are titled as follows:

- I. Atomic to Molecular Properties
- II. Polymer Chemistry to Physical Properties
- III. Polymer Chemistry to Mechanical Properties

The atomic to molecular properties model was developed under this program to provide new and detailed estimates of the bulk and surface properties of metal oxides and their interaction with encapsulants for corrosion protection. The two models for polymer chemistry have been developed outside this program but are included to form the critical links between interface properties and macroscopic integrity estimates of the bonded encapsulant in solar cells and modules.

In addition to the above three material selection models two additional models dealing specifically with solar cells and modules are appended to complete this discussion. These specific models are titled as follows:

- IV. Atmospheric Corrosion Model and Monitor for Solar Arrays.
- V. AC Impedance Evaluation of Solar Cell and Module Properties.

The appended reports on these subjects describe the current status of corrosion modeling and monitoring of electrical response of the solar cells and modules to detect early symptoms of environmental degradation.

The combination of these five models is intended to provide a continuous chain of analysis for the general laminate life prediction program illustrated in the logic flow diagram of Fig. 1 and discussed in earlier reports.³ In Fig. 1, a simple linear model is proposed which describes material property inputs at the top and composite system response in terms of reliability and durability at the bottom. Where it becomes too expensive, in cost or time requirements, to carry out the experimental measurement and analysis program listed on the right side of Fig. 1 the computer-aided models listed above become increasingly useful.

4.0 ANALYTICAL MODELS

As discussed in prior reports¹⁻³ the real difficulty in developing materials selection criteria for solar cells and encapsulant bonding is related to the diverse combinations of materials to be joined. Semiconductor materials, metals and their oxides and one or more polymer insulators normally meet at a common interface. The solution to the above problem of material diversity was obtained, in part, by computerizing the entire periodic table of the common elements in the atomic and molecular properties model.

4.1 Atomic and Molecular Properties Model

As discussed in Appendix I, a comprehensive table of the properties of 67 elements is organized and placed in computer memory. Chemical compounds involving any combination of these elements can be generated by the computer model and their molecular bulk and surface properties evaluated. As discussed in the last annual report, an important practical and theoretical questions are related to interfacial bonding for corrosion protection (see Ref. 3, Fig. 26). The acid-base bonding criteria of Bolger and Michaels⁴ is now incorporated as part of the numeric analysis of interface adsorption developed in Appendix I. As the discussion of Appendix I shows (see Appendix I, Figs. 7 and 8) the computed trihydroxy forms of the reactive silane coupling agents act as both strong acids and bases and are predicted to displace water from a wide range of oxide surfaces. This result agrees with experience⁴ and provides a detailed mechanistic explanation for this important property of silane coupling agents and their resistance to moisture.

Other computational examples of Appendix I illustrate a number of materials selection criterial relevant to solar arrays. The oxide bond energy and its ionic character determine in large measure their chemical stability and electrical properties. The oxide dilation factor as discussed in Appendix I has an additional controlling effect on corrosion protection properties of oxides.

4.2 Polymer Chemistry and Physical Properties

The acid-base bonding of reactive silanes to metal oxides is treated by Appendix I. Current theories and chemical analysis⁵ shows that the silanes also homopolymerize, crosslink and chemically react with the matrix or polymer encapsulant. Both the polymerization and physical properties of the coupling layer are capable of being modelled by the computer model of Appendix II. In Appendix II are listed 33 polymer structure units which include dimethylsiloxane. The chemical bonding of silane to the polymer encapsulant and the physical properties of the coupling layer can be estimated by the methods described in both Appendix II and Appendix III.

4.3 Polymer Chemistry and Mechanical Properties

As described in Appendix III the analysis of mechanical properties includes the estimate of strength, extensibility and fracture energy under uniform tensile or shear bonding. The effects of environmental aging are expressed in the mechanical analysis model through chemical composition, low molecular weight diluent, average molecular weight and crosslink density. In the life prediction program of Fig. 1 this branch of analysis culminates in the prediction of defects and cavity formation which introduces the detailed discussion of specific experimental studies of solar cells and solar arrays. The above three models are designed for use in conjunction with detailed laminate models for internal stress analysis and current-voltage (IV) response as is discussed in several related reports.^{2,3} on hydrothermal and radiation aging effects.

SC81-13600

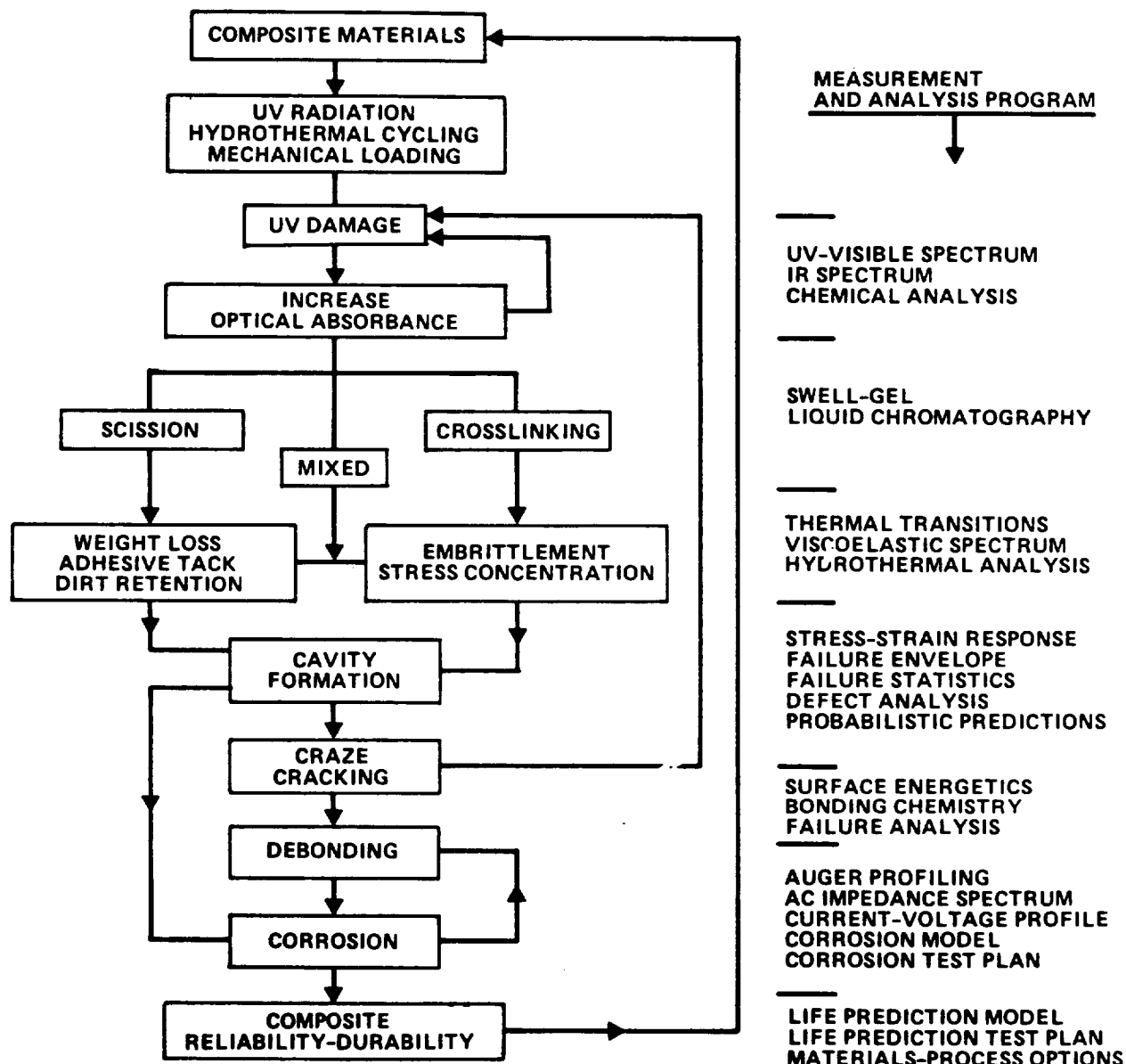


Fig. 1 General laminate life prediction program.

5.0 EXPERIMENTAL

Two areas of combined experiment and model development have been carried out in the current program. The current atmospheric corrosion model and monitor methodology are summarized in Appendix IV. The electrical evaluation of solar cell and module degradation by AC impedance is summarized in Appendix V.

5.1 Atmospheric Corrosion Model and Monitor for Solar Arrays

The still current model for atmospheric corrosion based on combined "time of wetness" and diffusion controlled corrosion current is summarized in Appendix IV. This discussion is now made much more specific by the analytic models discussed in Section 4. It has been shown this year that the atmospheric corrosion monitor (ACM) described in Appendix IV can be readily applied as a laboratory test method to determine relative measures of the corrosion protection values of thin coatings of encapsulant (generally <3.0 mils) which simulate the thickness of paint coatings. For thick coatings of 20 to 50 mils of highly protective encapsulant the ACM loses sensitivity as shown in the long term studies at Mead, Nebraska (see Appendix IV). The present results indicate that the ACM is a simple and direct test for thin coating corrosion protection as afforded by direct measure of the total corrosion current.

5.2 Evaluation of Solar Cell and Module Properties by AC Impedance Measurement

Experimental studies completed and summarized in Appendix V show that the appropriate combination of impedance modelling and measurement is quite informative in analyzing slight deviations from proper cell performance. In some cases, these deviations of impedance response relate to intrinsic cell degradation such as lowering of shunt resistance. In other clearly documented cases the deviations in impedance response relate to incipient degradation and

failure of interconnects between cells which modify and raise the series resistance of the module. The occurrence of a distribution of impedance time constants in an array of cells is a clear indication of defective cells and lowered power generating efficiency. AC impedance measurements continue to show promise as an NDE (nondestructive evaluation) technique for quality control of solar cell arrays.

6.0 CONCLUSIONS

Three new analytical models are introduced which provide materials selection criteria for solar cells and encapsulants which are based directly on chemical composition. These models are computer based and highly interactive. These material selection models permit a closer definition of the environmental design problem and the materials solution by direct consideration of the interactions of atomic and molecular properties with the environmental stress.

The atmospheric corrosion monitor (ACM) which is widely used in evaluating the corrosivity of environments (see Appendix IV) is shown to be a simple passive measurement for the corrosion protection of thin (≤ 3 mils) encapsulant films but insensitive to thick protective films (20-50 mils) which suppress the corrosion current below the level of detection.

AC impedance measurements continue to show promise as an NDE technique for quality assessment and control of solar cell arrays. The measurement has shown promise in following minor deviations of solar cell electrical properties induced independently by temperature and moisture. The measurement and analysis have now been extended to detect the electrical responses indicative of interconnect deterioration and incipient failure in solar cell modules.

7.0 RECOMMENDATION

The following specific recommendations in the area of encapsulant interface durability and corrosion protection are presented from this study:

1. The new materials selection models and criteria should be tested and validated with the goal of achieving long-term interfacial bonding stability of FSA photovoltaic encapsulation systems.
2. This materials selection study should include the development of methods for monitoring bond strength and stability under actual and accelerated outdoor aging.
3. The experimental program to measure and interpret corrosion and electrical degradation of single solar cells and interconnected cells should continue in support of validating material selection models and bond strength monitoring.
4. Guidelines for field instrument requirements and design of AC impedance measurements for solar modules should be defined.

8.0 NEW TECHNOLOGY

This study has developed and demonstrated new materials selection criteria. Chemically based computer models provide a new means of rapidly analyzing materials and numerically estimating environmental and long term aging response. AC impedance measurements and models continue to show promise as a quality control test for NDE (nondestructive evaluation) of solar cell arrays. Atmospheric corrosion monitors (ACM) are sensitive as a laboratory test for measurement of corrosion protection properties of thin encapsulant coatings.

9.0 REFERENCES

1. R. J. Cottshall and A. W. Czanderna, "Basic Research Needs and Opportunities on Interfaces in Solar Cells: An Executive Summary," J. of Metals (October 1981) p. 27.
2. W. Carroll, C. Coulbert, E. Cuddihy, A. Gupta, and R. Liang, "Photovoltaic Module Encapsulation Design and Materials Selection: Volume I, JPL Report No. DOE/JPL-1012-XX (Preliminary) Nov. 1, 1981.
3. D. H. Kaelble, F. B. Mansfeld, M. Kendig and C. Leung, "Study Program for Encapsulation Materials Interface for Low-Cost Solar Array," Annual Report for Period Jan. 1, 1980 through Dec. 31, 1980, Science Center Report No. 5106.104AR (February 1981).
4. J. C. Bolger and A. S. Michaels, "Interface Conversion (Editor: P. Weiss), Elsevier, Amsterdam (1968), Chap. 1.
5. C. H. Chiang and J. L. Koenig, Polymer Composites, 1(2), (1980), p. 88.

ACKNOWLEDGEMENTS

The authors wish to express their appreciation to the many individuals who contributed to this research and this report. At the Jet Propulsion Laboratory the helpful discussions and supply of test materials by P. Frickland and J. Repar were most helpful.

Edward Cuddihy is technical monitor of the subcontract for JPL and Cliff Coulbert of JPL is Manager of the Encapsulation Task of the Flat Plate Solar Array Project. Their helpful technical guidance is gratefully acknowledged.

APPENDIX I

RELATIONS BETWEEN ATOMIC AND MOLECULAR PROPERTIES

D.H. Kaelble

Rockwell International Science Center
Thousand Oaks, CA 91360

ABSTRACT

Computer aided methods are presented for estimating the energies of ionic-covalent chemical bonding, properties of the molecular crystalline state, and acid-base properties, surface interaction, and molecular dipoles. The primary objective of this atomic to molecular properties model is to provide direct numeric estimation of the chemical, environmental, and corrosion stability of metals, their oxides and protective encapsulants. The analysis of ionic-covalent bonding includes chemical bond energy, percent ionic character, and bond lengths. The molecular analysis includes calculation of heats of formation, molecular weight, molar and specific volumes. The analysis of acid-base interactions includes surface isoelectric point (in pH units), Coulomb adsorption energies, and surface dipole moments. This analysis includes new estimates for the bond energies of metallic elements. The adhesion and hydrophobic or hydrophilic properties of metal oxides is related to their acid-base character and consequent orientation effects on chemisorbed films.

Introduction

Extensive tabulations of the chemical and physical properties of metallic and polymeric materials are limited to the major classes of commercially important materials. Very often the chemist or materials specialist wishes to obtain a qualitative estimate of corrosion or environmental durability which is developed directly by writing the chemical structure of the material. In this discussion the homonuclear bond energies of metals are estimated from their heats of vaporization and combined with the Pauling values of single bond energy for nonmetallic elements. The table of elemental properties is stored in computer memory and automatically retrieved by the computer program for estimating chemical and physical response of chemical compounds.

Elemental Properties

The elemental properties for the 67 elements included in this study are listed in Table 1. The first column of Table 1 lists a code number which is employed as a retrieval number in the computer program. The second and third columns of Table 2 identify the atomic number and chemical symbol of the element. The right seven columns of Table 1 tabulate the elemental properties utilized in the computation. From left to right these properties are defined as follows:

- W = atomic weight
- D = single (2 electron) bond energy
- X = electronegativity
- R = atomic covalent radius
- V = most stable valence
- MV = maximum valence
- $S = MV/R$ = the ionic potential relating to acid-base properties.

All of the above properties of the elements are taken from a recent version of the periodic table¹ with the exception of the single bond energy D . The single bond energies for the nonmetallic elements in Table 1 are based upon values reported by Pauling.² The apparent bond energies for the metals are obtained by a modification of a convention applied by Vijn³ in the following relation:

$$D(M-M) = \frac{2\Delta H_S}{C.N.} \quad (1)$$

where $D(M-M)$ is the metal-metal bond energy, ΔH_S is the heat of sublimation (sum of the heats of melting and vaporization) and C.N. is the maximum lattice coordination number of the metal. The factor $2/C.N.$ in Eq. (1) corrects for the fact that each bond would otherwise be counted twice in the simple summing of all nearest neighbor interactions. Inspection of the bond energies listed by Vijn³ indicates what appear to be values with too low a magnitude for metal bond energies.

An alternative form of Eq. (1) can be written to incorporate the cohesive energy density δ^2 and molar volume V_m of metals as follows:

$$D(M-M) = \frac{2 \delta^2 V_m}{C.N.} \quad (2)$$

where extensive listings of both δ^2 and V_m for metals are compiled by Hildebrand.⁴ A comparative listing of single bond energies for ten elements are shown in Table 2 where the first column summarizes single bond energies of Pauling.² The second column provides calculated values from Eq. (2) for an assumed maximum coordination number C.N. = 12. The notable feature of Table 2 is that the Pauling values of bond energy are higher than the estimates of Eq. (1) or Eq. (2) by a nearly constant multiplier factor which appears in the

right column of Table 2. This result implies that a chemical coordination number of C.N. = 3 to 4 is more appropriate in calculating chemical bond energies by Eq. (2).

This result was applied to provide the calculated values of metal bond energies in Table 1. Where Pauling values of bond energy were not available the cohesive energy density δ^2 and molar volume V_m data of Hildebrand were applied in Eq. (2) with a chemical coordination number $C = 3$ for elements of Groups IA-VIA and $C = 4$ for elements of Groups VIIA-VIIIA and IB-VB of the revised periodic table.¹ These provisional values of metal single bond energy are parenthesised in Table 1 to distinguish them from the Pauling reference values.

Ionic-Covalent Bonding

Having a complete listing of homonuclear bond properties as presented in Table 1 permits application of the Pauling relations for calculation of heteronuclear single bond energy $D(A-B)$ and percentage ionic character (%I). The ionic component of single bond energy $I(A-B)$ is defined by the following standard relation:²

$$\Delta_{AB} \text{ (kJ/mol)} = 96.5 (x_A - x_B)^2 \quad (3)$$

The total single bond energy D_{AB} between atoms A and B is defined as the sum of the covalent and ionic bond energies by the following standard relation:²

$$D_{AB} \text{ (kJ/mol)} = 0.5(D_A + D_B) + \Delta_{AB} \quad (4)$$

The percent ionic character $I(\%)$ of the single bond energy is calculated from the ratio of Eq. (1) and Eq. (2) as proposed by Kaelble:⁵

$$I(\%) = \frac{100 \Delta_{AB}}{D_{AB}} \quad (5)$$

The more standard approach is to define the percent ionic character of the single bond energy purely from electronegativity differences by the following standard relation:^(1,2)

$$I(\%) = 100 \{1 - \exp [-0.25 (X_A - X_B)^2]\}$$

The obvious deficiency of the above expression is, of course, that no information on total bond energy is contained in the relation. A comparison of experimental and calculated values of %I for 18 diatomic compounds with experimental values of $I(\%) = 4$ to 92 shows that Eq. (5) provides an improved agreement with experiment.⁵ Consequently, Eq. (5) is incorporated in the computer program of this analysis.

The calculation of single bond length L_{AB} utilizes the standard Shoemaker-Stevenson relation as follows:^{2,6}

$$L_{AB} (10^{-10} \text{ m}) = R_A + R_B - 0.09 |X_A - X_B| \quad (6)$$

The absolute difference in electronegativities is shown by Eq. (6) to reduce the single bond length relative to purely covalent bonding. Values for both covalent radii R and electronegativity are tabulated in Table 1.

Due to the importance of molecular nitrogen N_2 and molecular oxygen O_2 in many chemical reactions the atomic properties of these molecules are described after the elements as Code No. 68 and 69. For the purpose of elemental computations the triple bond energy of N_2 of $D_{N_2} = 946$ kJ/mol is divided by 2 for the elemental constituent $(N_2)/2$ shown in Table 1 and the elemental radius is taken as one-half the triple bond length $L_{N_2} = 1.10 \cdot 10^{-10}$ m. Equivalently the elemental bond energy and radius of $(O_2)/2$ is taken as one half the double bond energy $D(O_2) = 404$ kJ/mol and bond length $L(O_2) = 1.24 \cdot 10^{-10}$ m. This convention makes allowance for the loss of resonance energy and increase in bond length on conversion to singly bonded states.

Molecular Analysis

A computer program has been written to provide a simple chemical and physical analysis of chemical compound structures. The program first inputs a description the compound in terms of the number of moles N_i of each of the elements which is equivalent to writing the empirical chemical formula. The program then inputs a complete description of the number of moles N_{AB} of each of the chemical bonds and the A and B elements for each bond which is equivalent to writing a chemical structure formula. The individual bond properties are calculated by means of Eq. (1) through Eq. (4). The total bond energy is obtained by summation:

$$U_T = \sum N_{AB} D_{AB} \quad (7)$$

The molecular weight is determined by a summation of the elemental constituents with the following expression:

$$W_T = \sum N_i W_i \quad (8)$$

A defect free lattice formed by N moles of homogeneous atomic units all with uniform chemical bond length L_{AA} has a volume V which is defined by the following relation:⁵

$$V = \frac{N_0 (N_i L_{AA}^3)}{C}$$

where $N_0 = 6.023 \cdot 10^{23}$ is Avogadro's number and C is a lattice packing factor which varies with lattice type as shown in Table 3. The volume of a lattice with a mixture of chemical bond lengths will be approximated by summing the partial volumes for each fraction of bond types. An appropriate expression for calculating a compound lattice of mixed elements and chemical bonds is given as follows:

$$V_m = \frac{N_0 \sum N_i}{C} \frac{\sum (N_{AB} L_{AB}^3)}{\sum N_{AB}} \quad (9)$$

and the specific volume V_s is computed by the ratio of Eqs. (8) and (9) as follows:

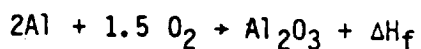
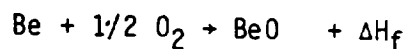
$$V_s = V_m / W_T \quad (10)$$

The cross plot of homonuclear bond energy D_{AA} vs elemental electronegativity shown in Fig. 1 provides a summarizing illustration of the distribution of the elemental properties from Table 1 relative to ionic-covalent bonding.

The data display in Fig. 1 is referenced to the atomic properties of hydrogen by the dashed horizontal and vertical curves. Elements with electronegativity less than $Z < 2.2$ are metallic and elements with $Z > 2.2$ are semi-metallic or nonmetallic. Chemical compounds formed between metallic and

nonmetallic elements, as indicated by Eq. (3), become increasingly ionic with the increased separation of X_A and X_B and this property is easily visualized by the horizontal separation of data points in Fig. 1. The covalent bond energies D_{AA} shown on the vertical axis of Fig. 1 define many properties of the metallic elements such as melting point, elastic modulus, hardness, and abrasion resistance.³ As shown in Fig. 1 only three refractory metals, tantalum Ta, niobium Nb, and tungsten W display D_{AA} values greater than hydrogen H. One notes in Fig. 1 no particular trends between D_{AA} and electronegativity X indicating that these are essentially independent material selection properties of the elements.

Some of the useful outputs of the computer program are illustrated in the computations shown in Fig. 4 for the energy (or heat) of formation of oxides from their elements. The computations illustrate the following chemical reactions:



where ΔH_f is the heat of formation (negative for stable product). The properties of the elements as stored in Table 1 are presented at the top of each example in Table 4. The appropriate disappearance of the homonuclear bonds is shown by the negative moles and the production of the reaction product by positive moles. The total bond energy computed by Eq. 7 sums over both negative (bonds broken) and positive (bonds formed) moles of bonds to obtain the net energy $U_T = -\Delta H_f$ of formation. As shown in Table 4 the computer model also reports the bond energy, % ionic character, and bond length for each component of the above chemical reactions.

Table 5 compares calculated and reference values of the heats of formation for ten metal oxides. The right column records the differences. The sum of the differences is seen to be small indicating no large tendency to either over or under estimate the heat of formation. The standard deviation of $\pm 2.04 \cdot 10^5$ J/mol which is about 40% of the hydrogen single bond energy appears typical of this simple calculation.

Table 6 compares calculated and reference values of the heats of formation for metal chlorides. The differences in calculated and reference energies are similar to the oxides. Accepting these qualitative results one has available a simple method of computing the chemical bond properties for an enormous range of chemical compounds.

In characterizing the corrosion protection properties of oxides one important parameter is the oxidation dilation factor ϕ for various metals as defined in Table 7. The oxidation dilation factor ϕ was introduced by Pilling and Bedworth⁸ as an important corrosion resistance index of metals. When $\phi < 0.7$ the oxide film is in tension and cracks. Conversely when $\phi > 2.0$ the oxide film is under compression and tends to blister and peel from the substrate metal. The computer program, by Eq. (9), estimates molar volume V_m of both metals and oxides and this permits a rapid evaluation of ϕ .

The right columns of Table 7 report experimental values of molar volumes for various oxides and their characteristic ϕ values.^{8,9} The left columns of Table 7 report the calculated values of molar volume for metals, their oxides and the computed estimate of ϕ . These computations represent a maximum coordination number $Z = 12$ for both metal and oxide so as to minimize both V_m and ϕ . One notes a consistent and agreeable trend between the calculated and experimental values of ϕ . Oxides tend to display lower coordination numbers than their parent metals. With the four high ϕ oxides in lower Table 7 assuming a $Z = 6$ for the oxide would double the calculated values of ϕ to provide good agreement with experimental data. The computer program calculates values of V_m for $Z = 12, 8, 6$, and 4.

Acid-Base Interactions

Many adhesion and corrosion properties of metals are dominated by the acid-base interactions of the metal oxide which covers all metals, except gold, under ambient atmospheric exposure. As pointed out by Parks¹⁰ and Bolger and Michaels,¹¹ experience shows that different metals and their oxides display widely differing types of interactions with adhesives and corrosive environments based upon the isoelectric point (IEP) or zero point of surface charge (ZPC) under aqueous immersion. The IEP or a surface is defined as the $\text{pH} = -\log [\text{H}^+]$ where the immersed oxide surface has zero net surface charge due to equivalent concentrations of positive (cation) and negative (anion) complexes.

In this discussion the objective is to develop specific relations for coulombic charge displacement between atoms A and B. Atom A is defined as more electropositive than atom B. In the ionized state atom A will act as Lewis acid (A = electron acceptor or cation) and B is a Lewis base (B = electron donor or anion). Through the use of a simple electrostatic model for coulombic interactions Parks derives a two parameter model for IEP with the following relation:¹⁰

$$\text{IEP} = \text{pH} = C_1 - C_2(V/R_I) \quad (11)$$

where V is the metal cation valence, R_I is the "effective" ionic radius of the oxolated cation, and C_1 and C_2 are constants. The ratio (V/R_I) termed the ionic potential was introduced by Cartledge¹² and, as indicated in a review by Moeller,¹³ has found broad applications in evaluations of atomic contributions to acid-base properties. A comprehensive review of IEP values for solid oxides, solid hydroxides, and aqueous hydroxylated oxides by Parks¹⁰ shows the characteristic ranges of acid-base properties summarized in Table 8.

The essential form of Eq. (11) and the data summary of Table 7 follows from the standard Coulomb equation:¹⁰

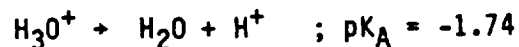
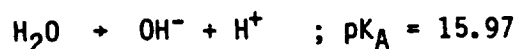
$$U_E = - \frac{dF}{dL_{AB}} = \frac{M N_O V_A V_B \epsilon^2}{D L_{AB}} \quad (12)$$

where U_E is electrostatic potential energy, F is the Coulomb electrostatic force, and L_{AB} is the distance separation of cation A and anion B. The moles of acid-base bonds per mole of adsorbate is M and N_O is Avagadro's number, V_A and V_B are the respective cation and anion valences, D the dielectric constant of the medium and ϵ the charge of the electron.

A combined consideration of the Coulomb equation and Eq. (11) provides a new empirical form for Eq. (11) as follows:

$$IEP = pH = 16.0 - 3(V/R) \quad (13)$$

where V is atomic valence and R is covalent radius as listed in Table 1. In Eq. (13) the limits of IEP are bounded by the following ionization properties of ambient water:¹³



which tend to limit the acid-base responses of solvated ions. The atomic properties of the hydrogen cation with $V/R = 3.13$ provides a value of $IEP = 6.61$ for a neutral surface as represented for the bulk ambient state of

water with pH = 7.0. Application of the covalent radius R and the maximum valence $V = MV$ values of Table 1 in Eq. (13) will tend to emphasize the specific acidic-base properties of the elements relative to hydrogen. For this extreme case of highest oxidation state Eq. (13) will describe the minimum IEP as follows:

$$\text{IEP} = \text{pH} = 16.0 - 3S \quad (14)$$

where the atomic values of $S = MV/R$ are listed in the right column of Table 1.

A plot of $S = MV/R$ vs electronegativity X for the elements is shown in the data display of Fig. 2. Despite a broad scatter of the data one notes an underlying trend of increasing S and related oxide acidity with increasing electronegativity. The dashed horizontal and vertical curves of Fig. 2 again reference the atomic properties of hydrogen and the pH of water as a reference. Of special reference and importance in the adhesion and corrosion properties of the metal oxides are those metals of intermediate electronegativity $X = 1.4$ to 2.6 which show high or low values of S and which display extremes of acidic (high S) or basic (low S) surface properties.

These extreme values of S for the elements are more clearly shown in Fig. 3 when plotted as a function of atomic number. The dashed horizontal curve of Fig. 3 represents the neutral properties of hydrogen with $S = 3.13$ forming the dividing line between elemental acid or base character. One notes with interest in both Fig. 2 and Fig. 3 that acidic elements with $S > 5$ and of intermediate electronegativity $X = 1.4$ to 2.2 are restricted to four which are chromium Cr, manganese Mn, technetium Tc, and rhenium Re. The high oxidation state chromates such as zinc chromate are commonly used as corrosion suppressing pigments and this function may be primarily due to strong acid-base interaction with neutral or basic oxides such as formed on iron, steel, aluminum and titanium. Manganese which forms a strongly acidic oxide is commonly used as an alloying constituent in copper, brass and bronze alloys which are subject to marine applications and salt water corrosion. Manganese is

considered as an excellent deoxidizing agent for steel manufacture. Technetium is informally reported to have exceptional corrosion properties with essential immunity to salt water corrosion and an unique resistance to barnacle growth in marine environments.¹⁴

According to the definitions applied here all metals in the metallic state $V = 0$ are strongly basic and strong electron donors. Metals with a low maximum valence $MV < 2$ remain strongly basic in their fully oxidized state as shown in the plots of Fig. 2 and Fig. 3. Metals of intermediate electronegativity $Z = 1.4$ to 2.2 and low $S < 2$ tend to form basic oxides which are hydrophobic and electrically conductive. The extensive use of copper oxide as a hydrophobic substrate in lithography is well known. The oxides of zinc, copper, and silver, all tend to display hydrophobic character and semi-conductive properties. One notes that lead (Pb) and gold (Au), although of higher electronegativity, tend to fit this latter category of definition and particularly in their lower valence states.

The general qualitative validity of Eq. (13) and Eq. (14) is shown in the three examples illustrated in Figs. 4 through 6. In Fig. 4 is plotted the reference pH values of concentrated acids and bases⁷ vs the ratio of MV/R for the cation as listed in Table 1. The dashed curve is the predicted relation of Eq. (14) which shows a reasonable correlation with experimental data.

Figure 5 plots data from Moeller¹³ for a wide variety of aqueous dissociation constants as $pK_A = pH$ where the principal anion or cation is not necessarily in its maximum valence state. For example, sulphur has a valence $V = -2$ in hydrogen sulphide (H_2S) and $V = +6$ in sulphuric acid (H_2SO_4). Also shown are several valence states for iodine where $V = +1$ in HIO and $V = +5$ in HIO_3 and $V = +7$ in H_5IO_6 . These data indicate a reasonable correlation with the dashed curve of Eq. (13) where the valence V is assumed variable.

Figure 6 plots a number of the dissociation states of phosphorous and phosphoric acids as reported by Moeller¹³ to illustrate the broad range of $pK_A = pH$ and apparent cation valence states that are available in some hydrated oxides with multiple valence states. The extensive review listings

of IEP data by Parks¹⁰ also indicates that the acid-base properties of metal oxides can display widely varied values of surface pH which evidently depend on metal oxidation states and surface morphology. The data of Fig. 6 thus illustrate the important idea that a metal oxide surface can display a spectrum of acid-base characteristics which are bounded by a maximum acid character and minimum pH characteristic of MV/R.

Surface Adsorption

As an excellent brief review of corrosion resistance materials by Hoar¹⁵ points out, the acid-base character of the oxide is one of a number of important variables in corrosion protection. A simple approach to estimating the acid-base character of molecular adsorption to metals and their oxides is available by a special use of the Coulomb energy calculation as defined by Eq. (12). By appropriate substitution of physical units we can rewrite Eq. (12) in the following special form:

$$U_M \left(\frac{\text{kJ}}{\text{mole}} \right) = \frac{12.2 M V_A V_B}{R_A + R_B} \quad (15)$$

Our objective is to calculate the maximum value of U_M characteristic of the limit of close approach of cation A and anion B. We assume the dielectric constant D of Eq. (12) is $D = 1.0$ and L_{AB} is the sum of the covalent radius so that $L_{AB} = R_A + R_B$ with R values from Table 1. Applying the classical values of valence for hydrogen bonding in water where $V_A = 1$ for hydrogen and $V_B = 2$ for oxygen and $R_A + R_B = 0.32 + 0.73 = 1.05 \cdot 10^{-10}$ m the energy U_M for a single hydrogen bond where $M = 1$ is $U_M = 23.2 \text{ kJ/mol} = 5.5 \text{ kcal/mol}$. This computed U_M value is in reasonable agreement with experimental values for the H-bond energy of bulk water of 5.0 kcal/mole .⁵ The O-H- -O bond length of $1.99 \cdot 10^{-10}$ m produced by this simple calculation is, of course, less than the experimental length determined for the hydrogen bond in bulk water where the O-H- -O hydrogen bond length is $2.76 \cdot 10^{-10}$ m.⁵

Recognizing that Eq. (15) calculates an upper estimate for the Coulomb energy a second relation which estimates the nominal Coulomb energy U_N can be written as follows:

$$U_N \left(\frac{\text{kJ}}{\text{mol}} \right) = \frac{12.2 \text{ M } (\sum V_A I_A) (\sum V_B I_B)}{R_A + R_B} \quad (16)$$

where $\sum V_A I_A$ and $\sum V_B I_B$ appropriately sum the product of valence and ionic character for each bond within the molecule to reflect the fractional ionic character of molecular structures. Using Eq. (16) the two O-H bonds of water, would produce a sum $\sum V_A I_A = 0.341$ for each H atom and $\sum V_B I_B = 0.682$ for the oxygen atom. The resulting nominal Coulomb energy is $U_N = 2.70 \text{ kJ/mole}$ for the single hydrogen bond in water. Equation (16) thus provides a more conservative estimate of electrostatic bonding which appropriately becomes $U_N = 0$ when either the acid or base are purely covalently bonded.

Estimates of the valences of U_M and U_N between various adsorbates and substrates can be readily calculated using Eq. (15) and Eq. (16). The upper portion of Table 9 illustrates model monobase and diacidic orientations of water on five substrate oxides. The lower portion of Table 9 tabulates the calculated values of U_M and U_N . We would expect the actual orientation (acid or base) of water is the orientation which gives the highest respective value of U_M or U_N . The calculations indicate the diacid conformation of water on Ag_2O and CuO which are basic oxides. The values of U_M and U_N become nearly equivalent for the acid and base interaction of water on neutral Fe_2O_3 indicating no strong molecular orientation effect. However, an acidic SiO_2 and CrO_3 the calculation shows that the monobasic interaction with water is favored.

Different adsorbate molecules can be represented by these calculations as shown respectively in Tables 9-11 for ammonia, chrome oxide, and an organic silanetriol. Ammonia represents a cleaning agent often added to water. Chromium trioxide is a common corrosion suppressing pigment

constituent. The trihydroxy silane is a postulated intermediate form of trimethoxy silanes commonly employed as adhesion promoters which suppress corrosion and increase adhesive bond strength in the presence of high moisture.¹¹ By noting only the higher of the U_M values for acid or base oxidations of the adsorbates of Tables 9 through 12 we can plot U_M vs $S = MV/R$ for the five substrate oxides. The curves of Fig. 7 show the variation of U_M for each adsorbate. Chromium trioxide adsorbate displays the highest U_M estimate and, by inference, would be expected to displace the other adsorbates from the substrate oxides. The transition from acid to base orientation of the adsorbate is indicated by the change in slope of each curve. Both ammonia and the silanetriol are predicated to displace water from neutral or acidic substrates such as Fe_2O_3 , SiO_2 , and CrO_3 but not from basic oxides such as Ag_2O and CuO .

The curves of Fig. 8 show the trends of adsorption predicted by the appropriate selection of nominal Coulomb U_N values for acid-base interactions as calculated by Eq. (16). The curves of Fig. 8 show that applying the covalent-ionic criteria for available valence not only lowers the bond energies but shows ammonia NH_3 is more weakly bonded than water H_2O to all five substrates. The trihydroxy silane and chrome oxide are estimated to bond more strongly than water. The inference to be drawn based on the curves of Fig. 8 is that both chromium trioxide and trihydroxy silane should displace water from both basic (low V/R) and acidic (high V/R) oxide surfaces as is concluded from numerous studies of adhesion¹¹ and corrosion.¹⁵

Molecular Dipole Properties

A set of simple relations permits the numeric estimation of molecular dipole properties directly from atomic properties. The absolute value of the dipole moment μ_{AB} for a chemical bond is approximately expressed by the following relation:¹⁶

$$\mu_i = 4.8 L_{AB} I_{AB} \quad (16)$$

where L_{AB} is bond length as defined by Eq. (6) and I_{AB} is the fractional ionic character of chemical bond as defined by Eq. (5). As discussed by Hedvig,¹⁶ the effective dipole moment of the rigid molecular $\bar{\mu}$ can be readily calculated from the individual bond moment componens μ_{xi} , μ_{yi} , μ_{zi} along cartesian coordinates x, y, z by the following relation:

$$\bar{\mu} = \left[\sum_{i=1}^n \mu_{xi}^2 + \sum_{i=1}^n \mu_{yi}^2 + \sum_{i=1}^n \mu_{zi}^2 \right]^{1/2} \quad (17)$$

A simple and extraordinary sensitive measurement for molecular adsorption at surfaces involves the measurement of surface potential difference ΔV . Bewig and Zisman¹⁷ discuss the effects of adsorbed films on ΔV as defined by the classical Helmholtz relation:¹⁷

$$\Delta V = \frac{4\pi\bar{\mu}_p}{A} = \frac{4\pi}{A} \sum_{i=1}^n \mu_{yi} \quad (18)$$

where $\bar{\mu}_p$ is the effective molecular dipole moment perpendicular to the substrate surface and A is the area per molecule in the close packed adsorption layer. By defining the y axis perpendicular to the surface as shown in Eq. (18) it is evident that ΔV can be numerically estimated from the bond properties described in Eq. (16). This calculation is not demonstrated but is an obvious extension of the surface analysis of molecular adsorption shown in Tables 9 through 12. The bond dipole moments for all the acid-base bonds are calculated by Eq. (16) and included in the data summary of Table 13. The charge orientation of each dipole is, of course, defined easily from electronegativities. The additional information required to solve Eq. (17) or

Eq. (18) is, of course, the individual bond angles and orientations which are not available directly from Table 1.

Summary and Conclusions

This discussion has introduced and demonstrated a computer aided model for creating and evaluating molecular compounds, acid-base characterization, surface adsorption energies, and molecular dipole properties which characterize the adsorption layer. The illustrative examples developed by computations from atomic properties show reasonable qualitative agreement with experiment. The real power and versatility of the model discussed here is, of course, the extreme wide range of materials that can be numerically evaluated by this method. This same observation applies to the numeric investigation of surface chemical processes such as oxidation, surface adsorption, and molecular dipole response.

The fundamental question of valency, bond ionicity, and bond length estimation are presently very lively subjects of research and discussion.¹⁸⁻²¹ Inspection of Table 14 which compares the current (1980) revised estimates¹ of electronegativity with the earlier Pauling² estimates shows that the properties of some elements such as tungsten W (AT.NO = 74) have been substantially redefined. This process of revision of atomic properties is, of course, improved by computer models such as discussed here. A recent review by Morgan²² provides an excellent discussion and recent bibliography of this broad subject as it relates to analysis of chemical bonding in ceramics.

The transcending importance of achieving corrosion resistant interfaces and stable long term adhesive bonding is defined in a recent review of basic research needs on interfaces in solar energy conversion systems (SECS).²³ Present energy needs of the United States, about 85 quads, would require exposure of 73000 km² (28000 sq miles) of solar collectors operating at 20% efficiency. Economics require a stable and non-degrading performance life of about 30 years. The computer assisted model discussed here was developed as part of a research program to develop long term environmental

durability and corrosion protection in polymer encapsulated photovoltaic SECS. Related computer based models for selection of polymer chemistry are discussed in separate reports.^{24,25} The combination of the three computer aided models are as follows: (1) atomic and molecular properties (discussed here), (2) polymer chemistry and physical properties, and (3) polymer chemistry and mechanical properties. The objective of these models is to provide for numeric estimation of bulk and interfacial properties of materials directly from chemical composition and chemical structure. The computer aided models add great speed and convenience to these numeric analysis and property evaluations.

Acknowledgment

This research was supported, in part, by the Flat Plate Solar Array Program of the U.S. Department of Energy through Jet Propulsion Laboratory, Pasadena, subcontract No. JPL-954739. The author gratefully acknowledges helpful discussions with Drs. T. Smith and P.E.D. Morgan during the development of this discussion.

References

1. "Table of the Periodic Properties of the Elements," Sargent-Welsh Scientific Co., Skokie, Ill. (1980).
2. L. Pauling, "The Nature of Chemical Bond," 3rd ed., Cornell University Press, Ithaca, N.Y. (1960)
3. A.K. Vijh, J. of Material Sci. 10, 998 (1975).
4. J.H. Hildebrand and R.L. Scott, "The Solubility of Nonelectrolytes," 3rd ed., Reinhold, New York (1950).
5. D.H. Kaelble, "Physical Chemistry of Adhesion," Wiley-Interscience, New York, Chap. 1, 2, 5 (1971).
6. V. Shoemaker and D.P. Stevenson, J. Am. Chem. Soc. 63, 37 (1941).
7. Handbook of Chemistry and Physics, 54th ed, CRC Press, p. D-61, D-114 (1973).
8. N.B. Pilling and R.E. Bedworth, J. Inst. Met. 29, 529 (1923).
9. O. Kubaschewski and B.E. Hopkins, "Oxidation of Metals and Alloys," Butterworths, London, Chapt 1 (1962).
10. G.A. Parks, Chem. Rev. 65, 177 (1965).
11. J.C. Bolger and A.S. Michaels, Interface Conversion (Editor: P. Weiss), Elsevier, Amsterdam, pp. 3-51 (1968).
12. G.H. Cartledge, J. Amer. Chem. Soc. 52, 3076 (1930).
13. T. Moeller, "Inorganic Chemistry," Wiley, New York, p. 210 (1952).
14. F. Mansfeld, Science Center, personal communication (1981).
15. T.P. Hoar, J. Electrochem. Soc. 117(1), p. 17c (1970).
16. P. Hedwig, "Dielectric Spectroscopy of Polymers," Halstead Press, New York, Chap. 1 (1977).
17. K.W. Bewig and W.A. Zisman, J. of Phys. Chem. 68, p. 1804 (1964).
18. L. Pauling, Amer. Mineralogist, 65, p. 321 (1981).
19. R.F. Steward, M.W. Whitehead and G. Donnay, Ibid, 65, p. 324 (1980).

20. J.A. Tossell, Ibid, 65, p. 163 (1980).
21. I.D. Brown and R.D. Shannon, Acta Cryst. A29, p. 266 (1973).
22. P.E.D. Morgan, "Bonding in Nitrogen Ceramics," Nitrogen Ceramics (Editor: F.L. Riley), Nordhoff, Leiden, pp. 23-40 (1977).
23. R.J. Gottschall and A.W. Czanderna, "Basic Research Needs and Opportunities on Interfaces in Solar Materials: An Executive Summary," J. of Metals p. 27 (October 1981).
24. D.H. Kaelble, "Relations Between Polymer Chemistry and Physical Properties," ACS Organic Coatings and Plastics Preprint, 43(1), April (1982), in press.
25. D.H. Kaelble, "Relations Between Polymer Chemistry and Mechanical Properties," Ibid 43(1), (April, 1982) in press.

FIGURE CAPTIONS

- Fig. 1 Covalent bond energy D_{AA} and electronegativity X for the elements.
- Fig. 2 The maximum valence to atomic radius ratio MV/R vs electronegativity X .
- Fig. 3 Acidity index $pH \approx 16-3S$ vs atomic number.
- Fig. 4 pH vs (MV/R) for acids and bases.
- Fig. 5 Acid dissociation index pK_A vs (V/R) for miscellaneous acids and bases at varied valence.
- Fig. 6 Acid dissociation index pK_A vs apparent cation valence V and V/R .
- Fig. 7 Calculated maximum Coulomb energy U_M between adsorbate and substrate oxides.
- Fig. 8 Calculated nominal Coulomb energy U_N between adsorbate and substrate oxides.

Table 1
Properties of the Elements
(Sheet 1 of 2)

Code No.	Z	SY	W G/Mole	D 10 ⁵ J/Mole	X	R 10 ⁻¹⁰ m	V	MV	S
1	1	H	1.008	4.35	2.20	0.32	1	1	3.13
2	3	LI	6.941	1.11	0.98	1.23	1	1	0.81
3	3	BE	9.012	(2.28)	1.57	0.90	2	2	2.22
4	5	B	10.81	(2.53)	2.04	0.82	3	3	3.66
5	6	C	12.01	3.48	2.55	0.77	4	4	5.19
6	7	N	14.01	1.61	3.04	0.75	3	5	6.67
7	8	O	16.00	1.39	3.44	0.73	2	2	2.74
8	9	F	19.00	1.53	3.98	0.72	1	1	1.39
9	11	NA	22.99	0.753	0.93	1.54	1	1	0.65
10	12	MG	24.31	(0.971)	1.31	1.36	2	2	1.47
11	13	AL	26.98	(2.06)	1.61	1.18	3	3	2.54
12	14	SI	28.09	1.77	1.90	1.11	4	4	3.60
13	15	P	30.97	2.15	2.19	1.06	5	5	4.72
14	16	S	32.06	2.13	2.58	1.02	6	6	5.88
15	17	CL	35.45	2.43	3.16	0.99	1	7	7.07
16	19	K	39.09	0.552	0.82	2.03	1	1	0.49
17	20	CA	40.08	(1.15)	1.00	1.74	2	2	1.15
18	21	SC	44.96	(2.58)	1.36	1.44	3	3	2.08
19	22	TI	47.90	(2.64)	1.54	1.32	4	4	3.03
20	23	V	50.94	(3.36)	1.63	1.22	5	5	4.10
21	24	CR	52.00	(2.38)	1.66	1.18	3	6	5.08
22	25	MN	54.94	(1.43)	1.55	1.17	2	7	5.98
23	26	FE	55.85	(2.03)	1.83	1.17	3	3	2.56
24	27	CO	58.93	(2.20)	1.88	1.16	2	3	2.59
25	28	NI	58.70	(2.12)	1.91	1.15	2	3	2.61
26	29	CU	63.55	(1.72)	1.90	1.17	2	2	1.71
27	30	ZN	65.38	(0.653)	1.65	1.25	2	2	1.60
28	31	GA	69.72	(1.36)	1.81	1.26	3	3	2.38
29	32	GE	72.59	1.57	2.01	1.22	4	4	3.28
30	33	AS	74.92	1.34	2.18	1.20	3	5	4.17
31	34	SE	78.96	1.84	2.55	1.16	4	6	5.17
32	35	BR	79.90	1.93	2.96	1.14	1	7	6.14
33	37	RB	85.47	0.519	0.82	2.16	1	1	0.46
34	38	SR	87.62	(1.05)	0.95	1.91	2	2	1.05
35	39	Y	88.91	(2.74)	1.22	1.62	3	3	1.85
36	40	ZR	91.22	(3.45)	1.33	1.45	4	4	2.76
37	41	NB	92.91	(4.85)	1.60	1.34	5	5	3.73

Table 1
Properties of the Elements
(Sheet 2 of 2)

Code No.	Z	SY	W G/Mole	D 10^5 J/Mole	X	R 10^{-10} m	V	MV	S
38	42	MO	95.94	(4.30)	2.16	1.30	6	6	4.62
39	43	TC	98.0	(3.35)	1.90	1.27	7	7	5.51
40	44	RU	101.07	(3.35)	2.20	1.25	3	8	6.40
41	45	RH	102.91	(3.24)	2.28	1.25	3	4	3.20
42	46	PD	106.4	(1.93)	2.20	1.28	2	4	3.13
43	47	AG	107.87	(1.44)	1.93	1.34	1	1	0.75
44	48	CD	112.41	(0.552)	1.69	1.48	2	2	1.35
45	49	IN	114.82	(1.18)	1.78	1.44	3	3	2.08
46	50	SN	118.69	1.43	1.96	1.41	4	4	2.84
47	51	SB	121.75	1.26	2.05	1.40	3	5	3.57
48	52	TE	127.60	1.38	2.10	1.36	4	6	4.41
49	53	I	126.90	1.51	2.66	1.33	1	7	5.26
50	55	CS	132.91	0.448	0.79	2.35	1	1	0.43
51	56	BA	137.33	(1.12)	0.89	1.98	2	2	1.01
52	57	LA	138.91	(2.48)	1.10	1.69	3	3	1.78
53	72	HF	178.49	(4.72)	1.30	1.44	4	4	2.78
54	73	TA	180.95	(5.56)	1.50	1.34	5	5	3.73
55	74	W	183.85	(5.61)	2.36	1.30	6	6	4.62
56	75	RE	186.21	(3.97)	1.90	1.28	7	7	5.47
57	76	OS	190.2	(3.64)	2.20	1.26	4	8	6.35
58	77	IR	192.22	(3.48)	2.20	1.27	4	6	4.72
59	78	PT	195.09	(2.79)	2.28	1.30	4	4	3.08
60	79	AU	196.97	(1.86)	2.54	1.34	3	3	2.24
61	80	HG	200.59	(0.301)	2.00	1.49	2	2	1.34
62	81	TL	204.37	(0.866)	2.04	1.48	1	3	2.03
63	82	PB	207.2	(0.992)	2.33	1.47	2	4	2.72
64	83	BI	209.0	(1.03)	2.02	1.46	3	5	3.42
65	90	TH	232.04	(3.42)	1.30	1.65	4	4	2.42
66	92	U	238.03	(3.56)	1.38	1.42	6	6	4.22
67	94	PU	244.0	(2.29)	1.28	1.21	4	6	4.96
68	7	(N2)/2	14.01	4.73	3.04	0.55	3	5	6.67
69	8	(O2)/2	16.00	2.01	3.44	0.62	2	2	2.74

Table 2
Comparison of Single Bond Energies

Element	Group	Single Bond Energy (kcal/mol)		
		Ref. 2	Eq. (2) (C.N.=12)	Ratio
Lithium	IA	25.6	6.3	4.06
Sodium	IA	18	4.3	4.19
Potassium	IA	13.2	3.3	4.00
Rubidium	IA	12.4	3.4	3.65
Cesium	IA	10.7	3.0	<u>3.57</u>
				3.89 ± 0.27
Boron	IIIB	25.0	15.1	1.66
Germanium	IVB	37.6	13.2	2.85
Arsenic	VB	32.1	9.5	3.38
Tin	IVB	34.2	11.4	3.00
Antimony	VB	30.2	10.6	<u>2.85</u>
				2.75 ± 0.65

Table 3
Lattice Types and Packing Factors

Lattice Type	Coordination Number	Packing Factor (C)
Face centered cubic	12	1.414
Body centered cubic	8	1.299
Simple cubic	6	1.000
Tetrahedral	4	0.650

Table 4

Calculation of Heat of Formation for BeO, TiO₂, and Al₂O₃

Z, SY, W, D/1E5, X, R/1E-10, V, PH =

4 BE 9.012 2.28 1.57 0.9 2 7

8 0 16 1.39 3.44 0.73 2 2

To continue press ENTER

?

Chemical Analysis:

Bonding Elements	Bond Energy (J/mole)	% Ionic Energy	Bond Length (M*1E-10)	Moles
A B				
BE BE	228000	0	1.8	-1
(02)/2(02)/2	201000	0	1.24	-1
BE O	520951	64.776	1.4617	2
Total	612902			0

To continue press ENTER

Z, SY, W, D/1E5, X, R/1E-10, V, PH =

22 TI 47.0 2.64 1.54 1.32 4 7

8 0 16 1.39 3.44 0.73 2 2

To continue press ENTER

?

Chemical Analysis:

Bonding Elements	Bond Energy (J/mole)	% Ionic Energy	Bond Length (M*1E-10)	Moles
A B				
TI TI	264000	0	2.64	-2
(02)/2(02)/2	201000	0	1.24	-2
TI O	549865	63.3547	1.879	4
Total	1.26946E+06			0

To continue press ENTER

Z, SY, W, D/1E5, X, R/1E-10, V, PH =

13 AL 26.98 2.06 1.61 1.18 3 7

8 0 16 1.39 3.44 0.73 2 2

To continue press ENTER

?

Chemical Analysis:

Bonding Elements	Bond Energy (J/mole)	% Ionic Energy	Bond Length (M*1E-10)	Moles
A B				
AL AL	206000	0	2.36	-3
(02)/2(02)/2	201000	0	1.24	-3
AL O	495669	65.1986	1.7453	6
Total	1.75301E+06			0

To continue press ENTER

? -

Table 5
Comparison of Calculated and Experimental Heats of
Formation for Oxides

Compound	$-\Delta H_f(\text{calc.})$ (10^5 J/mole)	$-\Delta H_f$ (Ref. 7) (10^5 J/mole)	Difference (10^5 J/mole)
Al_2O_3	17.5	16.3	1.20
Fe_2O_3	13.1	11.2	1.90
TiO_2	12.7	9.11	3.59
MgO	8.13	5.20	2.93
SiO_2	7.91	8.56	-0.65
BeO	6.13	6.10	0.03
MoO_2	5.08	5.43	-0.35
WO_2	3.26	5.70	-2.44
Au_2O_3	2.83	-0.80	3.63
SeO_2	1.82	2.29	<u>-0.47</u>
Sum:			0.94
Std. Dev:			± 2.04

Table 6
Comparison of Calculated and Experimental Heats of
Formation for Chlorides

Compound	$-\Delta H_f(\text{calc.})$	$-\Delta H_f$ (Ref. 7) (10^5 J/mole)	Difference
AlCl_3	6.95	6.95	0.0
FeCl_3	5.12	4.05	1.07
TiCl_4	10.1	7.50	2.60
MgCl	3.30	6.41	-3.11
SiCl_4	6.12	6.10	0.02
BeCl_2	4.87	5.11	-0.24
MoCl_4	3.86	3.30	0.56
AuCl_3	1.11	1.18	<u>-0.07</u>
		Sum:	0.10
		Std. Dev:	± 1.60

Table 7
Calculation of the Oxidation Dilution Factor ϕ for Metals

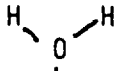
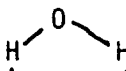
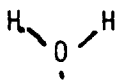
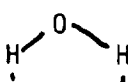
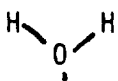
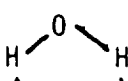
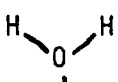
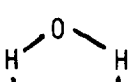
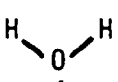
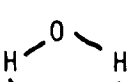
Oxide	Calculated (for Z = 12)			Exper. (7,8)	
	$V(\text{Me})$ (CC)	$V(\text{MeO}_x)$ (CC)	ϕ	$V(\text{MeO}_x)$ (CC)	ϕ
K ₂ O	57.02	20.55	0.36	40.6	0.45
BaO	26.45	13.00	0.49	26.8	0.67
MgO	8.57	6.34	0.74	11.3	0.81
Al ₂ O ₃	11.19	11.32	1.01	25.7	1.28
TiO ₂	7.84	8.48	1.08	18.7	1.78
Fe ₂ O ₃	10.92	11.52	1.05	30.5	2.14
Ta ₂ O ₅	16.40	20.31	1.24	53.9	2.50
Nb ₂ O ₅	16.40	20.60	1.26	59.5	2.68
MoO ₃	7.49	11.96	1.60	30.7	3.30
WO ₃	7.49	12.30	1.64	32.4	3.35

$$\phi = \frac{\text{molecular volume of metal compound } \text{MeO}_x}{\text{atomic volume of equal moles of metal } \text{M}_e}$$

Table 8
Correlation Between Metal Oxidation State
and IEPS

Oxide	IEPS Range (pH Units)	Acid-Base Character
M ₂ O	pH > 11.5	strong base
MO	8.5 < pH < 12.5	intermediate base
M ₂ O ₃	6.5 < pH < 10.4	weak base
MO ₂	0 < pH < 7.5	intermediate acid
M ₂ O ₅ , MO ₃	pH < 0.5	strong acid

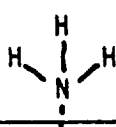
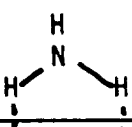
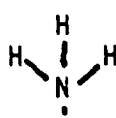
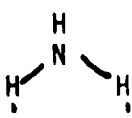
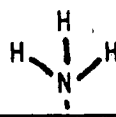
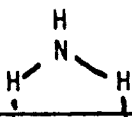
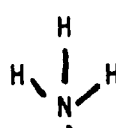
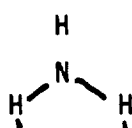
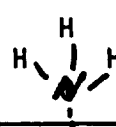
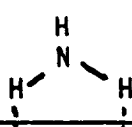
Table 9
Coulomb Bond Energies Between Water and Various Oxides

																					
(Ag ₂ O)	Ag	O	Ag	O	Ag	O	Ag	O	Ag	O	Ag	O	Ag	O	Ag	O	Ag	O	Ag	O	
																					
(CuO)	O	Cu	O	Cu	O	Cu	O	Cu	O	Cu	O	Cu	O	Cu	O	Cu	O	Cu	O	Cu	
																					
(Fe ₂ O ₃)	O	Fe	O	Fe	O	Fe	O	Fe	O	Fe	O	Fe	O	Fe	O	Fe	O	Fe	O	Fe	
																					
(SiO ₂)	O	Si	O	Si	O	Si	O	Si	O	Si	O	Si	O	Si	O	Si	O	Si	O	Si	
																					
(CrO ₃)	O	Cr	O	Cr	O	Cr	O	Cr	O	Cr	O	Cr	O	Cr	O	Cr	O	Cr	O	Cr	

Adsorbate: H ₂ O		Monobasic		Diacid	
Substrate	Oxide	U _M (kJ/mole)	U _N	U _M	U _N
Ag ₂ O		11.8	2.4	46.5	9.6
CuO		25.7	5.2	46.5	9.5
Fe ₂ O ₃		38.5	7.1	46.5	9.3
SiO ₂		53.0	10.6	46.5	9.3
CrO ₃		76.6	16.2	46.5	9.2

1770-

Table 10
Coulomb Bond Energies Between Ammonia and Various Oxides

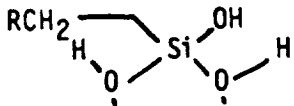
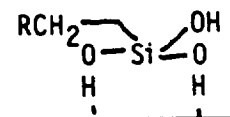
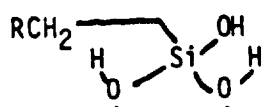
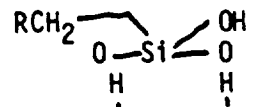
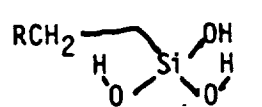
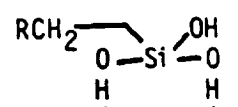
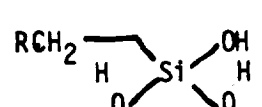
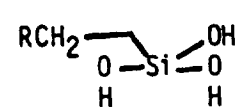
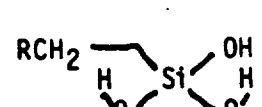
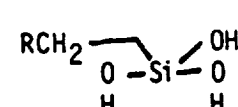
															
(Ag ₂ O)	0	Ag	0	Ag	0	Ag	0	Ag	0	Ag	0	Ag	0		
															
(CuO)	0	Cu	0	Cu	0	Cu	0	Cu	0	Cu	0	Cu	0		
															
(Fe ₂ O ₃)	0	Fe	0	Fe	0	Fe	0	Fe	0	Fe	0	Fe	0		
															
(SiO ₂)	0	Si	0	Si	0	Si	0	Si	0	Si	0	Si	0		
															
(CrO ₃)	0	Cr	0	Cr	0	Cr	0	Cr	0	Cr	0	Cr	0		

Adsorbate:NH ₃ Substrate Oxide	Monobasic		Diacid	
	U _M (kJ/mole)	U _N	U _M	U _N
Ag ₂ O	17.5	2.0	46.5	9.6
CuO	38.1	4.3	46.5	9.5
Fe ₂ O ₃	57.2	6.4	46.5	9.3
SiO ₂	78.7	8.8	46.5	9.3
CrO ₃	113.8	13.4	46.5	9.2

000-1

Adsorbate: CrO_3	Dibasic		Monoacid	
Substrate Oxide	$U_M(\text{kJ/mole})$	U_N	U_M	U_N
Ag_2O	24.9	8.8	76.6	27.1
CuO	40.9	14.2	76.6	26.7
Fe_2O_3	81.7	28.0	76.6	26.2
SiO_2	112.8	38.6	76.6	26.2
CrO_3	162.7	58.5	76.6	27.6

Table 12
Coulomb Bond Energies Between R-CH₂ Si(OH)₃ and Various Oxides

	
(Ag ₂ O)	0 Ag 0 Ag 0 Ag 0 Ag 0 Ag 0 Ag 0 Ag 0 Ag 0
	
(CuO)	0 Cu 0 Cu 0 Cu 0 Cu 0 Cu 0 Cu 0 Cu 0 Cu 0 Cu 0
	
(Fe ₂ O ₃)	0 Fe 0 Fe 0 Fe 0 Fe 0 Fe 0 Fe 0 Fe 0 Fe 0 Fe 0
	
(SiO ₂)	0 Si 0 Si 0 Si 0 Si 0 Si 0 Si 0 Si 0 Si 0 Si 0
	
(CrO ₃)	0 Cr 0 Cr 0 Cr 0 Cr 0 Cr 0 Cr 0 Cr 0 Cr 0 Cr 0

Adsorbate:R ₃ Si(OH) ₂	Dibasic	Diacid		
Substrate Oxide	U _M (kJ/mole)	U _N	U _M	U _N
Ag ₂ O	23.6	6.63	45.6	16.4
CuO	51.4	14.6	45.6	16.1
Fe ₂ O ₃	77.0	21.8	45.6	15.9
SiO ₂	106.0	30.0	45.6	15.9
CrO ₃	153.2	45.6	45.6	16.7

Table 13
Bond Properties for Adsorbates and Substrate Oxides

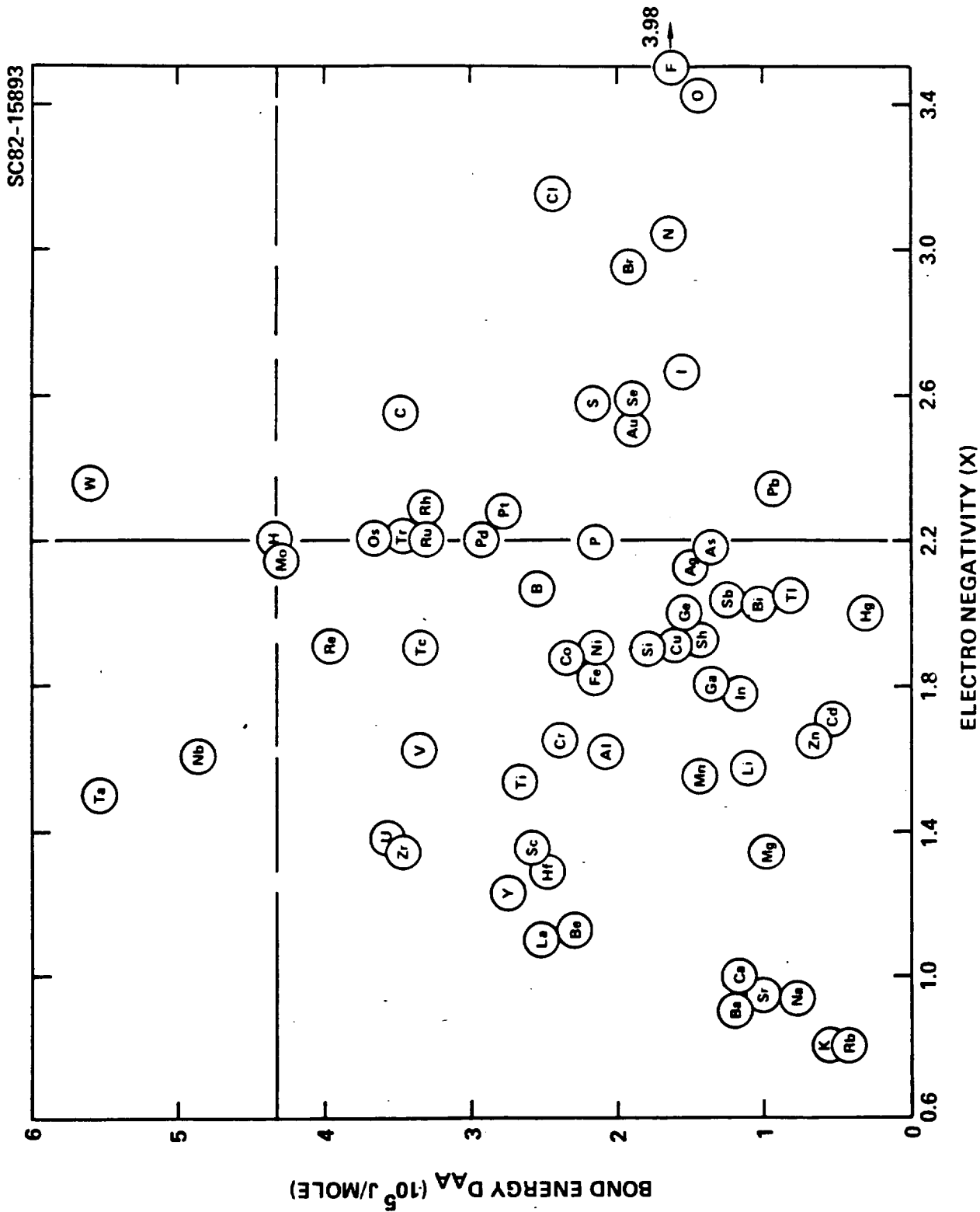
Bond + - -	D_{AB} (kJ/mole)	%I	L_{AB}	μ (debye)	R_A	R_B
H - O	435	34.1	0.94	1.54	0.32	0.73
H - N	366	18.6	0.99	0.88	0.32	0.75
Cr = O	1051	58.2	1.64	4.58	1.18	0.62
Ag - O	362	60.9	1.93	5.64	1.34	0.73
Cu - O	384	59.5	1.76	5.03	1.17	0.73
Fe - O	421	59.4	1.76	4.56	1.17	0.73
Si - O	387	59.1	1.70	4.82	1.11	0.73
Cr - O	494	61.9	1.75	5.20	1.18	0.73
Si - C	303	13.4	1.82	1.17	1.11	0.77

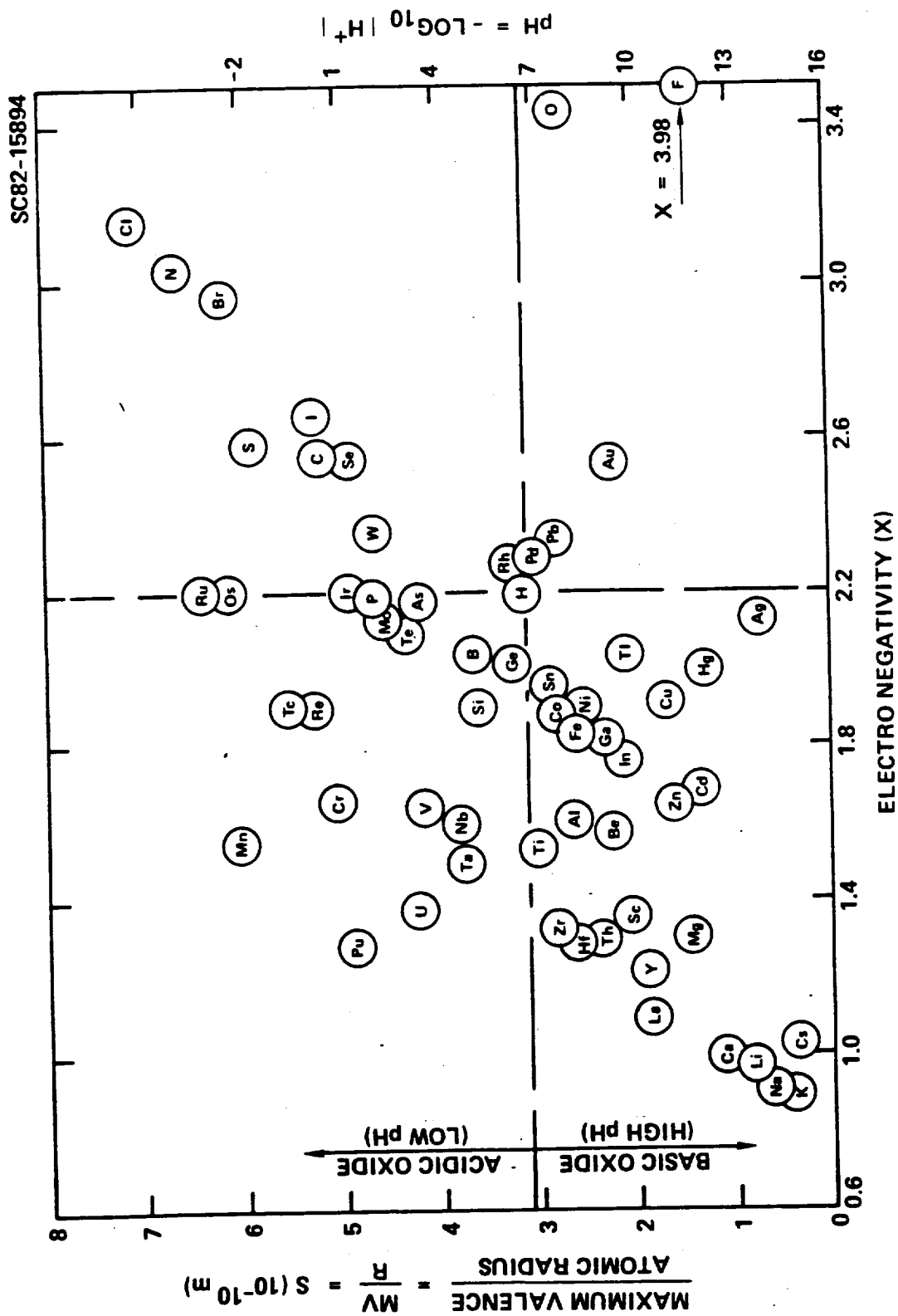
Table 14
Comparison of Revised (Ref. 1 = X) and Pauling (Ref. 2 = X_p)
Values of Elemental Electronegativity

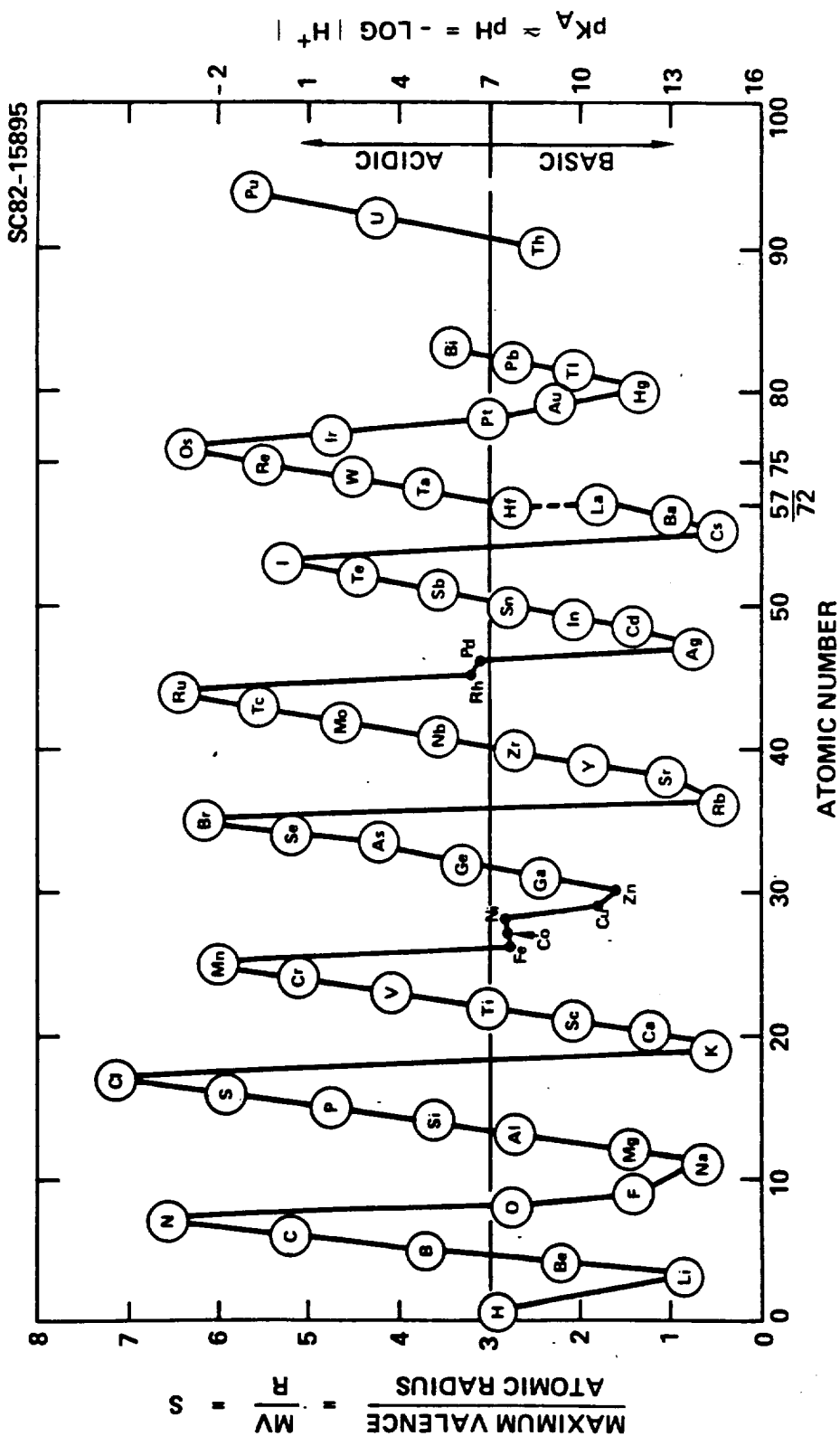
AT. No.	SY	X	X_p	$X-X_p$	AT. No.	SY	X	X_p	$X-X_p$
1	H	2.20	2.1	0.10	37	RB	0.82	0.8	0.02
3	LI	0.98	1.0	-0.02	38	SR	0.95	1.0	-0.05
4	BE	1.57	1.5	0.07	38	Y	1.22	1.2	0.02
5	B	2.04	2.0	0.04	40	ZR	1.33	1.4	-0.07
6	C	2.55	2.5	0.05	41	NB	1.60	1.6	0.0
7	N	3.04	3.0	0.04	42	MO	2.16	1.8	0.36
8	O	3.44	3.5	-0.06	43	TC	1.90	1.9	0.0
9	F	3.98	4.0	-0.02	44	RU	2.20	2.2	0.0
					45	RH	2.28	2.2	0.08
11	NA	0.93	0.9	0.03	46	PD	2.20	2.2	0.0
12	MG	1.31	1.2	0.11	47	AG	1.93	1.9	0.03
13	AL	1.61	1.5	0.11	48	CD	1.69	1.7	-0.01
14	SI	1.90	1.8	0.10	49	IN	1.78	1.7	0.08
15	P	2.19	2.1	0.19	50	SN	1.96	1.8	0.16
16	S	2.58	2.5	0.08	51	SB	2.05	1.9	0.15
17	CL	3.16	3.0	0.16	52	TE	2.10	2.1	0.0
					53	I	2.66	2.5	0.16
19	K	0.82	0.8	0.02	55	CS	0.79	0.7	0.09
20	CA	1.00	1.0	0.0	56	BA	0.89	0.9	-0.01
21	SC	1.36	1.3	0.06	57	LA	1.10	1.1	0.0
22	TI	1.54	1.5	0.04	72	HF	1.30	1.3	0.0
23	V	1.63	1.6	0.03	73	TA	1.50	1.5	0.0
24	CR	1.66	1.6	0.06	74	W	2.36	1.7	0.66
25	MN	1.55	1.5	0.05	75	RE	1.90	1.9	0.0
26	FE	1.83	1.8	0.03	76	OS	2.20	2.2	0.0
27	CO	1.88	1.8	0.08	77	IR	2.20	2.2	0.0
28	NI	1.91	1.8	0.11	78	PT	2.28	2.2	0.08
29	CU	1.90	1.9	0.0	79	AU	2.54	2.4	0.14
30	ZN	1.65	1.6	0.05	80	HG	2.00	1.9	0.10
31	GA	1.81	1.6	0.21	81	TL	2.04	1.8	0.24
32	GE	2.01	1.8	0.21	82	PB	2.33	1.8	0.53
33	AS	2.18	2.0	0.18	83	BI	2.02	1.9	0.12
34	SE	2.55	2.4	0.15					
35	BR	2.96	2.8	0.16	90	TH	1.30	1.3	0.0
					92	U	1.38	1.7	-0.32
					94	PU	1.28	-	-

56

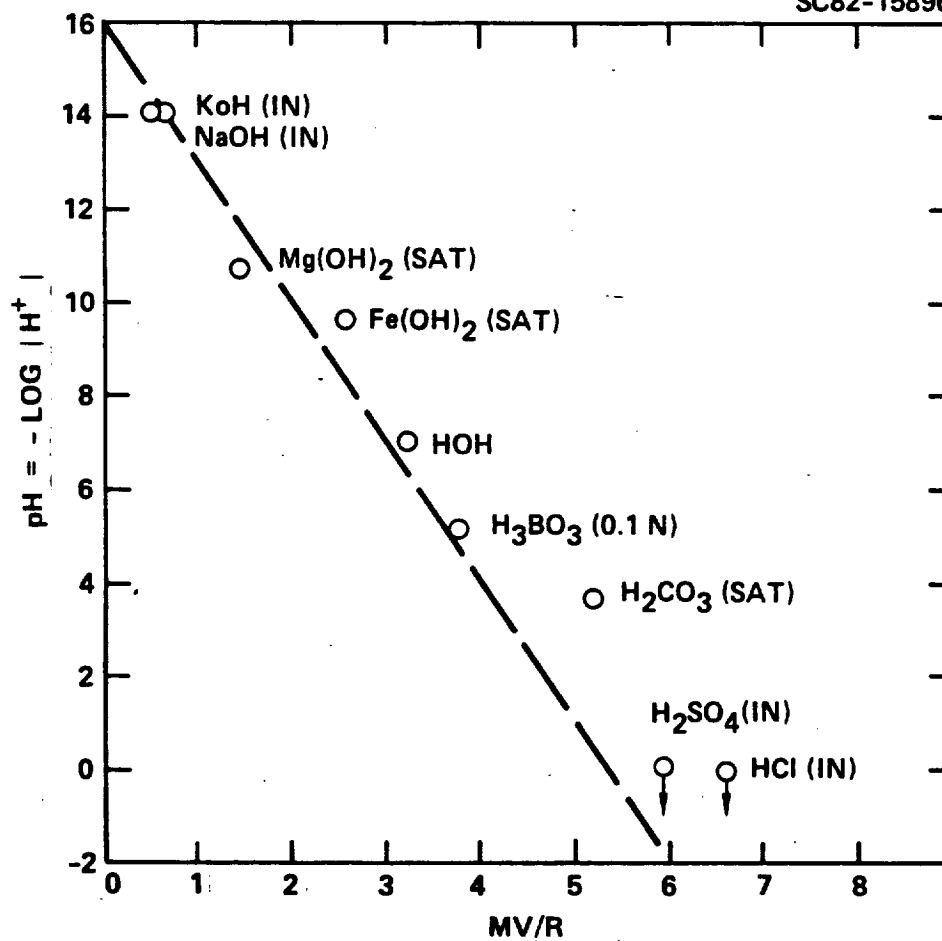
35.84



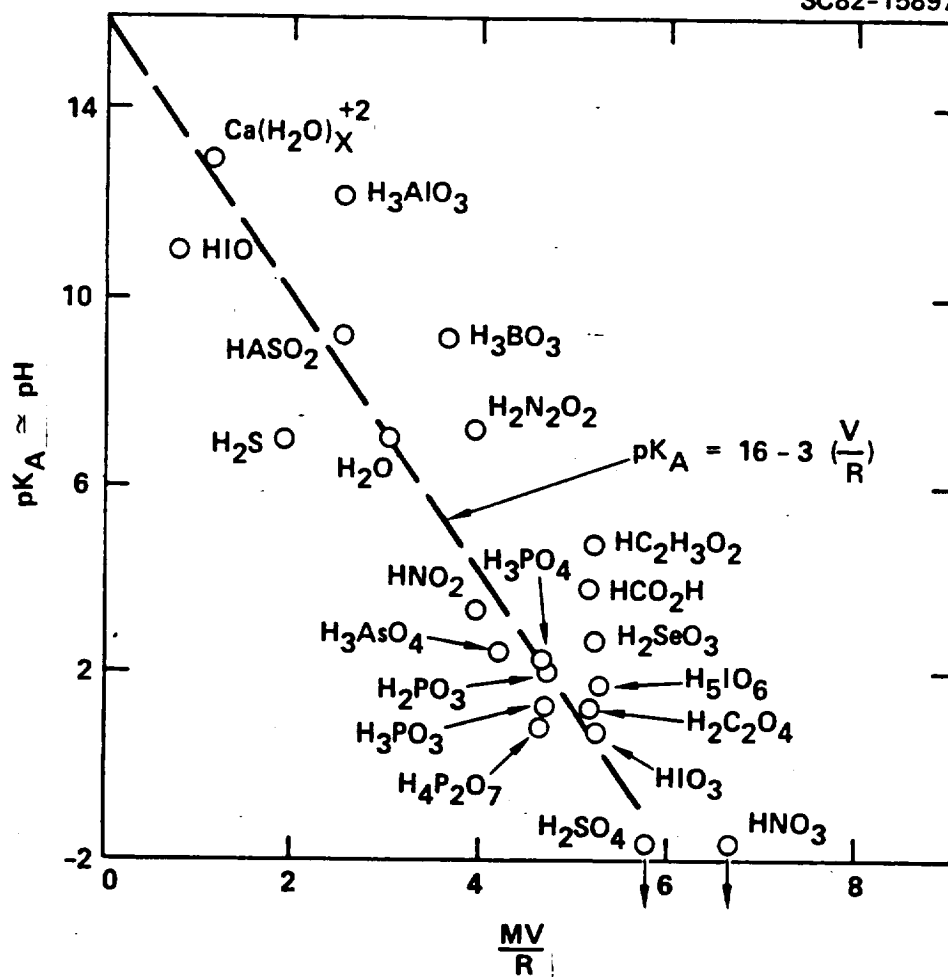




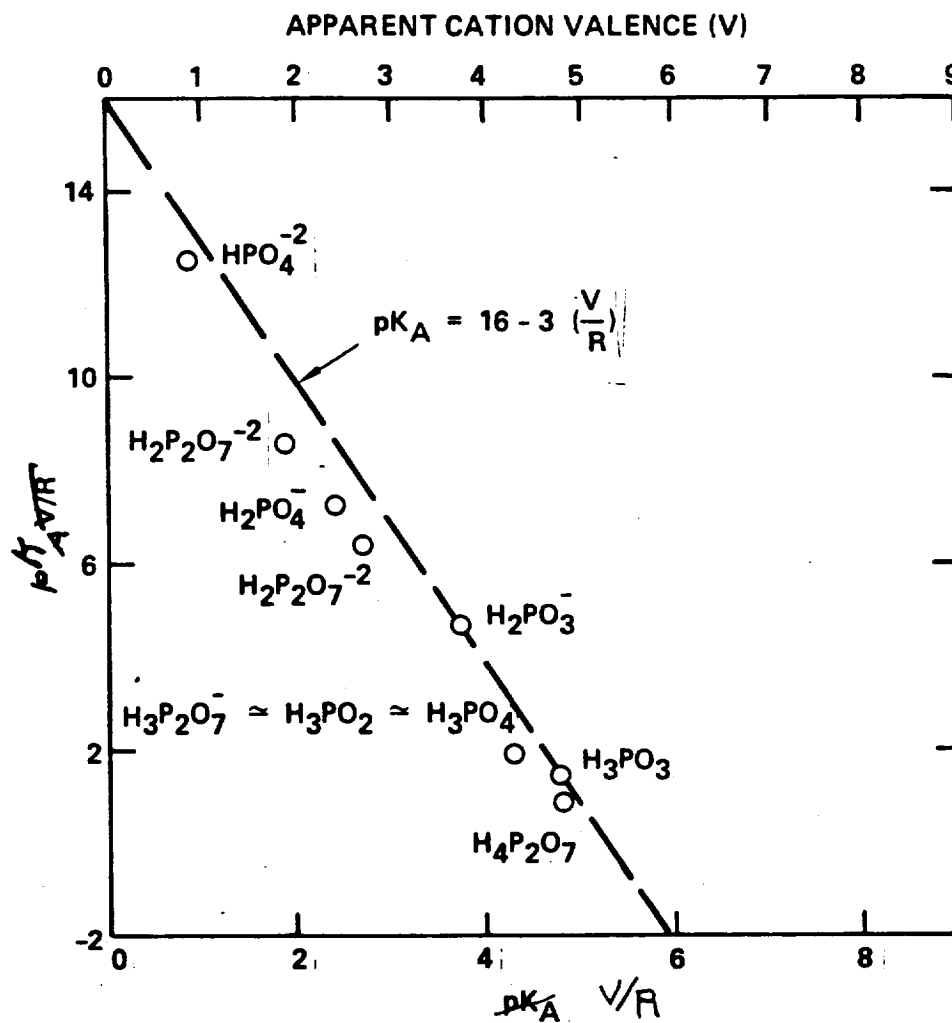
SC82-15896



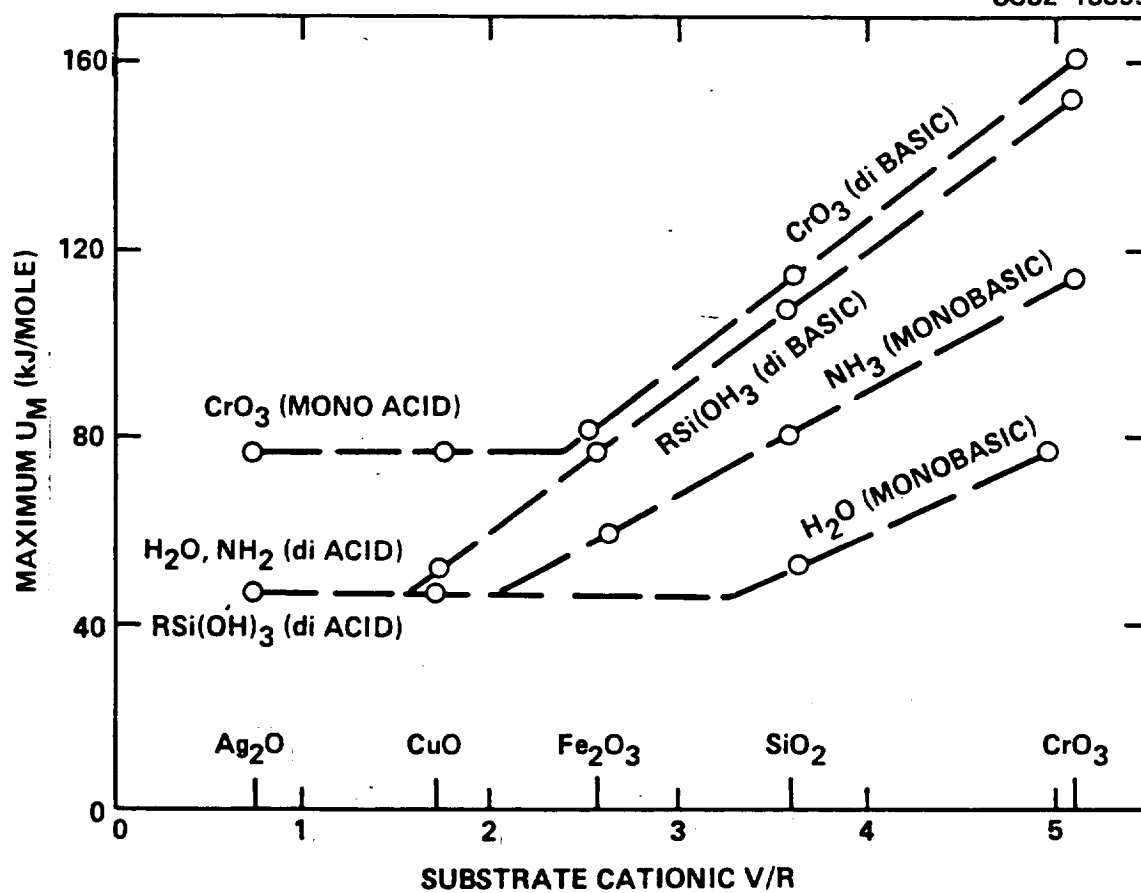
SC82-15897

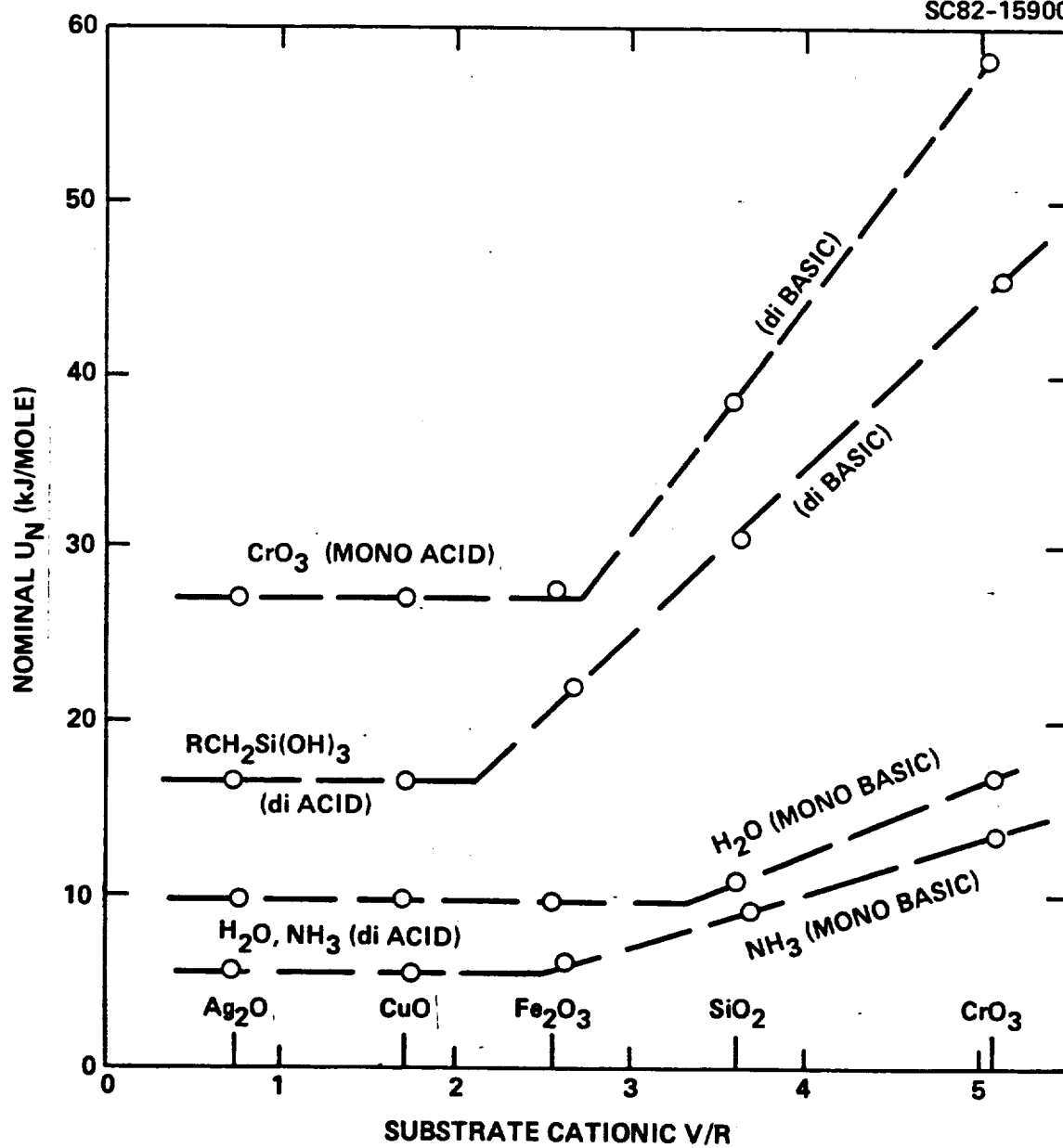


SC82-15898



SC82-15899





APPENDIX 2

Relations Between Polymer Chemistry and Physical Properties

D.H. Kaelble Rockwell International Science Center
1049 Camino Dos Rios
Thousand Oaks, CA 91360

ACS Membership number MUST be indicated for at least one author _____
(Please use number as it appears on C&EN mailing label)

RELATIONS BETWEEN POLYMER CHEMISTRY AND PHYSICAL PROPERTIES. D.H. Kaelble.
Rockwell International Science Center, 1049 Camino Dos Rios, Thousand Oaks, CA 91360

Methods are presented for computer assisted estimations of polymer specific volume V_p , solubility parameter δ , glass temperature T_g , and molecular weight between entanglements M_e .—These properties are computed from 33 functional groups, ranging from methylene to sulfone, which can be combined to describe the main chain and side chain structures of model linear polymers. The additional effects of molecular weight and cross linking upon glass transition temperature are computationally defined. The functional group properties are stored in computer memory and recalled by an interactive computer program which permits construction of the polymer repeat unit chemistry for both main chain and side chain structures. The computation then describes the above four physical properties for the infinite linear polymer in its amorphous glass state. This monomer-polymer prediction program is self-instructive and useful in qualitative exploration of chemical structure effects on polymer processability and performance.

RELATIONS BETWEEN POLYMER CHEMISTRY AND PHYSICAL PROPERTIES

D.H. Kaelble

Rockwell International Science Center
Thousand Oaks, CA 91360

INTRODUCTION. Extensive tabulations of polymer properties very often are limited to the major classes of commercially important polymers. Very often the chemist or materials specialist wishes to obtain an qualitative estimate of several important polymer properties such as specific volume V_p , solubility parameter δ , and glass temperature T_g simply by writing the chemical structure of the polymer repeat unit. The characteristic molecule weight between interchain entanglements M_e , serves as an important index of true high polymer response and is defined by a new relation which correlates M_e with the apparent cross section area of the polymer chain.

FUNCTIONAL GROUP PROPERTIES. The functional group properties of the 33 functional groups utilized in this computation are listed in Table 1. The first column of Table 1 lists the group number which is employed as a retrieval number in the computer program. The second column lists the structure group in terms of a simplified upper case code with parenthesis to indicate side group structures and parenthesised numbers to indicate multiple side units. The reference polymer for each structure group shown in the right column of Table 1 further identifies the functional group chemistry. The central five columns of Table 1 tabulate the group properties utilized in the computation. From left to right these group properties are defined as follows:

U = the cohesive energy per group

H = group contribution to internal degrees of freedom related to rotational motion.

N = number of main chain atoms per group

V = group contribution to molar volume

M = molar weight per group.

The substantial proportion of the group values of U and H are based on the published volumes of Hayes¹ and the rest derived by inspection of known polymer properties. The values of N and M are directly deduced from chemical structure and magnitude of V based upon LeBas values of atomic molar volume as reviewed by Kaelble.²

POLYMER PROPERTY RELATIONS. The polymer specific volume for the amorphous glass state is calculated by a simple empirical relation demonstrated by Kaelble which is given as follows:

$$V_p = 0.69 \left[\frac{\sum V}{\sum M} \right] \quad (1)$$

where $\sum V$ and $\sum M$ describe the summations of V and m that describe the polymer repeat unit. The constant 0.69 minimizes the deviations between experimental and calculated values of V_p for 13 polymers and generally gives agreement within 5 percent.²

The polymer solubility parameter squared, δ^2 , is termed the cohesive energy density and calculated by the following relation:

$$\delta^2 = 1.44 \left[\frac{\sum U}{\sum V} \right] \quad (2)$$

Table 1
Functional Group Properties for Polymers

Unit No.	(R = 8.314 J/K*mole) Structure Group	U (J/mole)	H	N	V (m ³ /mole)	M (kg/mole)	Polymer Unit
1	-CH ₂ -	4.14E3	8	1	2.22E-5	1.4E-2	ethylene
2	-CH(CH ₃)-	1.28E4	11	1	4.44E-5	2.8E-2	propylene
3	-C((CH ₃) ₂)-	1.19E4	14	1	6.66E-5	4.2E-2	isobutylene
4	-CH(C ₆ H ₅)-	3.01E4	15	1	1.11E-4	9.0E-2	styrene
5	-P-C ₆ H ₄ -	2.38E4	5	4	8.86E-5	7.6E-2	terephthlate
6	-M-C ₆ H ₄ -	2.58E4	10	3	8.86E-5	7.6E-2	isophthalate
7	-C(CH ₃)CH-	1.15E4	11	2	5.92E-5	4.0E-2	isoprene
8	-CHCH-	7.49E3	8	2	3.70E-5	2.6E-2	1,4-butadiene
9	-CH(CHCH ₂)-	1.29E4	11	1	5.90E-5	4.0E-2	1,2-butadiene
10	-CH(C ₆ H ₁₁)-	2.56E4	21	1	1.48E-4	9.6E-2	vinyl cyclohexane
11	-CH(C(O)OCH ₃)-	2.81E4	23	1	7.57E-5	7.2E-2	methacrylate
12	-C(CH ₃)(C(O)OCH ₃)-	4.60E4	26	1	9.79E-5	8.6E-2	methylmethacrylate
13	-CH(CH ₃)O-	1.39E4	17	2	5.54E-5	4.4E-2	propylene oxide
14	-C(O)O-	1.41E4	12	2	3.32E-5	4.4E-2	ethylene adipate
15	-CH(OC(O)CH ₃)-	3.17E4	23	1	7.57E-5	7.2E-2	vinyl acetate
16	-C(O)-	7.32E3	6	1	2.22E-5	2.8E-2	ketone
17	-CH(C(O)OH)-	3.51E4	20	1	5.64E-5	5.8E-2	acrylic acid
18	-CH(OH)-	2.66E4	14	1	4.90E-5	3.0E-2	vinyl alcohol
19	-CH(OC(O)O)-	2.86E4	20	1	5.54E-5	5.8E-2	vinyl formate
20	-O-	6.82E3	6	1	1.06E-5	1.6E-2	ether
21	-NHC(O)-	4.44E4	13	2	3.79E-5	4.3E-2	amide
22	-NHC(O)O-	2.63E4	19	3	4.89E-5	5.9E-2	urethane
23	-CH(CN)-	2.41E4	8	1	4.89E-5	3.9E-2	acrylonitrile
24	-CH(C ₂ H ₅)-	1.75E4	8	1	4.07E-5	4.85E-2	vinyl chloride
25	-C(C ₂ H ₅)CH-	1.26E4	8	2	5.55E-5	6.05E-2	neoprene
26	-C((C ₂ H ₅) ₂)-	1.13E4	8	1	5.92E-5	8.30E-2	vinylidene chloride
27	-CF ₂ -	4.81E3	8	1	3.48E-5	5.0E-2	tetrafluoroethylene
28	-CH ₂ CF ₂ -	1.48E4	16	2	5.70E-5	6.4E-2	vinylidene fluoride
29	-CF(CF ₃)-	1.84E4	13	1	6.96E-5	1.0E-1	perfluoropropylene
30	-Si((CH ₃) ₂)O-	1.72E4	30	2	8.62E-5	7.4E-2	dimethylsiloxane
31	-N((C(O)) ₂)C ₆ H ₂ ((C(O)) ₂)N-	1.10E5	62	7	2.01E-4	2.14E-1	imide
32	-S-	8.26E3	8	1	2.56E-5	3.2E-2	sulfide
33	-S((O) ₂)-	4.54E4	23	1	4.04E-5	6.40E-2	sulfone

where ΣU is the summation of the group cohesive energies and ΣV the summation of the group molar volumes. The constant 1.44 reduces the LeBas values of molar volume to represent the polymer structure in the solid state. This computation calculates the value of cohesive energy density and expresses this result as the square of the familiar solubility parameter δ .

The Kelvin scale value of the glass transition temperature is calculated by a slight modification of the equation proposed by Hayes [1] with the following form:

$$T_g = \frac{2}{R} \left[\frac{\Sigma U}{\Sigma H} \right] + C(t) \quad (3)$$

In Eq. (3) R is the gas constant and ΣU and ΣH are the respective summations of cohesive energies and degrees of freedom for the functional groups of the polymer repeat unit. The constant $C(t) = 25K$ in Eq. (3) is a temperature compensation which reflects the time scale of T_g measurements. The rule of thumb is that T_g is increased by roughly three degrees centigrade by each factor of ten reduction in measurement time.² Slow thermal expansion measurement of T_g is associated with $C(t) = 25K$ and is used in the computer computations. More rapid scanning calorimeter measurements might require $C(t) = 20K$ as a normalizing correction.

The relation for calculating the molecular weight between entanglements M_e , in kg/mole, is given as follows:

$$M_e = 5.4 \cdot 10^3 \frac{\Sigma M}{\Sigma N} \left[\frac{\Sigma V}{\Sigma N} - 1.48 \cdot 10^{-5} \right]^{1/2} \quad (4)$$

In Eq. (4) the ratio (IM/IN) describes the averaged molecular weight per atom of main chain structure for the polymer repeat unit. The ratio (IV/IN) within the square root brackets of Eq. (4) correlates with the molar volume per main chain. If a functional group from Table 1 is introduced as a side chain unit the computation sets $N = 0$ for that group but introduces M and V for that group into Eq. (4). The constants $5.4 \cdot 10^3$ and $1.48 \cdot 10^{-5}$ in Eq. (5) are empirical factors which minimize the differences in experimental and calculated values of M_e . Since the chain length per main chain unit is roughly constant the square root term of Eq. (4) represents a measure of the cylindrical cross section area of the averaged polymer repeat unit. The type entangle described by Eq. (4) is associated with overlapping of the statistical chain coils.³ Interchain bonding by strong polar or hydrogen bonding interactions would tend to reduce M_e in a manner not described by Eq. (4).

RESULTS. The data of Table 1 and Eqs. (1)-(4) have been incorporated in an interactive micro-computer program with two sample computations shown in Table 2. The upper case of Table 2 shows the computational inclusion of eleven methylene groups in the side chain of polymethylmethacrylate to create poly-n-dodecylmethacrylate. The lower case of Table 2 illustrates the computational procedure for the typical SBR elastomer copolymer of styrene (S) and butadiene (B).

Table 2
Sample Computations for Methacrylates (Upper Case)
and Butadiene-Styrene Copolymers (Lower Case)

Unit No.	Moles	Structure Unit	Polymer Reference
I. Main Chain Units			
1	1	-CH ₂ -	ethylene
12	1	-C(CH ₃)(C(O))CH ₃ -	methyl methacrylate
II. Side Chain Units			
1	11	-CH ₂ -	ethylene
Glass Spec. Vol. (M^*M^*M/kg) = $9.89634E-04$ (CC/G) = 0.989634			
Glass C.E.D. (J/M^*M^*M) = $3.7802E+08$ (CAL/CC) = 90.3904			
Glass Temp (K) = 214.007 (C) = -59.1928			
Entang. MW (kg/mole) = 88.7177 (g/mole) = 88717.7			
I. Main Chain Units			
1	0.87	-CH ₂ -	ethylene
8	0.87	-CHCH-	1,4-butadiene
1	0.87	-CH ₂ -	ethylene
1	0.13	-CH ₂ -	ethylene
4	0.13	-CH(C ₆ H ₅)-	styrene
Glass Spec. Vol. (M^*M^*M/kg) = $1.00516E-03$ (CC/G) = 1.00516			
Glass C.E.D. (J/M^*M^*M) = $2.96893E + 8$ (CAL/CC) = 70.9575			
Glass Temp (K) = 208.462 (C) = -64.7382			
Entang. MW (kg/mole) = 2.58618 (g/mole) = 2586.18			

Table 3 shows the computed property trends for a series of alkylmethacrylate polymers and the copolymers of styrene and 1,4-butadiene. For both polymer series Table 3 shows good agreement between computed and experimental T_g values which is typical of such computations. The trends for M_e change with T_g are seen to be opposite for the two polymer series. A comparison of computed and experimental values of M_e is summarized in Table 4. The agreement is reasonable considering the broad range experimental estimates of M_e .

Table 3
Comparison of Calculated and Experimental T_g (Ref. 2,4)

Methacrylates	V_p (g/cc)	δ^2 (cal/cc)	T_g (C)	M_e (kg/mole)	T_g (exp) (C)	
methyl	0.829	144	107	18.2	105	
ethyl	0.861	131	63	23.1	61	
propyl	0.886	122	33	28.4	31	
butyl	0.907	115	12	34.0	12	
hexyl	0.938	105	-17	46.1	-19	
octyl	0.989	90	-36	59.3	-38	
dodecyl	0.989	90	-59	88.7	-62	
Butadiene-Styrene Copolymers						
Mole (B)	Mole (S)					
0	1	0.883	88	110	20.2	100
0.2	0.8	0.902	86	69	12.8	-
0.4	0.6	0.923	82	28	8.2	-
0.61	0.39	0.954	77	-14	5.0	-12
0.64	0.36	0.959	77	-20	4.7	-13
0.72	0.28	0.973	75	-35	3.9	-34
0.77	0.23	0.983	74	-45	3.4	-37
0.87	0.13	1.01	71	-64	2.6	-51,-60
0.95	0.05	1.03	68	-80	2.0	-71,-76
0.99	0.01	1.04	67	-88	1.8	-74
1.00	0	1.04	67	-90	1.7	-79,-87

Table 4
Calculated and Experimental Values of M_e

Polymer	M_e (kg/mole)	M_e (exp) (kg/mole)
poly-n-octylmethacrylate	59.3	87
poly-n-hexylmethacrylate	46.1	33.9
polymethylmethacrylate	18.2	4.7-10.0
polystyrene	20.2	17.3-18.1
styrene-butadiene copolymer (0.87 mole St, 0.13 mole Bd)	2.6	3.0
poly-1,4-polybutadiene	1.7	1.7-2.9

CONCLUSIONS. An interactive computer model for estimating four polymer physical properties from polymer chemical structure is introduced and demonstrated. This model is useful in computer aided polymer design and in extending or interpolating experimental data on polymer properties. Monomer sequence distribution as discussed by Johnston⁵ and semicrystallinity as discussed by Boyer⁶ complicate the use of this computational model for some polymers.

ACKNOWLEDGMENTS. This research was in part supported by the U.S. Army Research Office under Contract DAAG-29-80C-0137.

REFERENCES

1. R.A. Hayes, J. Appl. Polymer Sci. **5**, 318 (1961).
2. D.H. Kaelble, Physical Chemistry of Adhesion, Wiley-Interscience, New York, pp. 40-41, 282 (1971).

3. J.D. Ferry, Viscoelastic Properties of Polymers, 3rd Ed., Wiley, New York, Chap. 11 (1980).
4. L.A. Wood, J. Poly. Sci. 28, 319 (1958).
5. N.W. Johnson, J. Macromol. Sci. Rev. Macromol. Chem. C14(2), p. 215 (1976).
6. R.F. Boyer, J. Poly. Sci. Symposiums 50, p. 189 (1975).

APPENDIX 3

Relations Between Polymer Chemistry and Mechanical Properties

D.H. Kaelble Rockwell International Science Center
1049 Camino Dos Rios
Thousand Oaks, CA 91360

ACS Membership number MUST be indicated for at least one author _____
(Please use number as it appears on C&EN mailing label)

Work done at _____
Publication No. _____
Submitted for Presentation _____
Date of Submission _____
Author's Address _____

RELATIONS BETWEEN POLYMER CHEMISTRY AND MECHANICAL PROPERTIES. D. H. Kaelble.
Rockwell International Science Center, 1049 Camino Dos Rios, Thousand Oaks, California
91360.

A computer model is presented for direct estimation of time dependent modulus, strength, extensibility, and fracture toughness of polymers based upon a description of chemical structure. The model analyses the above mechanical properties in simple shear and tension. Polymer-diluent interactions are defined and properties can be computed for varied temperature and time conditions of mechanical loading. Polymer density, solubility parameter, glass temperature, and interchain entanglement molecular weight are computed from functional group structures of the polymer repeat unit. Assignment of polymer molecular weight and crosslink density permits computation of the time dependent modulus functions for shear and tension. Appropriate integration of variable modulus and strain produces the computed stress vs. strain curve and the fracture condition. The energy integral of the stress versus strain curve defines the fracture energy of the unnotched specimen.

RELATIONS BETWEEN POLYMER CHEMISTRY AND MECHANICAL PROPERTIES

D. H. Kaelble

Rockwell International Science Center
Thousand Oaks, CA 91360

INTRODUCTION. Generation of mathematical models to predict the mechanical response of polymers directly from chemical structure represents an important objective of polymer physics.^{1,2} In this discussion methods are presented for computer assisted estimation of the time dependent modulus, strength and extensibility and the unnotched fracture toughness of polymers based upon chemical composition and macromolecular structure. A molecular model for mechanical properties and cohesion of polymers proposed by Kaelble³ is implemented in these computer estimations. This computer model thus assembles quite diverse aspects of liquid-solid state theory and polymer rheology to describe mechanical properties and cohesion. The objective of this computer model is to provide a rapid and meaningful translation of chemical structure information into direct estimations of mechanical performances useful in plastics engineering.

CHEMICAL STRUCTURE PROPERTIES. The computer model requires as a minimum description of chemical structure the following six chemical structure properties³:

- V_p = polymer specific volume below T_g
- δ_p^2 = polymer solubility parameter squared (cohesive energy density) below T_g
- T_g = glass transition temperature
- M_e^g = interchain entanglement molecular weight (num. ave.)
- M_n = polymer molecular weight (num. ave.)
- M_c = molecular weight between chemical crosslinks (number ave.)

The upper four properties V_p , δ_p^2 , T_g , and M_e can often be calculated for the linear high polymer from five functional group properties which are⁴:

- U = the cohesive energy per group
- H = group contribution to rotational degrees of freedom
- N = number of main chain atoms per group
- V = group contribution to molar volume
- M = molecular weight per group

A combination of polymer (P) and soluble diluent (D) can be described in the above terms plus the addition of the following two parameters which are³:

- $\phi_p = 1 - \phi_D$ = volume fraction polymer
- ϕ = polymer - solvent interaction parameter (a pure number usually between 0.5 and 1.0)

With this fairly simple description of the polymer or polymer-diluent combination the computer model proceeds to calculate the "master curve" of time dependent shear modulus such as shown in the upper curve of Fig. 1. A second computation generates the stress versus temperature functions for mechanical yielding, fracture and flow as shown in the lower curves of Fig. 1. These two sets of curves in Fig. 1 represent the first translation of the polymer chemistry into polymer physical state diagrams which are otherwise obtained by extensive rheological and mechanical testing.¹⁻³

MECHANICAL RESPONSE ESTIMATION. The mechanical response model proposed by Kaelble³ treats stress effects upon free volume. The predicted effect of mechanical loading in shear or tension is to increase free volume and as a consequence increased molecular motion. The predicted transitions from solid to rubber to flow state thus appear in a stress versus strain curve as

st type
+ this

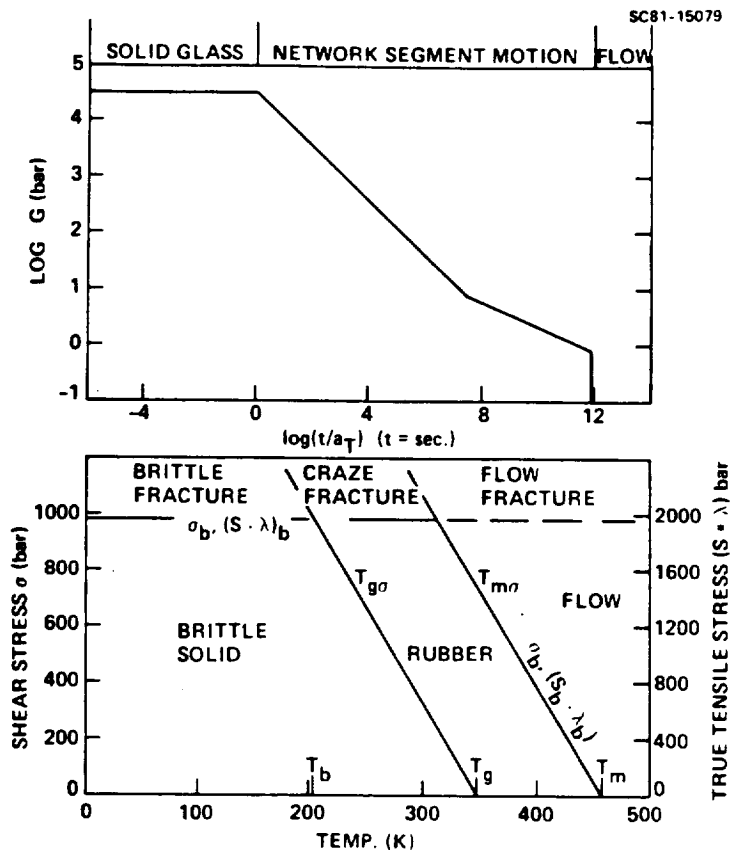


Figure 1

the yield stress followed by the flow or fracture stress. A simple variation on the familiar WLF equation of Williams, Landel, and Ferry is employed as follows³:

$$\log\left(\frac{1}{a_T}\right) = \log\left(\frac{\tau_g}{\tau_{g\sigma}}\right) = \frac{17.4(T - T_{g\sigma})}{51.6 + T - T_{g\sigma}} > -30 \quad (1)$$

where a_T is the dimensionless time shift factor, τ_g the glass transition relaxation time at zero stress ($\sigma = 0$), and $\tau_{g\sigma}$ the glass transition relaxation time at stress σ , T = test temperature and $T_{g\sigma}$ the glass temperature at stress σ .

As shown in the lower curves of Fig. 1 the magnitude of $T_{g\sigma}$ is decreased by increased stress thereby increasing the value of $\log(1/a_T)$ as defined by Eq. (1). In upper Fig. 1, with the test time t either constant or increasing with stress σ , the decrease in $\log(1/a_T)$ will increase the magnitude of $\log(t/a_T)$ displayed on the abscissa of the diagram. The prediction is that increased stress σ will increase $\log(t/a_T)$ and thereby decrease the shear modulus G as shown by the master function of upper Fig. 1. This general concept that stress and temperature affect the rheological response through Eq. (1) is exploited in the numeric analysis of a computed stress versus strain and fracture response.

The relation between shear stress and strain is defined by the following integral equation³:

$$\sigma = f(\lambda) \int_0^{\lambda} G(t/a_T) d\gamma \quad (2)$$

where $f(\lambda)$ is an appropriate function of extension ratio λ which accounts for chain orientation. The reduced time shear modulus $G(t/a_T)$ is the tangent slope of the shear stress σ versus strain γ curve at external test time t and concurrent internal polymer reduced time a_T as defined by Eq. (1). The relation between nominal tensile stress S and strain ϵ is defined by a similar integral equation³:

$$S = f_1(\lambda) \int_0^{\epsilon} E(t/a_T) d\epsilon \quad (3)$$

where $f_1(\lambda)$ is the appropriate function of extension ratio for tensile deformation and chain orientation. The reduced time tensile modulus $E(t/a_T) \approx 3 G(t/a_T)$ forms the tangent slope of tensile stress-strain curve at time t and reduced time a_T .

The stress-strain curves defined by Eq. (2) and Eq. (3) are generated by numeric integration where the external test time t and polymer response time $(1/a_T)$ are combined to define the incremental slope $E(t/a_T) \approx 3 G(t/a_T)$. The respective fracture energy per unit volume in shear W_s and tension W_T are defined by the stress-strain integrals as follows³:

$$W_s = \int_{\gamma=0}^{\gamma_b} \sigma d\gamma \quad (4)$$

$$W_T = \int_{\epsilon=0}^{\epsilon_b} S d\epsilon \quad (5)$$

which represent the areas beneath the respective stress-strain curves. The magnitudes of W_s and W_T represent the fracture energy per unit volume of unnotched polymer deformed under uniform stress and strain.

STRUCTURAL RELIABILITY AND THE FAILURE ENVELOPE. Structural reliability R_W is here defined as the statistical probability of load supporting ability (nonfailure) under a defined set of general environmental conditions which include mechanical stress and strain, temperature, and loading time. A multidimensional failure envelope can be defined by the extreme value statistics introduced by Weibull into the widely used models of structural reliability.^{5,6} Three principal failure responses can be incorporated into the following Weibull type definition for structural reliability as follows⁷:

$$R_W = \exp\left(-\left(\frac{\sigma}{\sigma_b}\right)^{m(\sigma)}\right) \exp\left(-\left(\frac{\lambda}{\lambda_b}\right)^{m(\lambda)}\right) \exp\left(-\left(\frac{t}{t_b a_T}\right)^{m(t)}\right) \quad (6)$$

$$= R_{\sigma} * R_{\lambda} * R_t$$

where σ_b , λ_b , and t_b are respectively described as the nominal strength, extension ratio, and load endurance time where $R_W = 1/e = 0.37$ for each process acting independantly. The parameters σ , λ , and t represent the applied stress, extension ratio, and load dwell time. The presence of a_T from Eq. (1) in the last term of Eq. (5) introduces the reduced variables criteria into the time dependent failure term. The Weibull factors $m(\sigma)$, $m(\lambda)$, and $m(t)$ define respective distribution shape factors. Since R_W is

the product of the three exponential decay terms, Eq. (6) assumes that these mechanisms interact in series to give a conservative estimate of structural reliability.

RESULTS. The model polymer described by the curves of Fig. 1 is a high molecular weight polyvinyl chloride polymer with the following chemical structure properties: $V_p = 0.71$ cc/gm, $\delta^2 = 94.1$ cal/cc, $T_g = 348$ K, $M_e = 6490$ gm/mole, $M_p = 8.32 \cdot 10^5$ gm/mole^P and $M_c = 8.32 \cdot 10^{58}$ gm/mole to reflect no crosslinking. The computed curves of nominal tensile stress and strain are shown in the upper view of Fig. 2. The stress-strain curve number and the associated computation temperature are listed in Table 1. The lower curve of Fig. 2 shows the fracture energy rise from brittle failure values at 220 K which maximize near room temperature and diminish toward zero at the flow temperature $T_m = 458$ K. The experimental deformation and failure properties of an unplasticized PVC polymer of $T_g = 346$ K and weight average molecular weight $\bar{M}_w = 1.16 \cdot 10^6$ gm/mole have been previously reported^{3,8} and display reasonable agreement with the computed results shown in Fig. 2. In the experimental study the tensile strength S_b and extensibility displayed a well defined failure envelope as shown in the lower portion of Fig. 3. One notes in comparing upper Fig. 2 and Fig. 3 that the strength $S_b = 50$ bar at maximum extensibility $\epsilon_b = 9.0$ is in good agreement with experiment. Experimental strength and extensibility data for temperatures below T_g are shown in Fig. 3 to be widely scattered. These low temperature data can be converted to true tensile stress $S_b \lambda_b$ where $\lambda_b = \epsilon_b + 1$ is the extension ratio at break.

Table 1
Relation of Stress-Strain Curve Number to Test Temperature

Curve No.	Temp (K)	Curve No.	Temp (K)	Curve No.	Temp (K)
1	180	8	285	15	390
2	195	9	300	16	405
3	210	10	315	17	420
4	225	11	330	18	435
5	240	12	345	19	450
6	255	13	360	20	465
7	270	14	375	21	480

In Fig. 4 the 26 experimental true tensile stress values fall on a modified Weibull type distribution function where the shape factor $m(\sigma)$ changes from 5.26 to 1.65 as $R(\sigma)$ decreases. This type of bimodal Weibull function has been observed and discussed previously with regard to polymer cavitation processes.⁹ By utilizing the experimental relation of $R(\sigma)$ versus true tensile strength $S_b \lambda_b$, curves of constant $R(\sigma)$ and $S_b \lambda_b$ can be defined for the failure data of Fig. 3. Inspection shows that these functions satisfactorily enclose the upper branch of the failure envelope of Fig. 3 which is dominated by the stress criteria of failure described by the $R\sigma$ mechanism of Eq. (6).

A single example illustrates the use by which the computer model permits investigation of changes in chemical structure properties on mechanical response. The high molecular weight thermoplastic PVC response shown in Fig. 2 can be modified by crosslinking. The curves of Fig. 5 show the same model PVC polymer of Fig. 2 which is modified by a single molecular structure change which is a low molecular weight between crosslinks of $M_c = 500$ gm/mole.

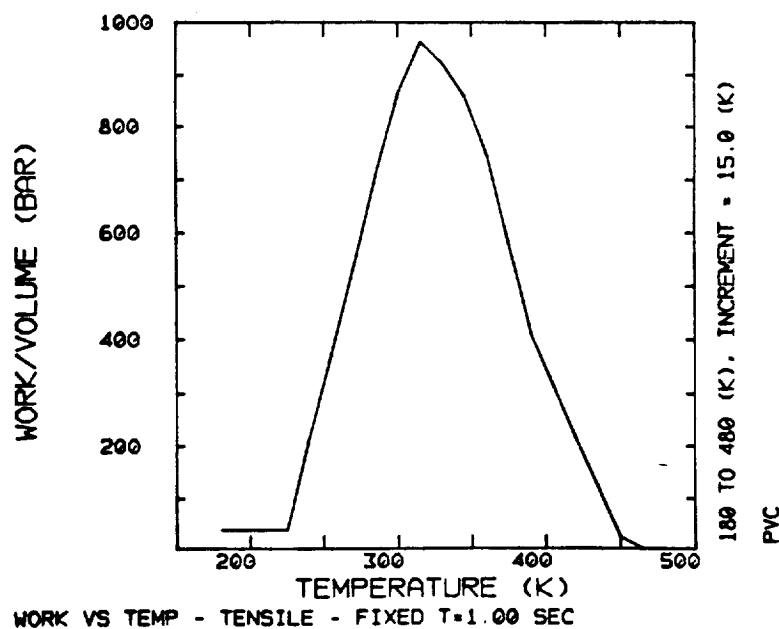
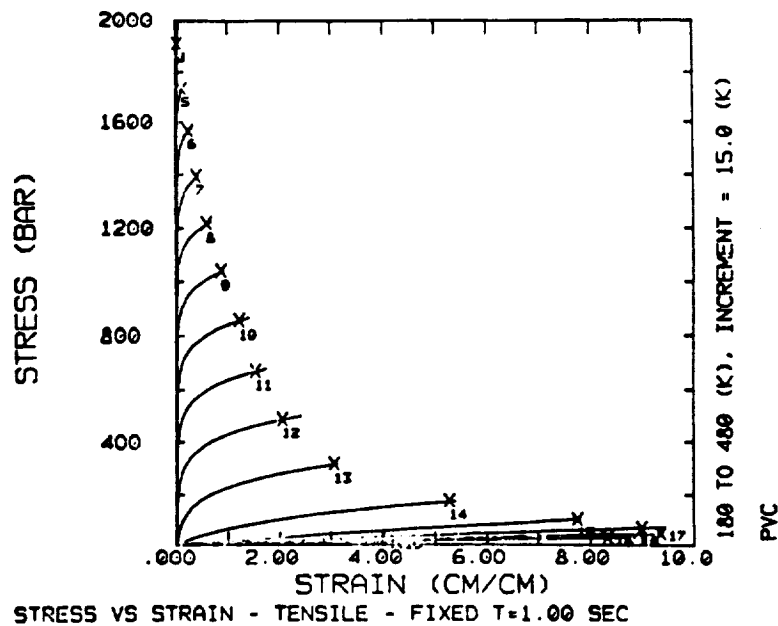


Figure 2

This high crosslink density of $(1/V_{P.C.}) = 2.82 \cdot 10^{-3}$ (moles/cc) is typical of fully crosslinked thermoset resins such as epoxies. The effect of this simulated dense crosslinking is to raise the stress and lower the polymer extensibility as shown in the upper curves of Fig. 5. The effects of chain orientation are dominant at temperatures well above T_g (see curves 15-19) where the stress strain curves and failure points are controlled by the equilibrium network modulus. The lower curve of Fig. 5 shows the narrow temperature span and lower magnitude of fracture energy produced by dense crosslinking. These same results are displayed in intercomparisons of experimental deformation and fracture master curves for thermoplastic PVC and thermoset epoxy resins at corresponding free volume states where effects of chemical structure dominate mechanical properties.^{3,8}

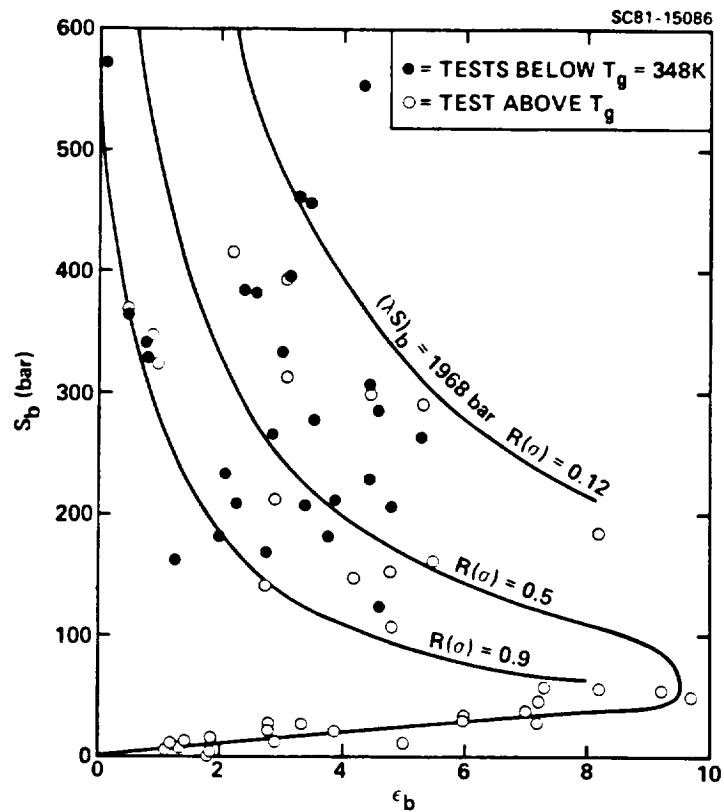


Figure 3

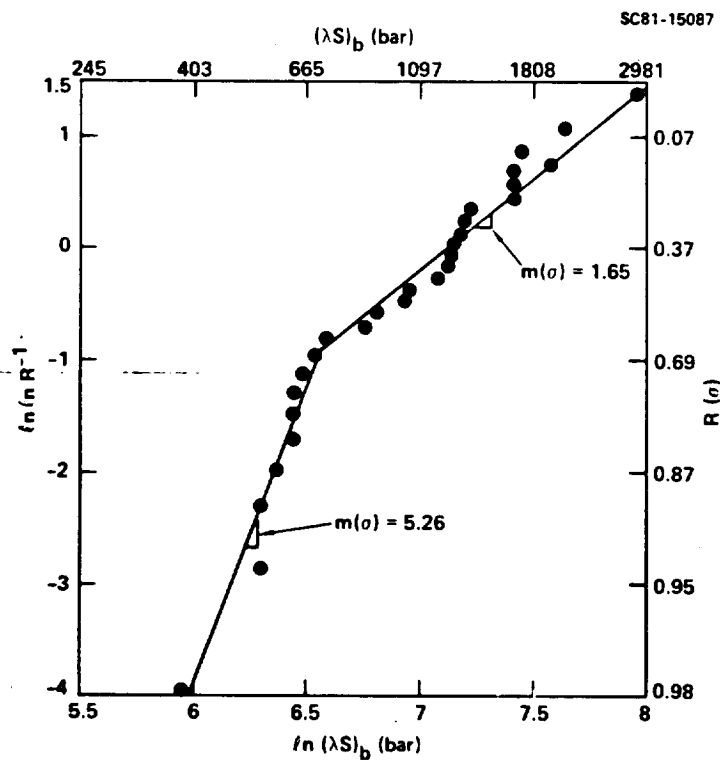


Figure 4

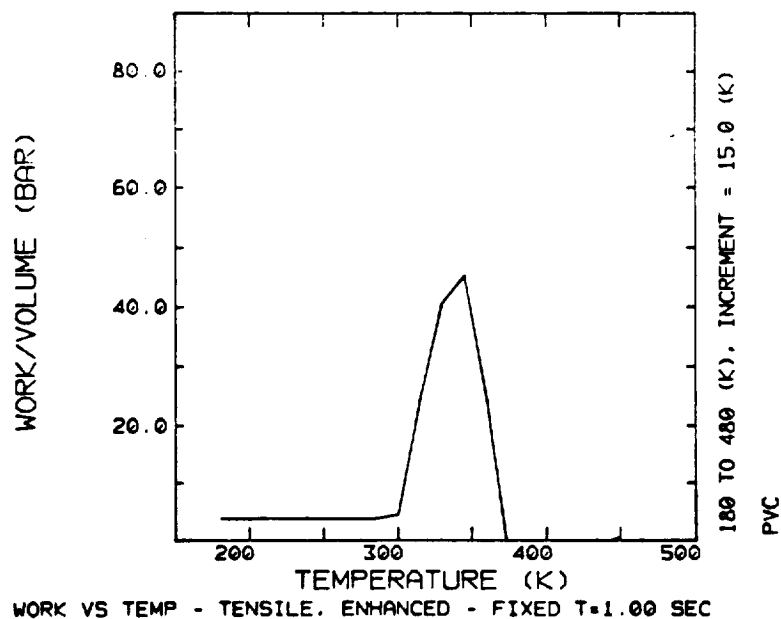
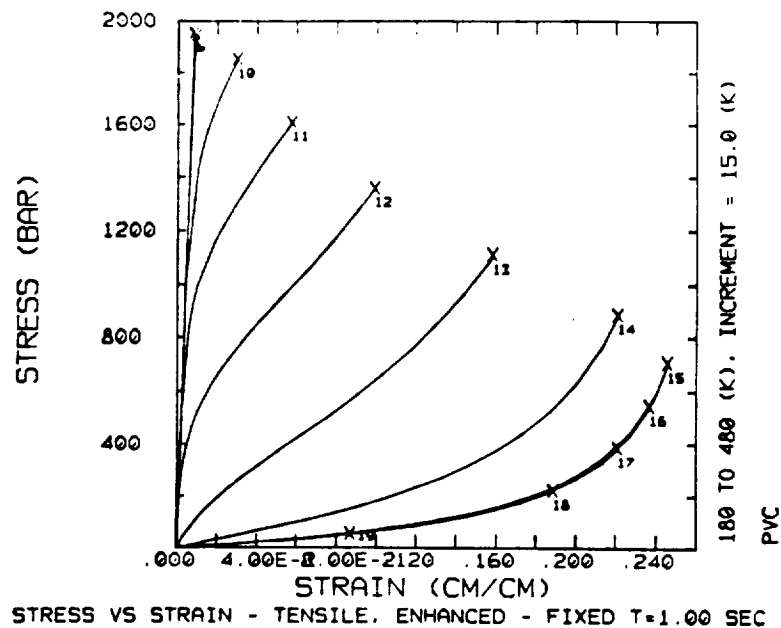


Figure 5

CONCLUSIONS. An interactive computer model for estimating the stress versus strain response, deformation and fracture response of polymers is introduced and demonstrated.

This model is useful in evaluating the engineering response of model polymer systems where the variations include both chemical composition and macro-molecular structure. In current research this model is being exploited in studies to optimize polymer fabrication and curing processes relating to structural adhesives and advanced composites.

ACKNOWLEDGEMENTS. This research was in part supported by the U.S. Army Research Office under Contract DAAG-29-80C-0137.

REFERENCES

1. J. D. Ferry, Viscoelastic properties of Polymers, 3rd Ed, Wiley, New York (1980).
2. I. M. Ward, Mechanical Properties of Solid Polymers, Wiley-Interscience, London, (1971).
3. D. H. Kaelble, Physical Chemistry of Adhesion, Wiley-Interscience, New York, (1971), Chap. 11.
4. D. H. Kaelble, "Relations Between Polymer Chemistry and Physical Properties," Amer. Chem. Soc. Div. of Plastics and Coatings Preprint Vol. 46 (April, 1982).
5. W. Weibull, J. Appl. Mech. 18, (1951), p.293.
6. N. R. Mann, R. E. Shafer, and N. D. Singpurwalla, "Methods of Statistical Analysis of Reliability and Life Data," Wiley, New York, (1974).
7. D. H. Kaelble, "Polymer Composite Reliability," U.S. Air Force Technical Report AFML-TR-78-205, pp. 193-207.
8. D. H. Kaelble, Treatise on Adhesion and Cohesion, (R.L. Patrick, Editor) Vol. 1, Chap. 5, Dekker, New York (1967).
9. D. H. Kaelble and E. H. Cirlin, J. Poly. Sci: Symposium No.43 (1973), p. 131.

FIGURE CAPTIONS

- Figure 1. Calculated shear modulus G versus reduced relaxation time t/a_T (upper curve) and stress-temperature functions for yield and fracture (lower curves).
- Figure 2. Computed estimates of nominal tensile stress versus strain response and failure (indicated by x in upper curves) and fracture energy (lower curve) of linear polyvinyl chloride ($T_g = 348 \text{ K}$, $M_n = 8.53 \cdot 10^5 \text{ gm/mole}$).
- Figure 3. Experimental values of nominal tensile strength S_b versus extensibility ϵ_b for polyvinyl chloride film ($T_g = 346 \text{ K}$, $M_w = 1.16 \cdot 10^6 \text{ gm/mole}$).
- Figure 4. Experimental reliability distribution $R(\sigma)$ for true tensile strength $(\lambda S)_b$ of polyvinyl chloride below T_g .
- Figure 5. Computed estimates of nominal tensile stress versus strain response (upper curves) and fracture energy (lower curve for crosslinked



The International Corrosion Forum Sponsored By the National Association of Corrosion Engineers / April 6-10, 1981 / Sheraton Centre, Toronto, Ontario, Canada.

ATMOSPHERIC CORROSION MODEL AND MONITOR FOR LOW COST SOLAR ARRAYS

DAVID H. KAEUBLE, FLORIAN B. MANSFELD, SAMUEL L. JEANJAQUET AND MARTIN KENDIG

Science Center, Rockwell International

Thousand Oaks, CA 91360

ABSTRACT

An atmospheric corrosion model and corrosion monitoring system has been developed for low cost solar arrays (LSA). The corrosion model predicts that corrosion rate is the product of the surface condensation probability of water vapor and the diffusion controlled corrosion current. This corrosion model is verified by simultaneous monitoring of weather conditions and corrosion rates at the solar array test site at Mead, Nebraska.

INTRODUCTION

A review of solar cell corrosion resulted in the formulation of a set of multiple working hypotheses which qualitatively define the causation, microprocesses, and macroscopic effects of corrosion in LSA. This set of 10 multiple working hypotheses are briefly summarized as follows.

Causation

1. Silicone (and other polymeric) encapsulants are permeable to water, oxygen and other gases whose reaction products can lead to further corrosion of the metallic substrates and interfaces in LSA.
2. Corrosion products or salts not removed in the fabrication process will greatly accelerate the corrosion processes by forming corrosive aqueous electrolyte with the species diffusing through the encapsulant.

Microprocesses

3. Corrosion initiates at interfacial defect sites where aqueous electrolyte is concentrated.

Publication Right

Copyright by the author(s) where copyright is applicable. Reproduced by the National Association of Corrosion Engineers with permission of the author(s). NACE has been given first rights of publication of this manuscript. Requests for permission to publish this manuscript in any form, in part or in whole, must be made in writing to NACE, Publications Dept., P.O. Box 218340, Houston, Texas 77218. The manuscript has not yet been reviewed by NACE, and accordingly, the material presented and the views expressed are solely those of the author(s) and are not necessarily endorsed by the Association.

Printed in USA

4. A condensed aqueous phase in the defect site is required for corrosion.
5. Moisture condensation is maximized in voids with hygroscopic contents and hydrophilic surfaces.
6. If interfacial voids are initially isolated, then isolated micro-corrosion sites can be located by scanning Auger microscopy (SAM).
7. When corrosion products accumulate, these corrosion sites should grow and coalesce with growth rates resolvable by SAM.

Macroscopic Effect

8. At some point, accumulation of corrosion products and corrosion site growth will influence both macroscopic appearance and solar energy conversion efficiency.
9. Chemical (UV) degradation of encapsulant can produce new degradation products, voids, and increased hygroscopic response which accelerates and possibly modifies the mechanism of corrosion.
10. Accumulation of hygroscopic and hydrophilic dirt further promotes water absorption and retention.

These hypotheses stress the interactive role of interfacial defects and condensed moisture in corrosion, and isolate causation factors from macroscopic effects. A combined predictive model and experimental test plan for encapsulant effects on atmospheric corrosion which utilize these initial hypotheses was the main objective of this program. The principle parameters utilized in the corrosion model are summarized in Table 1.

ATMOSPHERIC CORROSION MODEL

The multiple hypothesis described above points out that atmospheric corrosion involves combined condition of condensed moisture to provide the electrolyte and ionic conductivity at the corroding surface or interface. The condensation probability of moisture on a surface can be calculated based on an extension of conventional nucleation theory as briefly reviewed by Adamson.¹ Extension of the conventional nucleation theory by consideration of the role of surface energetics and condensate wettability is provided in a derivation by Kaelble² for nucleation of cavities at interface. The central assumption in this discussion is that the rate restriction to condensation is associated with the extra surface energy of small condensation nuclei which diminish the probability of droplet formation.

Based upon the above references and the nomenclature of Table 1 the following relations are readily derived for the process:

$$nA(\text{gas at pressure } P) + A_n(\text{small liquid drop})$$

The probability P_c of forming condensed droplets of n molecules from $n-1$ molecules is stated as follows:

$$P_c = \frac{I}{I_0} = \exp\left[\frac{-1.756 \times 10^{22} \phi v^2 \gamma_{LV}^3}{T^3 (\ln P/P_0)^2}\right] \quad (1)$$

where for liquid-solid contact angle $0 < \theta < 180$ the wettability parameter ϕ is²:

$$\phi = 0.25[2 + \cos^3 \theta - 3 \cos \theta] \quad (2)$$

The condensation temperature shift due to surface capillary curvature is defined by the following modified Kelvin relation¹:

$$\Delta T = \frac{-2 v \gamma_{LV} T_0}{\Delta H_v r_c} \quad (3)$$

Following normal convention r_c is negative for concave curvature of internal capillaries. The probability P_c versus temperature T curve is shifted along the temperature axis by ΔT to define a new reduced temperature

$$T_r = T + \Delta T \quad (4)$$

for condensation on a rough surface with capillary radius r_c . A computer program has been developed which calculates both P_c vs T and P_c vs T_r . This computer model incorporates the surface and bulk properties of water as a function of temperature as shown in Fig. 1. The upper view of Fig. 2 shows the logarithm of the condensation probability P_c versus dew point minus surface temperature ($T_0 - T$) for three solid surfaces. The solid surfaces are defined by a temperature invariant surface tension γ_{sv} which is described by the following relation²:

$$\gamma_{sv} = \gamma_{sv}^d + \gamma_{sv}^p \quad (5)$$

where the superscripts d and p describe the respective dispersion and polar components of solid-vapor surface tension. The temperature dependent surface properties of water are also described by dispersion and polar components where the ratio $\gamma_{lv}^d / \gamma_{lv}^p = 0.43$ is assumed temperature independent. For computational convenience the following parameters²:

$$\alpha_L = (\gamma_{LV}^d)^{1/2}, \beta_L = (\gamma_{LV}^p)^{1/2}$$

$$\alpha_s = (\gamma_{SV}^d)^{1/2}, \beta_s = (\gamma_{SV}^p)^{1/2}$$

are substituted for these surface tension components. The computation of temperature dependent liquid solid contact angle θ or $\cos \theta$ is provided by the following work of adhesion relation²:

$$\cos \theta = \frac{2(\alpha_L \alpha_s + \beta_L \beta_s)}{\gamma_{LV}} - 1 < 1.0 \quad (6)$$

The solid surface properties α_s and β_s influence the temperature dependent values of $\cos \theta$ of Eq. (6) and thereby modify the wettability parameter of Eq. (1) and Eq. (2).

The important new feature of the condensation model presented in Eq. (1) is, of course, the capability to incorporate the effects of surface wettability in the computation of the probability of condensation, P_c , versus temperature or relative humidity. The curves of Fig. 2 show the large differences in P_c versus surface temperature T_s or the surface supersaturation temperature $(T_0 - T_s)$ produced by relatively small changes in solid surface properties α_s and β_s . The surface energy diagrams of Fig. 3 shows the variations in water surface tension properties from 263 K to 383 K in terms of α vs β . The α_s versus β_s properties chosen for calculation in Fig. 2 are shown to lie close to water surface properties and therefore display relatively good water wettability typical of corroding metal surfaces.

The second important aspect of atmospheric corrosion deals with the ionic conduction processes at the corroding surface or interface. The following relations define diffusion controlled corrosion for the following metal (M) oxidation process⁴:



The equilibrium between the electrolytic solution and the surface is described by the following classical relation⁴:

$$E_2 - E_1 = - \frac{RT}{nF} \ln \left(\frac{M^{+n}}{M_s^{+n}} \right) \quad (7)$$

Where the corrosion process displays a diffusion limited ionic conductivity, the kinetics are described by the following standard relation⁴:

$$E_2 - E_1 = - \frac{RT}{nF} \ln \left(\frac{I_L}{I_L - I} \right) \quad (8)$$

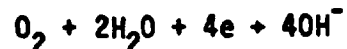
The limiting diffusion current density ($I_L = \text{Amp/m}^2$) is defined by the following relation⁴:

$$I_L = \frac{nFDC}{\delta t} \quad (9)$$

where the nomenclature of lower Table 1 define the electrochemical parameters of Eqs. (7-9). The maximum corrosion rate for atmospheric corrosion controlled by combined condensation probability P_c and limiting diffusion current I_L is given by the following simple expression⁴:

$$I = P_c I_L = P_c \frac{nFDC}{\delta t} \quad (10)$$

For atmospheric corrosion the limiting current I_L is usually established by the corrosion reaction in which oxygen is the cathodic reactant as follows⁴:



The maximum corrosion rate I_L can be readily calculated for cases where surface condensation has occurred with $P_c = 1.0$. Taking the concentration of

dissolved O_2 in water at 298K as $C = 1.0 \text{ mol/m}^3$, the diffusion coefficient $D = 1.10^{-9} \text{ m}^2/\text{s}$, diffusion layer thickness $= 5.10^{-4} \text{ m}$ and number of electrons $n=4$ and $t = 1.0$ shows a predicted maximum corrosion current density i_{max} as follows⁴:

$$i_{\text{max}} = 0.77 \text{ Amp/m}^2 (77 \text{ } \mu\text{A/cm}^2)$$

In Eq. (10) we can presume that i_L will appear as a system constant once corrosion has advanced beyond the initiation phase described by the macro-processes outlined in the Introduction. The environmental variation in the surface corrosion rate of an unprotected metal surface would be expected to vary with moisture condensation probability P_c .

ATMOSPHERIC CORROSION MONITORING

Technical details of atmospheric corrosion monitors (ACM) developed by the Science Center and employed in Mead site corrosion studies are presented in a published report.³ Four ACM units were fabricated for this program following the design of reference (3) using ten alternating plates of copper and zinc separated by a $50 \text{ } \mu\text{m}$ insulative film separator (DuPont Mylar polyester). This assembly was held together by nylon bolts and encapsulated in a castable epoxy so as to expose only one surface. This surface was polished to expose the edges of the Cu/Zn plates to provide the active corrosion monitoring surface.

Two atmospheric corrosion monitors were installed at the Mead, Nebraska site on July 12, 1979 as shown in Fig 4. One corrosion sensor is bare so as to represent a corrosion response in the absence of encapsulant protection. The second corrosion cell is covered with 2 mm SYLGARD 184 encapsulant over a reactive primer GE-SS4155. The reactive primer is applied to provide a moisture-resistant bond between the SYLGARD 184 encapsulant and the metal plates of the corrosion monitor.

The output of the corrosion monitors is connected into the data acquisition system at Mead. The records of the corrosion monitors at Mead can be correlated with concurrent recordings of environmental variables. Corrosion rates of the bare and Sylgard 184 encapsulated monitor can be intercompared to isolate the discrete role of the encapsulant. Two equivalent corrosion cells have been retained at the Science Center for accelerated aging studies.

The data acquisition system at Mead provides automatic recording and digital printout of data at 10 min intervals. With the kind cooperation of Dr. Steve Forman and Mr. Ray Hopkinson of the M.I.T. Lincoln Laboratories arrangements were made whereby these digital printouts have been sent to the Science Center

on a monthly basis from August 1, 1979 through Jan. 31, 1980. These records have been analyzed to isolate both typical and significant climatic and corrosion correlations. An intercomparison between ambient temperature and solar array string temperature for a continuous 56 hour period is shown in Fig. 5. The upper abscissa of Fig. 5 identifies the morning (A.M.) and evening (P.M.) periods through the 24 hr. day. The lower abscissa records the cumulative hours. During the mid-day hours 10-19 both ambient temperature and string temperatures achieve characteristic maximum values as shown in Fig. 5. On day 221 which is evidently clear and sunny at midday one notes in Fig. 5 that the string temperature at hour 13 (1 P.M.) rises 22°C above ambient indicative of light absorption and thermal output by the solar array. On day 222 which is cooler and cloudy the string temperature rises only 11°C above ambient at hour 10 (10 A.M.). These daily variations and day-to-day differences typify the summertime climatic records for the Mead test site. The concurrent precipitation, atmospheric moisture and corrosion monitor data for this period are shown respectively in the lower, middle and upper views of Fig. 6.

The lower curve of Fig. 6 shows that brief periods of precipitation occur at hours 7 and 20-23. The upper curves of Fig. 6 show the corrosion current outputs of the bare metal exposed and RTV silicone coated corrosion monitors. Note that the ordinate scale of these upper curves is logarithmic to display a 10,000 fold range of corrosion current I . The upper curves of Fig. 6 show two periods of variable corrosion current output for the uncoated corrosion monitor during periods when relative humidity exceeds 80% R.H.. The RTV silicone coated unit is passive with constant current $I = 0.04 \mu\text{A}$ (micro amps.) during these two periods of high atmospheric moisture. This passive response of the coated monitor shows quantitatively that the RTV silicone coating is providing a complete corrosion protection and moisture isolation function within the sensitivity range of measurement.

Inspection of Fig. 6 shows that the unprotected ACM (atmospheric corrosion monitor) corrosion current rises and falls as a direct function of both relative humidity (RH) or moisture supersaturation temperature ($T_D - T$) during high moisture conditions. Conversely, precipitation produces no special corrosion response not already related to atmospheric moisture saturation level.

The scale of relative humidity shown in Fig. 6 is not fully informative of atmospheric moisture conditions. During periods when $\text{RH} = 100\%$ the degree of moisture supersaturation is not defined. The scale of moisture supersaturation (dew point minus ambient temperature), as shown in Fig. 6 continues to describe this important region of high moisture and corrosion response and therefore is preferable to RH as a climatic indication of corrosion processes.

The curves of corrosion current ($\log_{10} I$) versus supersaturation temperature ($T_D - T$) shown in Fig. 7 clearly indicate the reversible transition in corrosion rate with level of moisture supersaturation for two cycles of condensation and subsequent surface drying. This type of reversible corrosion rate response shown in Fig. 6 and Fig. 7 was characteristic of warm weather response for Mead data for the uncoated ACM unit.

The lower limiting value of corrosion current $I = 0.04 \mu A$ shown in Fig. 7 reflects the lower sensitivity of measurement. At this lower current output the dry uncoated ACM and RTV coated ACM are equivalent. As shown in Fig. 7 with increasing supersaturation temperatures ($T_D - T$) the corrosion current displaces an upper limiting value $I = 15 \mu A$. Referring to the corrosion model developed in Eq. 1 and Eq. (10) this upper limiting current refers to the condition where condensation probability $P_c = 1.0$ and the current equals the limiting diffusion current $I = I_L$. The transition region in corrosion current output, where $(T_D - T) = -3.6$ to 0.3 , correlates with the rapid variation in $\log P_c$ predicted by Eq. (1) and shown graphically in the calculated curves of Fig. 2.

During winter weather and particularly during the freeze-thaw periods the response of the uncoated ACM displays a more complicated relation to moisture and temperature. The curves of Fig. 8 and Fig. 9 show a six day period in December 1979 which typifies winter Mead site ACM response. The RTV silicone coated ACM unit continues to show lower limit current $I = 0.04 \mu A$ under all climate conditions indicative of continued protection from all environmental corrosion stresses.

The uncoated ACM output shown in Fig. 8 and Fig. 9 now appears to respond in a complicated fashion to both atmospheric moisture ($T_D - T$) and temperature relative to freeze-thaw at $T = 0^\circ C$. The corrosion model and Eq. (10) would reasonably ascribe this result to temperature dependence of limiting diffusion current I_L and lower ionic conductivity for ice as compared to liquid water. Both ionic solubility C and diffusion coefficient D become potentially strong functions of temperature near $T = 0^\circ C$ as described in the parameters of Eq. (10).

The Mead corrosion and climatology recordings thus far support the preliminary hypothesis and corrosion model. Corrosion can occur at lower relative humidity due to surface capillarity condensation described by the corrosion model in Eq. (3). Typical reported values⁵ for surface porosity and capillarity of corroded surface films is $r_c = -1 \times 10^{-9} m(10A)$. The calculations of Fig. 2 assume a somewhat larger value of $r_c = -5 \times 10^{-9} m$. The rapidly varying value of condensation probability P_c accounts for the large shifts in corrosion rate with degree of atmospheric moisture saturation. During winter

periods the change in ice-liquid states of surface condensed moisture is seen to modify experimental corrosion rates by predicted variations in the diffusion controlled current I_L .

The ability of the RTV silicone coating to inhibit ACM corrosion processes is clearly shown. In terms of the corrosion model and Eq. (10) the RTV silicone coating lowers both P_c and I_L at the encapsulant/metal interface sufficiently to effectively protect the coated ACM unit during the entire six month period of recorded Mead site exposure (from August 1979 through January 1980). Continued surveillance of these ACM units for over one year of Mead exposure (through September 1980) show a continuation of responses reported above for the first six months of exposure.

CONCLUSIONS

- a. An atmospheric corrosion model has been developed which predicts the corrosion rate as controlled by surface condensation, and diffusion limited current.
- b. Atmospheric corrosion monitor (ACM) data from Mead site verify the predictions of the atmospheric corrosion model.
- c. Uncoated ACM data shows corrosion rate to correlate directly with surface moisture condensation.
- d. Silicone primed and coated ACM data show that by lowering the limiting diffusion current at the metal-encapsulant interface that corrosion is essentially inhibited.

ACKNOWLEDGEMENT

This paper presents the results of research conducted under JPL Subcontract 954739 which forms part of the JPL Low-Cost Solar Array Project sponsored by the U.S. Department of Energy.

REFERENCES

1. A. W. Adamson, Physical Chemistry of Surfaces, 2nd Ed. Interscience, N.Y., (1967), p. 375-387.
2. D. H. Kaelble "Cavitation in Viscoelastic Media," Trans. Soc. Rheology, 15, 275 1971.
3. F. Mansfeld and J. V. Kenkel, "Electrochemical Measurements of Time-of-Wetness and Atmospheric Corrosion Rates, Corrosion, 33 (1), p. 13-16, (1977).

4. L. L. Shreir, Corrosion, 2nd Ed., Vol. 1, Newnes-Butterworths, London (1976), p. 1:87-100.
5. L. L. Shreir, Ibid., p. 1:254, 2:31.

Table 1

Meaning of Symbols for Corrosion Model

Part 1: Condensation Probability

<u>Symbol</u>	<u>Meaning</u>
ΔF	free energy of drop formation
ΔF_m	maximum free energy of drop formation
ϕ	wettability parameter
θ	liquid - solid contact angle
γ_{LV}	liquid - vapor surface tension
r	drop radius
r_c	surface capillary radius
P	liquid vapor pressure
P_0	saturated liquid vapor pressure
N_0	Avagadro's Number
R	gas constant
T	kelvin temperature
T_0	kelvin temperature for liquid-vapor saturation
H_v	water heat of vaporization
v	water molar volume
I	rate of condensation (drops/m ³ s)
I_0	maximum rate of condensation
P_c	condensation probability
ΔT	temperature shift due to capillary condensation

Part II: Diffusion Controlled Corrosion

M^{+n} , M_s^{+n} = respective ion concentrations in solution and at electrode surface

E_2 = oxidation potential of electrode with current density I

E_1 = oxidation potential without current

I = current density (amperes/m²)

I_L = limiting current density

D = diffusion coefficient of reducing ion

n = number of electrons

F = Faraday (96500 coulombs/equivalent)

C = concentration of diffusing ions (moles/m³)

δ = thickness of diffusion layer ($\approx 5 \times 10^{-4}$ m in static solution)

t = transfer number of all ions in solution (≈ 1.0 if many other ions present).

FIGURE CAPTIONS

- Fig. 1 Temperature dependence of water properties.
- Fig. 2 Condensation probability ($\log_{10} P_c$) vs. surface temperature (T_s) for three values of solid surface energy (α_s, β_s).
- Fig. 3 Surface properties of water plotted on a surface energy diagram of dispersion (α) vs. polar (β) forces.
- Fig. 4 Photographic view of Mead, Nebraska LSA test site (upper view) and atmospheric corrosion monitors (lower view) installed on rear right portion of array.
- Fig. 5 Comparative Mead site ambient and solar array string temperatures.
- Fig. 6 Corrosion Monitor (upper view) correlation to Mead site moisture and rain climatology.
- Fig. 7 Corrosion Monitor current (I) vs. moisture super saturation temperature ($T_D - T$).
- Fig. 8 Corrosion Monitor (upper view) correlation to Mead site climatology for freeze-thaw periods.
- Fig. 9 Further corrosion Monitor (upper view) correlation to Mead site climatology for freeze-thaw periods.

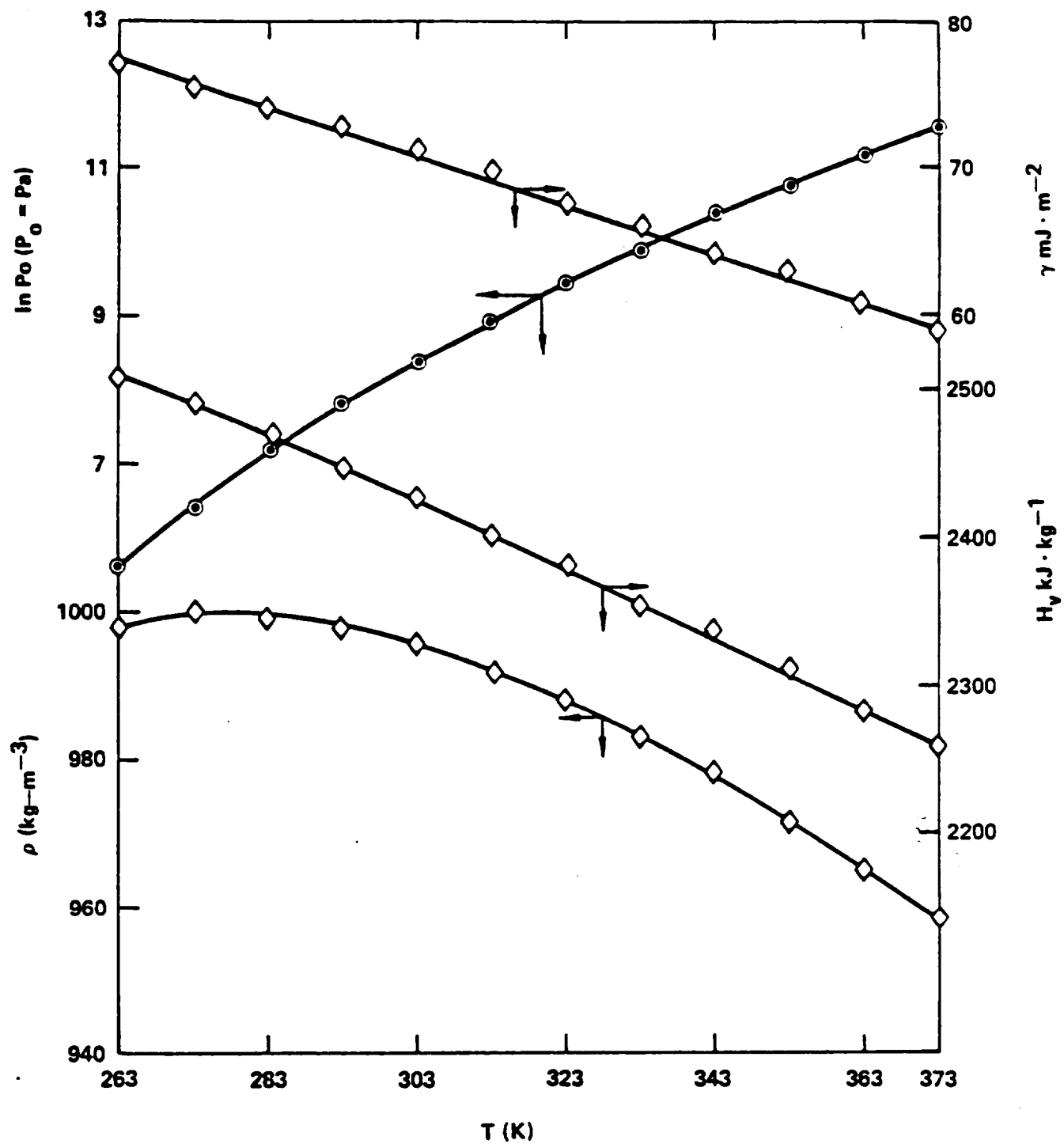


Fig. 1 Temperature dependence of water properties.

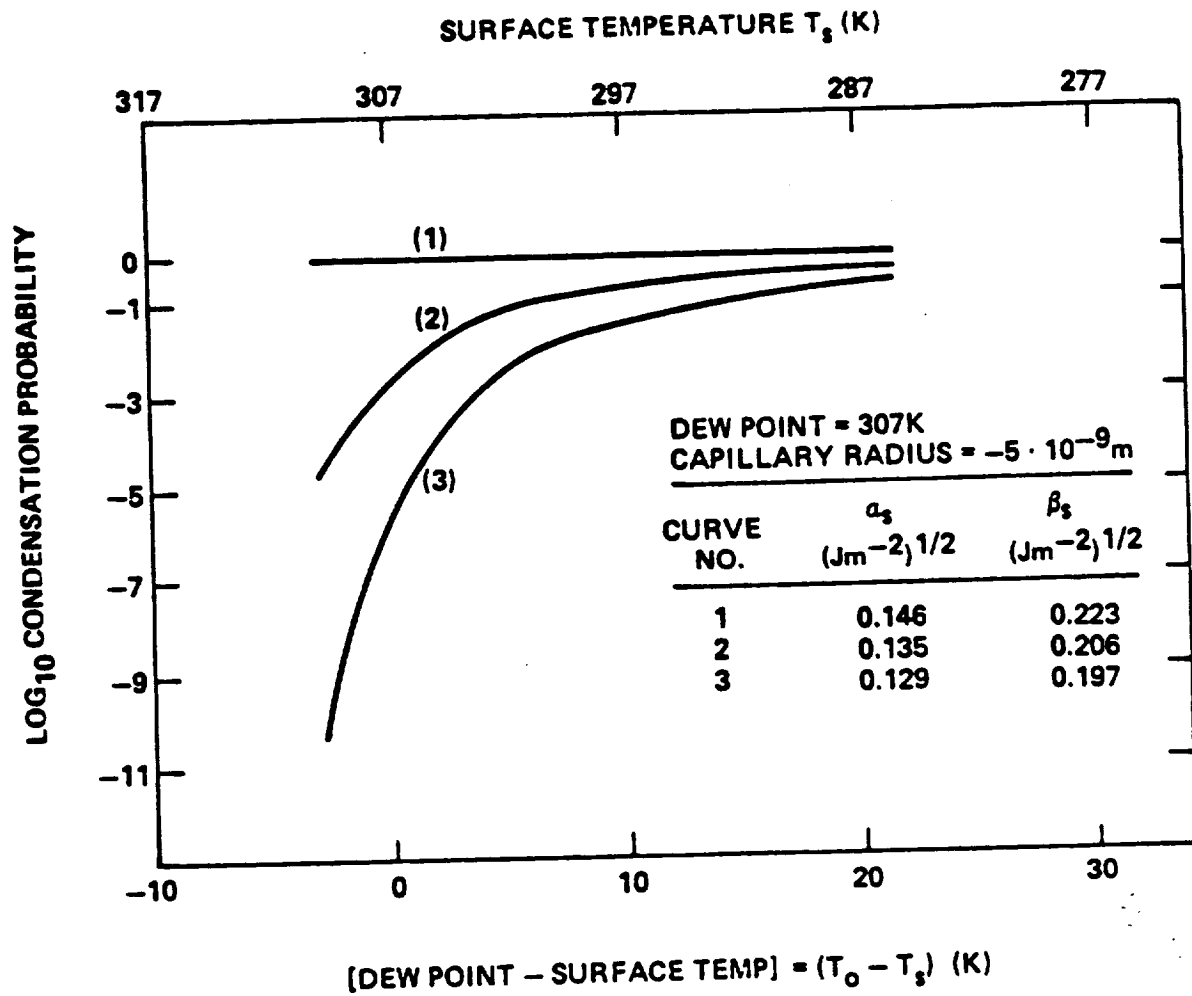


Fig. 2 Condensation probability ($\log_{10} P_c$) vs. surface temperature (T_s) for three values of solid surface energy (α_s , β_s).

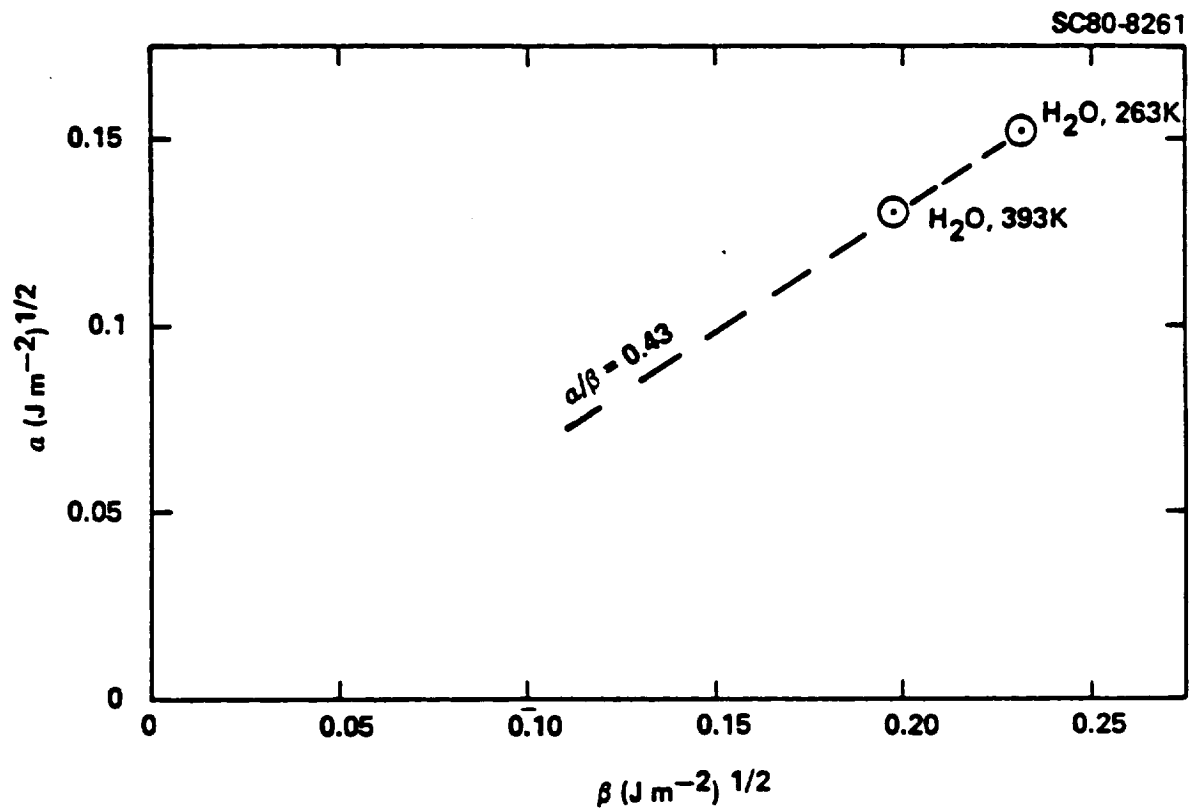


Fig. 3 Surface properties of water plotted on a surface energy diagram of dispersion (α) vs. polar (β) forces.

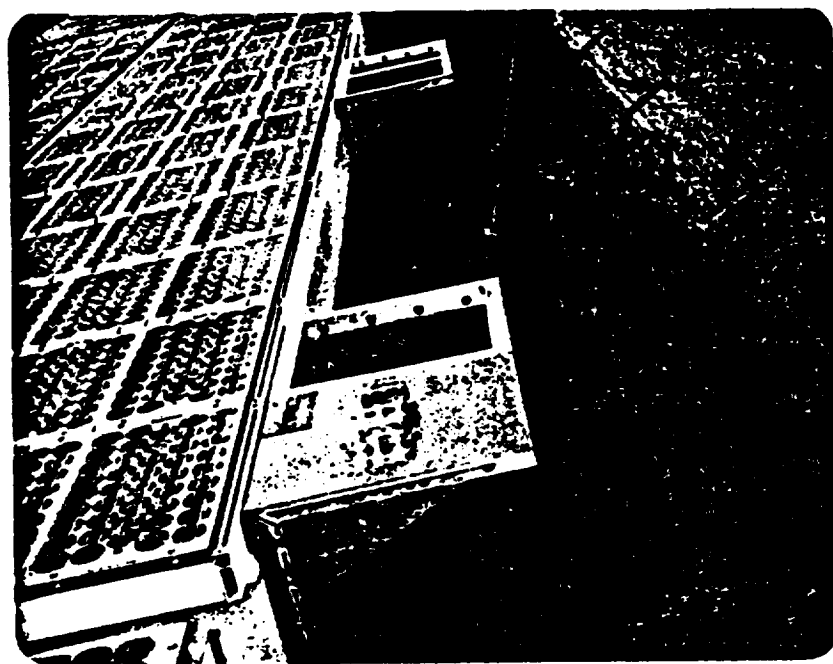
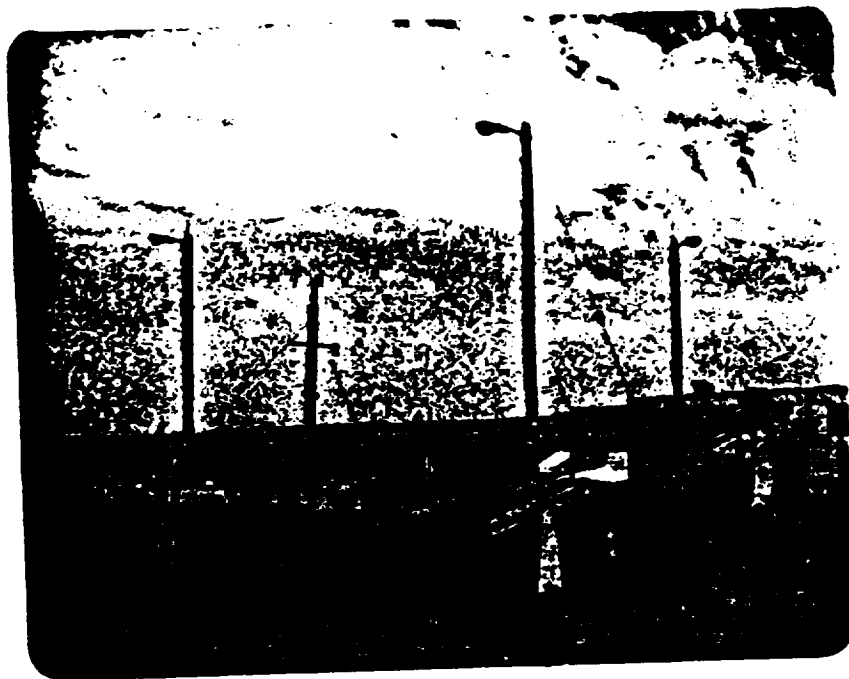


Fig. 4 Photographic view of Mead, Nebraska LSA test site (upper view) and atmospheric corrosion monitors (lower view) installed on rear right portion of array.

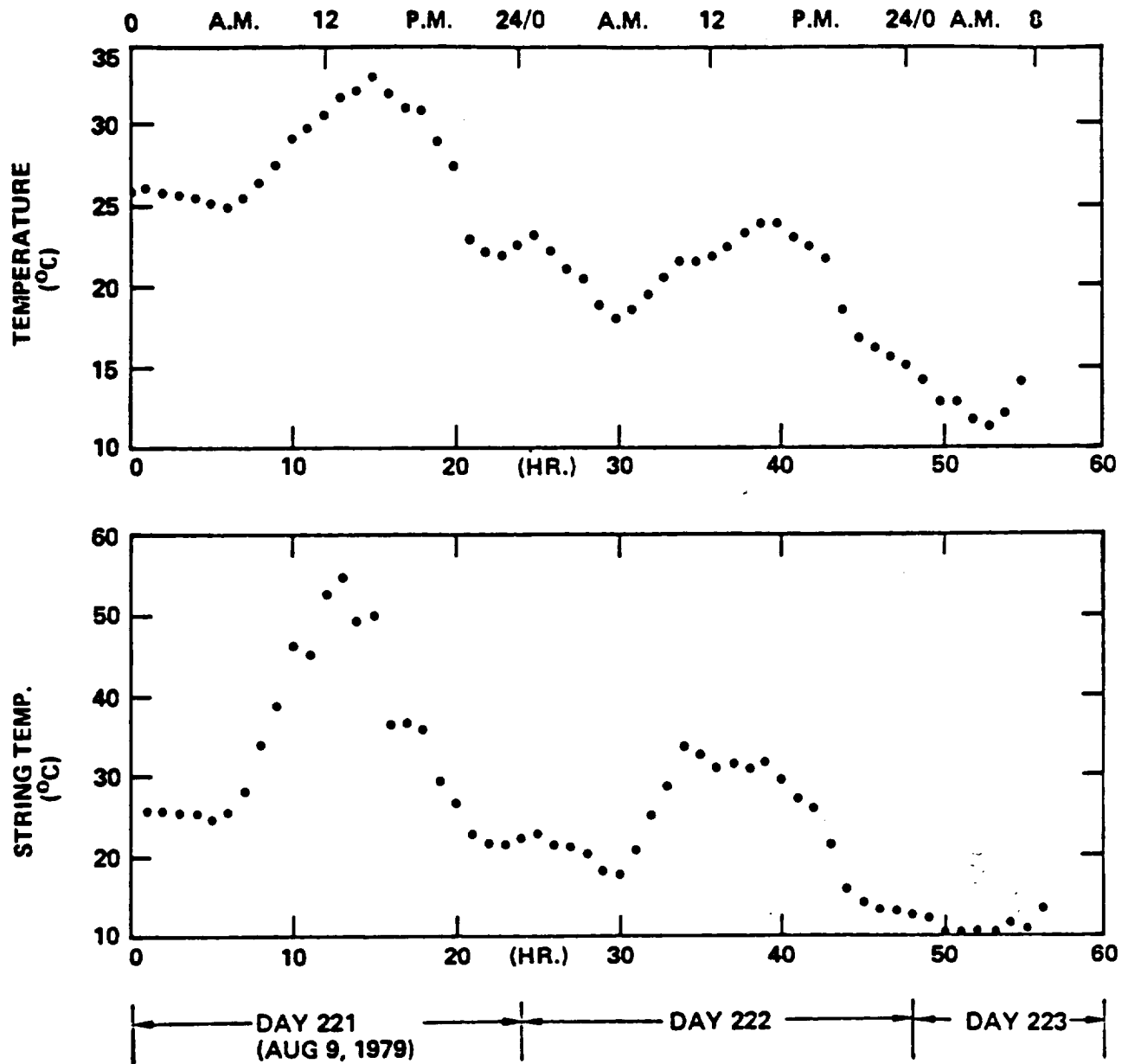


Fig. 5 Comparative Mead Site ambient and solar array string temperatures.

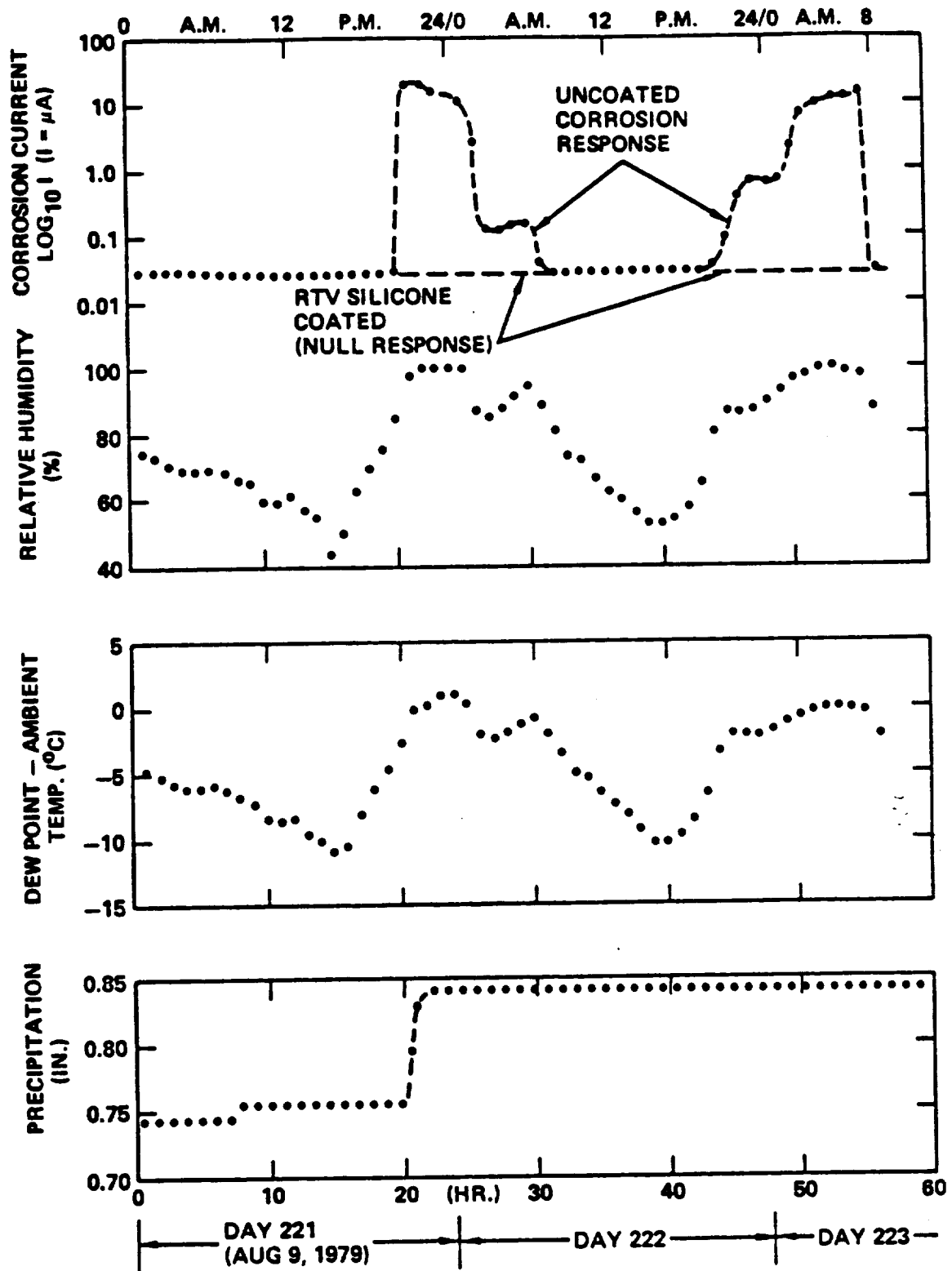


Fig. 6 Corrosion Monitor (upper view) correlation to Mead site moisture and rain climatology.

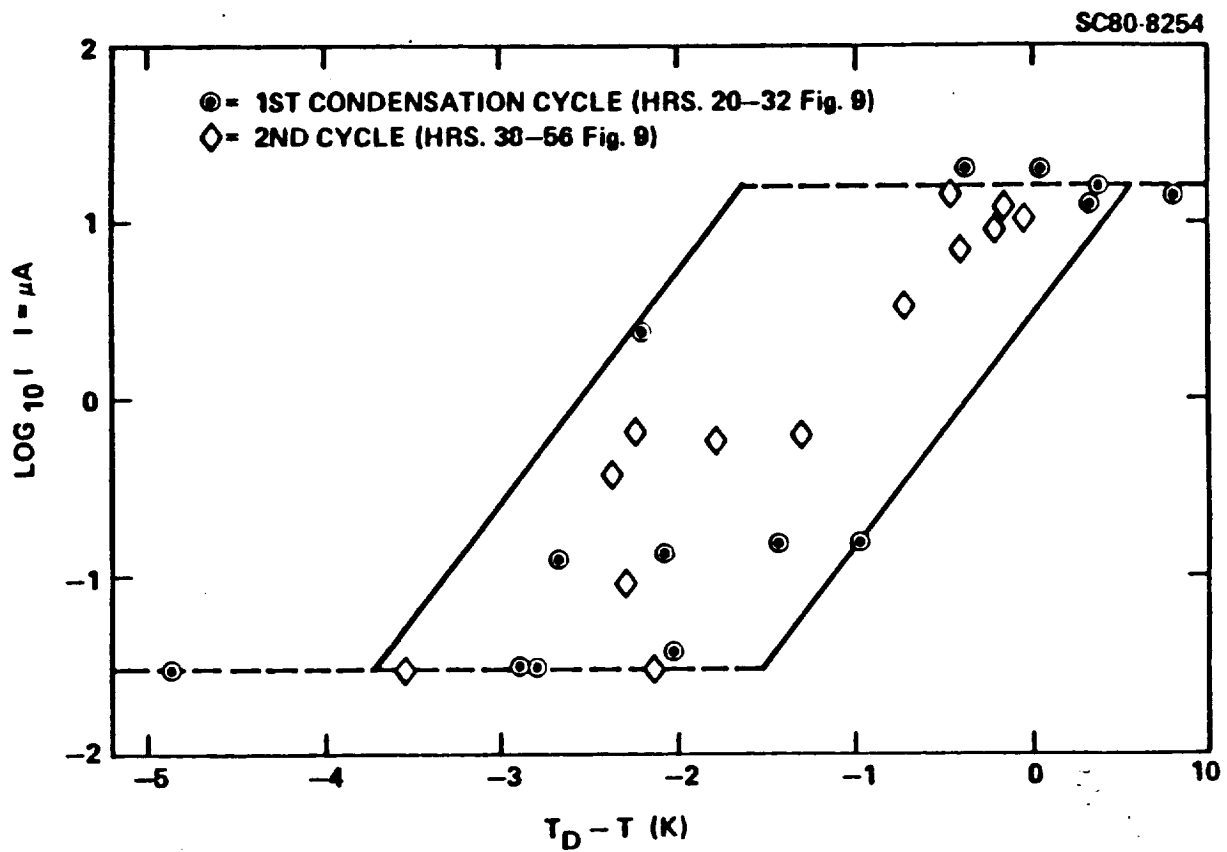


Fig. 7 Corrosion Monitor current (I) vs. moisture super saturation temperature ($T_D - T$).

SC80-8281

SC5106.86AR

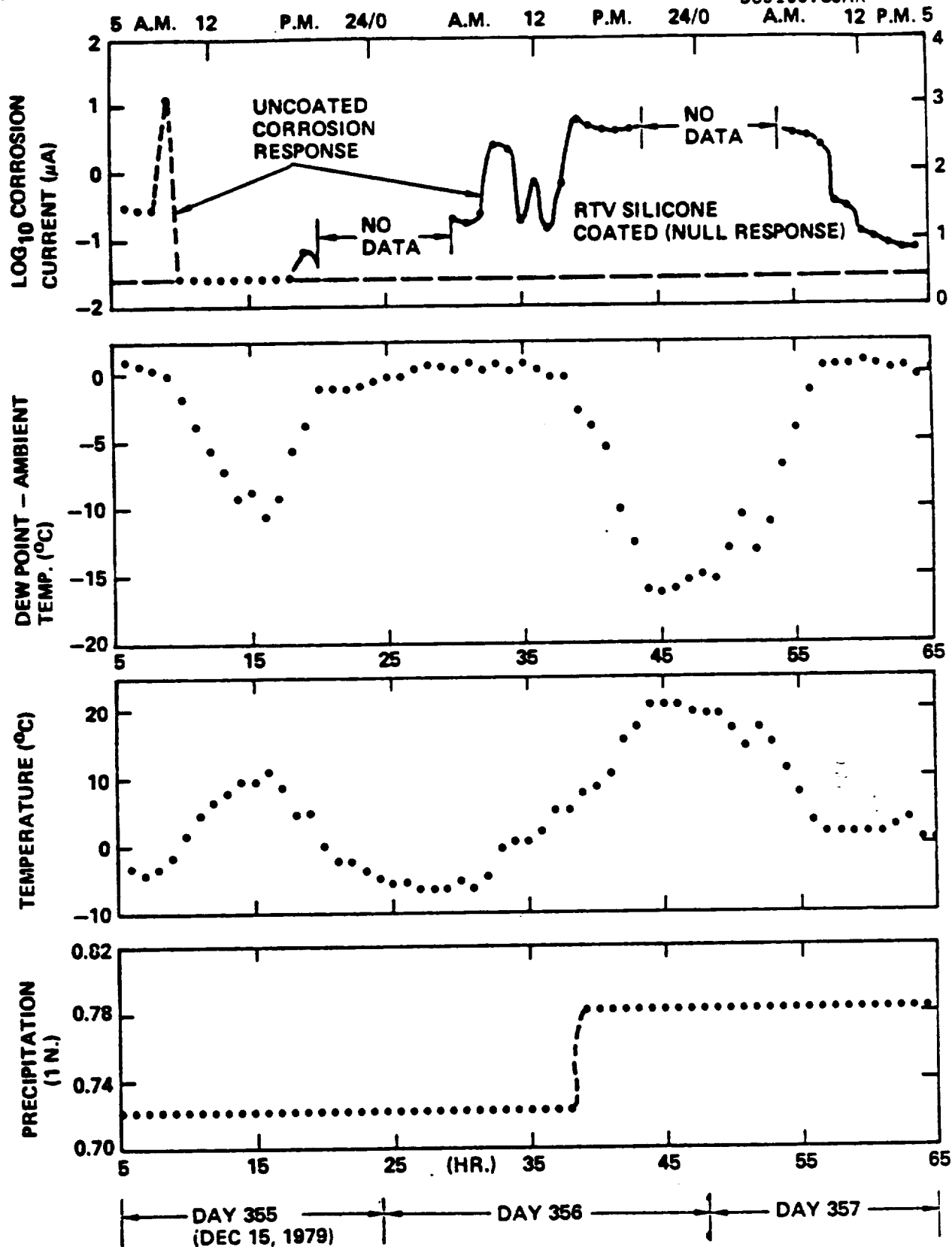


Fig. 8 Corrosion Monitor (upper view) correlation to Mead site climatology for freeze-thaw periods.

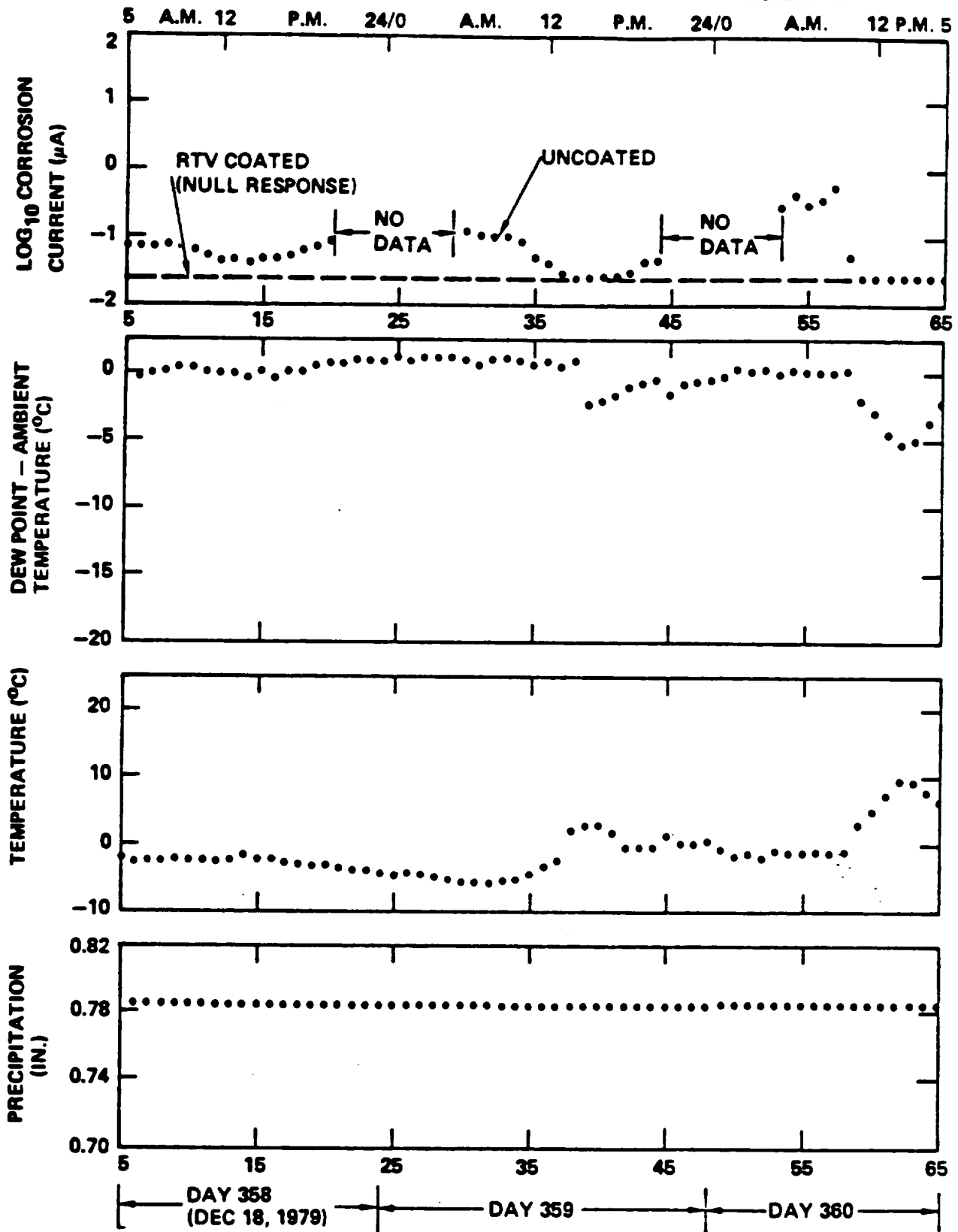


Fig. 9 Further corrosion Monitor (upper view) correlation to Mead site climatology for freeze-thaw periods.

APPENDIX 5

EVALUATION OF SOLAR CELL AND MODULE
PROPERTIES BY AC IMPEDANCE MEASUREMENTS

M. W. Kendig, D. Kaelble and F. Mansfeld
Rockwell International Science Center
Thousand Oaks, CA 91360

ABSTRACT

It has been observed that ac impedance measurements made over a wide frequency range can be used to determine the electrical properties of photovoltaic solar cells. The occurrence of a distribution of time constants for an array of cells indicates that one or more cells deviate significantly from the values of cells which operate properly. In some cases, such deviations have resulted from failure of leads. A model for the ac impedance of solar cells and validating experimental results are presented. AC impedance measurements show promise as an NDE technique for quality control of solar cell arrays.

1.0 INTRODUCTION

Efficient use of photovoltaic cells for power generation requires a minimization of electrical losses which occur as a result of the discharge of photogenerated carriers through a shunt resistance, R_{sh} , in parallel with the photovoltaic and minimization of I^2R_s power losses which result from passage of the photocurrent through leads and interfacial connections characterized by a resistance R_s in series with the photovoltaic cell. This requires maximizing the ratio of R_{sh} to the series resistance, R_s , and defines an optimum power point on the I-V curve for a cell. These electrical properties can change in time as a result of environmental effects. Environmental effects add extraneous impedance elements to the electrical networks representing the cells. For example, corrosion or fatigue cracking of a lead may have little effect on the intrinsic properties of the photovoltaic, but will replace R_s with a more complicated network. The development of hydrated ionic impurities within the encapsulant can form conducting paths in parallel with R_{sh} .

Statistical variation causes each cell of a module to have a different optimum power point on the current-voltage (I-V) characteristic. Therefore, efficient power generation by cells connected in modules also requires a close match of the I-V characteristics of individual cells which comprise the module (1).

In principle, the frequency spectrum of the ac electrical impedance of a photovoltaic cell provides a way for measuring R_s and R_{sh} for individual cells or their distribution and average values

when connected as modules. In general, modules containing cells connected in series have a distribution of R_{sh} and R_s which give rise to a distribution of time constants for the electrical response of the module. The distribution alters the response of the module so as to affect the frequency spectrum of the electrical impedance. To the extent that the electrical impedance elements for each cell relate to their respective I-V curve, a distribution of cell impedance parameters for a module can indicate the degree of dispersion of the I-V response and hence, the match or mismatch of the cells in the module. Similar arguments can be made for parallel connected cells or combination series/parallel connected cells. Therefore, the frequency dependence of the ac impedance of solar cells and solar cell modules contains information on the electrical properties of individual cells, the relative matching or mis-matching of properties of an ensemble of cells within an array, and degradation resulting from failure of leads and breakdown of encapsulated material. These aspects of the ac impedance of photovoltaics have been considered and specific results are reported.

2.0 EXPERIMENTAL DETAILS

Figure 1 shows a schematic for the apparatus used to obtain the frequency dependent ac impedance of a solar cell under controlled bias V_{cell} . Usually the bias was set at 0 volts across the cell ($V_{cell} = 0$) and the measurement made in the dark. An internal oscillator in the Solartron 1174 frequency response analyzer (FRA) provides a sinusoidally varying potential signal $\Delta E(j\omega)$, where $j^2 = -1$ and $\omega = 2\pi f$. This signal is added to the dc bias using a Stonehart BC1200 potentiostat. The typical amplitude of the potential modulation was 0.1 volt. Using the resulting current response, $\Delta I(j\omega)$, the FRA computes the in-phase and out-of-phase components, Z' and Z'' respectively, of the impedance $Z(j\omega)$:

$$Z(j\omega) = Z' + j Z'' \quad . \quad (1)$$

An HP 9825 desk top computer controls the FRA and stores the Z_{in} , Z_{out} , and frequency data. The data can be plotted either as a Bode plot ($\log |Z|$ vs $\log \omega$) or as plot in the complex plane of Z_{out} vs Z_{in} . Here $|Z|$ is the impedance modulus expressed as:

$$|Z| = (Z'^2 + Z''^2)^{1/2} \quad . \quad (2)$$

3.0 RELATIONSHIP OF I-V CHARACTERISTICS TO AC IMPEDANCE

The schematic for the solar cell impedance appears in Fig. 2a. It contains a capacitor, C, parallel shunt resistor, R_{sh} , and parallel diode both in series with the resistor, R_s . The diode represents the non-linear response of the cell. The ac impedance

measurement uses a small amplitude potential modulation so that the diode appears to the ac measurement as a linear element, R_d , in parallel with R_{sh} and C . The element R_d depends, of course, on potential. Under short circuit conditions or zero cell bias ($V_{cell} = 0$), the photo-current, I , becomes virtually independent of potential. Thus R_d approaches infinity and the equivalent impedance of the cell appears as only the parallel elements C and R_{sh} in series with R_s (Fig. 2b). The complex plane plot of the ac impedance of the analog shown in Fig. 2b forms a semicircle in the first quadrant of the complex plane as shown in the schematic (Fig. 2c). As the frequency approaches $\omega = \infty$, the curve intersects the real axis at $Z' = R_s$, and as $\omega \rightarrow 0$, the curve intersects the real axis at $Z_0' = R_{sh} + R_s$. From Z_∞' and Z_0' the values of R_{sh} and R_s can in principle be obtained.

A simple dc measurement will not measure Z' owing to the inherent non-linearity of the cell. Referring to Fig. 3, which illustrates this point, Z' is identical to the slope of the I - V curve at $V_{cell} = 0$, and equals $\Delta E_{ac}/\Delta I_{ac}$. The ratio of applied potential bias to the observed current, $\Delta E_{dc}/\Delta I_{dc}$, defines the dc resistance measurement which, in general, does not equal $\Delta E_{ac}/\Delta I_{ac}$ as shown schematically in Fig. 3.

Since $R_{sh} \gg R_s$, Z_0' provides a very good approximation for R_{sh} under the short circuit condition of $V_{cell} = 0$. However, an accurate determination of R_s requires an impedance measurement to be made under either of two conditions:

1. At a sufficiently high frequency such that the capacitive impedance, $1/\omega C$, is comparable to R_s .
2. At open circuit condition and high generation of the photoexcited state such that $R_d \rightarrow 0$.

In the limit for both of these cases, the impedance of R_s will equal the measured in-phase component of the complex ac impedance. The observed impedance for a two-cell module appears as a Bode plot in Fig. 4 and illustrates these cases. Accurate determination of a R_s in the hundreds of milliohm range requires an impedance measurement at frequencies above 3 MHz for the module. At this frequency $1/\omega C$ equals 100 milliohms. Alternatively, the impedance measurement at open circuit under high photon flux provides the limit of $R_d \rightarrow 0$, for which case the impedance of the cell equals R_s . The impedance for the two cell module in Fig. 4 has been measured at $V_{cell} = V_o$, the open circuit potential, under high illumination. The resulting impedance is frequency independent down to very low frequencies, indicating only resistive behavior as expected when the cell impedance equals R_s .

4.0 INFLUENCE OF DISPERSION IN VALUES FOR R_{sh} ON THE FREQUENCY RESPONSE OF A MODULE

The analog for a single cell shown in Fig. 2b produces a semicircle in the complex plane and can be expressed mathematically as:

$$Z = R_s + \frac{R_{sh}}{1 + j\omega\tau} \quad (3)$$

where $\tau = R_{sh}C$. When an ensemble of cells are connected in series, a distribution of time constants, τ , results due to variations in R_{sh} within the ensemble. The complex plane presentation of Z traces a semicircle with its center below the real axis. A general distribution function of τ defined by Cole and Cole (2) results in the depressed semicircular complex plane plot. In this case the impedance will take the form:

$$Z = R_s + \frac{R_{sh}}{1 + (j\omega\tau)^\beta} \quad (4)$$

A computer program has been written to fit complex plane data to a general semicircle in the complex plane (CIRFIT) (3). From such a procedure R_s , R_{sh} and β can be calculated.

To illustrate the influence of the distribution of parameters on the impedance behavior, Fig. 5 shows an actual distribution of R_{sh} for an ensemble of cells (4). Using this distribution of R_{sh} and assuming that the capacitance of each cell has a constant value of 10 μF /cell a calculation provides the complex impedance/cell for a series connection of the cells. The result of this calculation (points in Fig. 6) was subjected to CIRFIT. The best fit values produce curve #1 in Fig. 6. This result can be compared to the complex plane plot for the case where each of the cells takes the average value $\langle R_{sh} \rangle_{avg}$ (curve #2), or for the case where each cell takes the most probable value (curve #3). The mismatch of cell parameters expressed as R_{sh} has an influence readily detected from the ac impedance spectrum as a depression of the semicircular complex plane plot of the ac impedance.

5.0 A MODEL DESCRIBING THE INFLUENCE OF DEGRADATION ON CELL IMPEDANCE

Figure 7 presents a model in terms of analog impedance elements of an encapsulated cell experiencing environmental degradation. The results of encapsulant degradation can produce conducting paths parallel to the cell. The parallel resistor R_{cp}

schematically represents the parallel paths. This element gives rise to an observed shunt resistance:

$$R_{sh} = \frac{R_{sh}^0 R_{cp}}{R_{cp} + R_{sh}^0} \quad (5)$$

where R_{sh}^0 is the shunt resistance in the absence of any parallel conduction, that is where $R_{cp} \rightarrow \infty$. As R_{cp} decreases, R_{sh} decreases and the semicircular complex plane plot shows a decreased radius. For example the presence of a crack in a cell experiencing high humidity can produce a dramatic decrease in R_{sh} as shown in Fig. 8.

In the case that the leads to the cell fail either by corrosion or fatigue, an interface forms in series with the photovoltaic and produces an effective parallel resistor R_p and capacitor C_p in series with the cell (Fig. 7). This failure mode will show an entirely different frequency response than that observed for the case where parallel conducting paths form. The interconnect failure may result in the resolution of an additional semicircle. For example, a module of N cells connected in series and each having shunt resistance R_{sh} , capacitance C and series resistance R_s , but containing the element R_p, C_p due to the failure of interconnects will have an impedance:

$$Z_{\text{module}} = N \cdot R_s + \frac{N \cdot R_{sh}}{1 + j\omega R_{sh} C} + \frac{R_p}{1 + j\omega R_p C_p} \quad (6)$$

The elements R_p and C_p can have the following interpretation. C_p is the double layer capacitance formed at the interface of a broken interconnect, and R_p is the corrosion resistance at the broken interconnect. A typical impedance spectrum has been calculated for this situation which appears in Fig. 9. For this case $R_p = 10^4$ ohm and $C_p = 10$ μ F assuming the interconnect failure provides an interfacial area of 0.1 cm^2 with typical values of 1000 ohm \cdot cm 2 for the specific corrosion resistance and 100 μ F/cm 2 for the specific capacitance of the interface. As seen in Fig. 9, two partially resolved semicircles result. The larger low frequency semicircle results from the impedance of the failed interconnect and the high frequency semicircle results from the shunt resistance and capacitance of the photovoltaic cells.

6.0 THE OBSERVED INFLUENCE OF DEGRADATION ON CELL IMPEDANCE

Several tests have been carried out in this laboratory and in cooperation with a test program performed by others (5) in which the ac impedance spectra of modules have been observed during their environmentally produced degradation. The results illustrate several

of the points made previously pertaining to the diagnostic capabilities of the ac impedance technique.

The ac impedance spectra of ten modules which had just completed 150 cycles of the Battelle Accelerated Test (6), which is a simulated cyclic hydrothermal exposure test, consisted of either one or two semicircles in the complex plane. Best fit semicircles were obtained using the CIRFIT program. In the case where two semicircles occurred (as illustrated by Fig. 9) the circle fitting program was applied separately to the data in each frequency range. A high frequency intercept of the real axis, R_s , and a low frequency intercept of the real axis, $R_{sh} + R_s$, and $\tan \theta_0$ define each semicircle. Here θ_0 equals $\frac{\pi}{2}(1 - \beta)$, where β is defined in Eq. (4). The larger values of $\tan \theta_0$ correspond to highly depressed semicircles. This results from a broad distribution of time constants produced by a dispersion of cell parameters or introduction of extraneous impedance elements into the module.

The two types of complex plane plots observed for these modules appear in Figs. 10 and 11. Figure 10 shows the complex plane plot for the impedance of module #3408 which contains one depressed semicircle. In the complex plane plot for the impedance of #3191 (Fig. 11) two semicircles are resolved. A tabulation of data for the ten modules appears in Table 1. Three modules (#3191, #3822 and #4028) show two well resolved semicircles. The others exhibited only one semicircle. With one exception (#3663), the modules responding with a single semicircle in the complex plane plot yield apparent negative R_s . This "system response" results from the skewness of the data to which a best-fit semicircle was forced. When a second time constant begins to resolve, the fitted R_s increases. This happens to be the case for #3663 and indicates the onset of resolution of a second time constant since its fitted value for R_s is positive and equals 737 ohms (Table 1). Significantly, the modules #3191, #3822, #4028 and #3663 which showed early resolution or partial resolution (as the case of #3663) of two time constants at 150 cycles showed early power drops >10% at 360 cycles (5). All plots containing a single semicircle exhibit a significant distribution of time constants as judged by the large $\tan \theta_0$. In time all modules showed open circuit behavior at 95°C which is consistent with the development of highly skewed semicircles at the early times of 150 cycles. These results can be interpreted by the model described in the previous section for which interconnect failures can add additional, resolved time constants (Fig. 9).

In addition to causing interconnect failure, hydrothermal aging can also produce parallel conducting paths, R^{-1} (Fig. 7) within encapsulated photovoltaic modules. Two mini-modules^{CP} DE543 and DE243 each containing two cells in series and encapsulated as described in Table 2 were exposed to hydrothermal stress. The glass/aluminum backed module showed very little weight gain during extended hydrothermal aging at 60°C and 100% RH. However, after an initial

Table 1
Circle-Fit Parameters for Ten Modules

Module No.	Circle Fit Parameters for High Frequency Semicircle			Circle Fit Parameters for Low Frequency Semicircle		
	R_s Ω	R_{sh} $10^3\Omega$	$\tan \theta_0$	R_s $10^3\Omega$	R_{sh} $10^3\Omega$	$\tan \theta_0$
3191	-62	9.7	0.200	2.8	3.0	0.019
3546	-24	10.8	0.155	n.a.	n.a.	n.a.
3663	737	5.3	0.178	n.a.	n.a.	n.a.
3822	-83	10.4	0.339	9.7	48.2	0.025
3723	-102	9.1	0.237	n.a.	n.a.	n.a.
4195	-173	16.7	0.536	n.a.	n.a.	n.a.
4028	-181	23.0	0.326	7.5	38.0	0.413
3408	-107	7.2	0.251	n.a.	n.a.	n.a.
3077	-334	14.6	0.483	n.a.	n.a.	n.a.
3934	-211	19.7	0.288	n.a.	n.a.	n.a.

n.a.: Only one relaxation time

Table 2
Materials Description of Block 4 Modules
Utilized in Moisture Diffusion Effects Test

Module No.	DE 243	DE 543
Materials (from front to back)	Glass	Tedlar film
	Clear EVA*	Clear EVA*
	Solar cell	Solar cell
	White EVA*	White EVA*
	Crane glass cloth	Crane glass cloth
	Al foil	Super Durlux (fiberboard)
		White EVA*

*EVA = ethylene-vinylacetate copolymer encapsulant.

decrease in shunt resistance during 77 day exposure to 60°C and 100% RH, the shunt resistance of the DE243 module returned to its initial value. DE543, the fiberboard backed module, showed a much different response. With exposure to 60°C, 100% RH, this module showed a somewhat reversible uptake of water, but a large irreversible decrease in shunt resistance. A crack was artificially formed in the DE543 module during a hydrothermal stress cycle which resulted in a sharp, partially reversible decrease in shunt resistance.

The model presented for the ac impedance analog of a photovoltaic cell or module (Fig. 7) includes a resistor, R_{cp} , in parallel with the photovoltaic. R_{cp} represents the presence of externally conducting paths which short circuit the photovoltaic. Its presence contributes to the observed shunt resistance of the cell according to Eq. (5). R_{sh}^0 in Eq. (5) is the shunt resistance for the device in the absence of any degradation which would cause the onset of parallel conducting paths. For the mini-modules DE243 and DE543 R_{sh}^0 has been taken as the initially observed shunt resistance for the respective dried cell. From the value of R_{sh}^0 and Eq. (5), the conductivity of the parallel conducting paths, $1/R_{cp}$, has been calculated for DE543 and DE243. Figure 12 shows a plot of $\log(1/R_{cp})$ vs time in days. For module DE543, the conductivity, R_{cp}^{-1} , increases irreversibly for each hydrothermal cycle and shows a sharp increase when one of its cells was intentionally cracked during hydrothermal treatment. The glass/aluminum cell DE243 shows an initial increase in conductivity within the first few hours for treatment but reverses thereafter. For DE243 the initial conductivity transient results from thermal processes which eventually decay with long term treatment.

For DE543 the conducting paths can be considered to result from the presence of transported and condensed aqueous phase in voids at the edges and cracks of the encapsulated cells. A volume, V , for these voids may be calculated with knowledge of cell thickness, d , and volume conductivity of the aqueous phase, σ :

$$V = d_{cell}^2 / \sigma R_{cp}$$

A cell thickness of 0.0254 cm and the 70 μ mho/cm conductivity of carbon dioxide saturated water requires a void volume of 9 cm³ to produce 1 mho of parallel path conductivity. Therefore DE543 shows void volumes of 0.01 cm³ to 0.1 cm³. Clearly the existence of ionic impurities in the aqueous phase would substantially decrease this estimate. Assuming the above estimates of void volume to be correct, the further development of ionic concentrations on the order of 0.1 M within the 0.1 cm³ void will produce an R_{cp} of approximately 0.6 ohms. This will dominate the shunt resistance and most certainly indicates cell failure. Hence, a crack defined by this model will not remain benign if ionic impurities concentrate within its void volume.

7.0 SUMMARY AND CONCLUSIONS

A review of the ac impedance of photovoltaic cells and modules has been presented and an assessment made of the use of impedance analysis as a diagnostic, non-destructive evaluation technique for the degradation of photovoltaic modules. Results of this study show that statistical variations in R_{sh} produce a significant change in the ac impedance for a module resulting in a depression of the semicircular complex plane plot. Furthermore, the frequency dependence of the ac impedance of photovoltaic modules can diagnose the mode of failure. Decreases in R_{sh} indicate the development of parallel conducting paths due to encapsulant degradation or cell cracking in the presence of hydrothermal stress. On the other hand, contact failure places an additional impedance network with a different time constant in series with the photovoltaic cells. Observation of a low frequency relaxation can provide an early warning of interconnect failure.

Specific results for mini-modules undergoing hydrothermal stress have shown that parallel paths which develop in fiber board backed, EVA encapsulated modules have a low conductivity and remain low ($1/R_{cp} < 10^{-2}$ mho), but could produce failure if ionic impurities would concentrate in the apparent void space.

AC impedance provides an important tool for analyzing photovoltaic degradation. It gives quantitative information in terms of R_{sh} which could be measured using relatively unsophisticated equipment. More elaborate equipment can provide the frequency dependence of the ac impedance which diagnoses modes of failure in certain cases.

8.0 ACKNOWLEDGEMENTS

This work was performed under Contract #954739 for the Jet Propulsion Laboratory. The authors wish to acknowledge the impedance measurements made by G. Lindberg.

9.0 REFERENCES

- (1.) L. L. Bucarelli, Jr., Solar Energy 23, 277-288 (1979).
- (2.) K. S. Cole and R. H. Cole, J. Chem. Phys. 9, 341(1949).
- (3.) D. H. Kaelble, F. B. Mansfield, M. Kendig and C. Leung, "Study Program for Encapsulation Materials Interface for Low-Cost Solar Array," Annual Report to JPL, SC5106.104AR, February 1981.
- (4.) Jet Propulsion Laboratory Workshop Proceedings: "Photovoltaic Circuit Design Optimization," March 31, 1980.
- (5.) P. Frickland, JPL, personal communication, December 1981.
- (6.) G. B. Gains, et al, "Final Report; Development of Accelerated Test Design for Predicting Service Life for the Solar Array at Mead, Nebraska," DOE-JPL 954319-79/13 (1979).

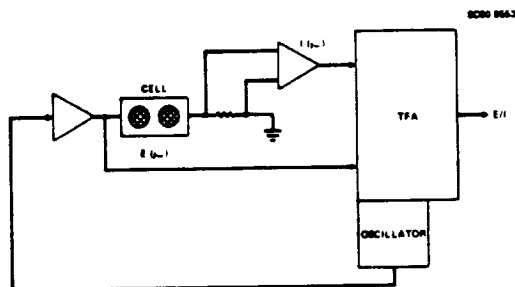


Fig. 1 Schematic of the apparatus for measuring the ac impedance of a photovoltaic

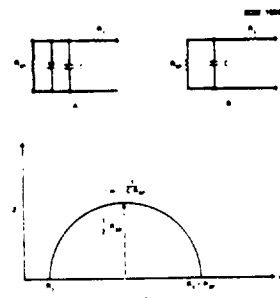


Fig. 2 A. Electrical schematic of a solar cell
B. Linearization of the solar cell response.
C. Schematic complex plane impedance plot.

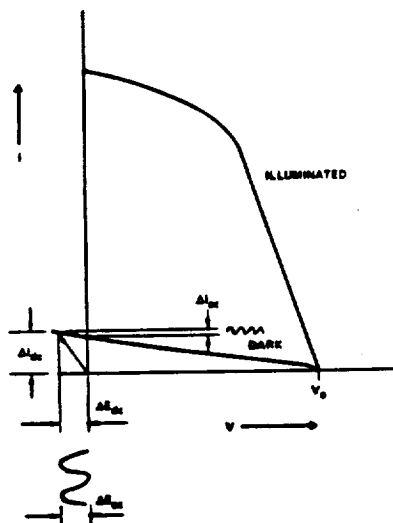


Fig. 3 Schematic showing the relationship of the I-V response to the ac impedance.

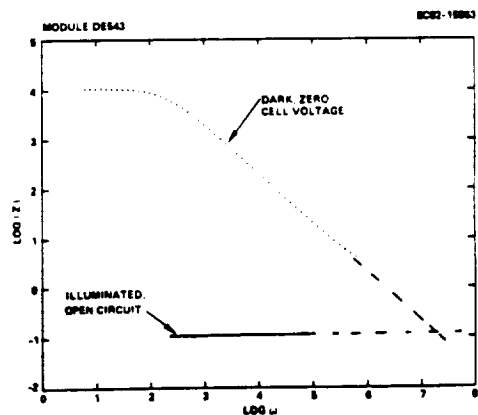


Fig. 4 Bode plot for module DE543 under dark and illuminated conditions.

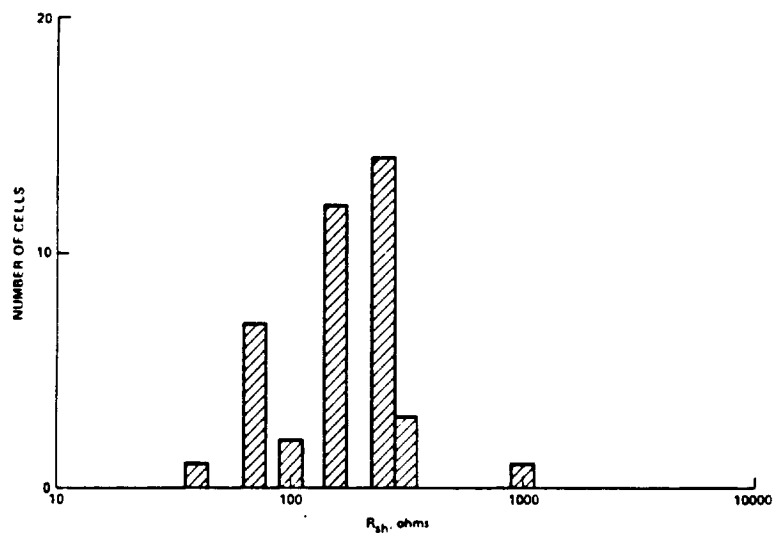


Fig. 5 Distribution of R_{sh} in a series array.

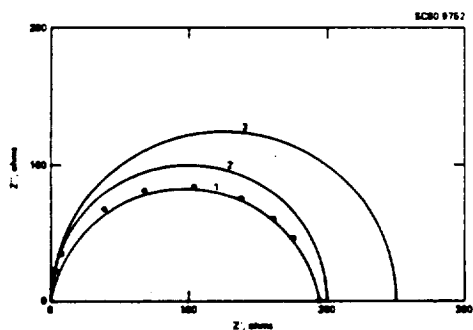


Fig. 6 Ac impedance of a series connection of the cells having the distribution in Fig. 5 (curve #1) as compared to the case where all cells have the average R_{sh} (curve #2) or the most probable R_{sh} (curve #3).

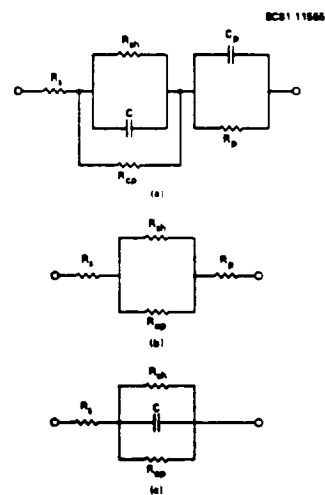


Fig. 7 Model of a cell undergoing environmental damage.

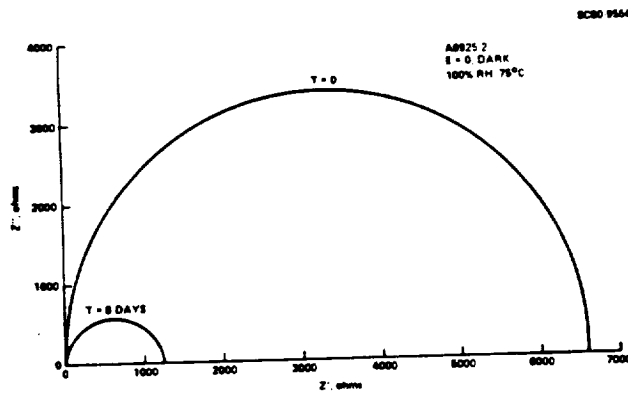


Fig. 8 Ac impedance of a cracked cell.

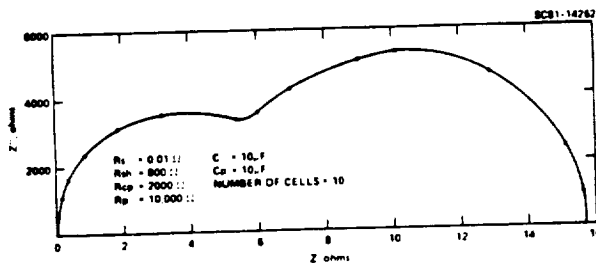


Fig. 9 Calculated ac impedance for a series of cells containing an interconnect failure.

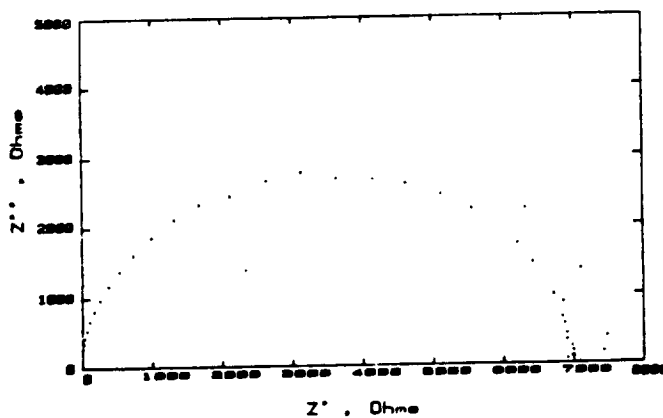


Fig. 10 Complex plane impedance for module #3408 at 150 cycles of the Battelle accelerated test.

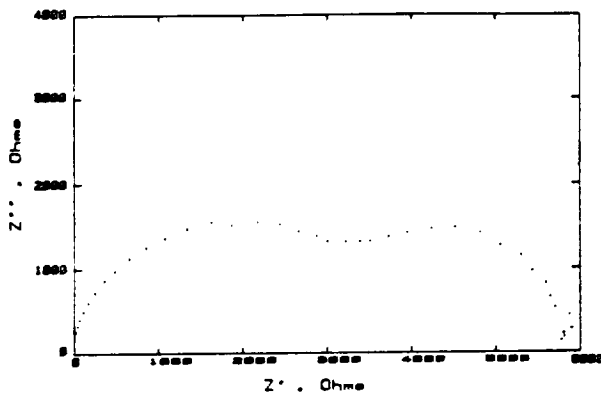


Fig. 11 Complex plane impedance for module #3191 at 150 cycles of the Battelle accelerated test.

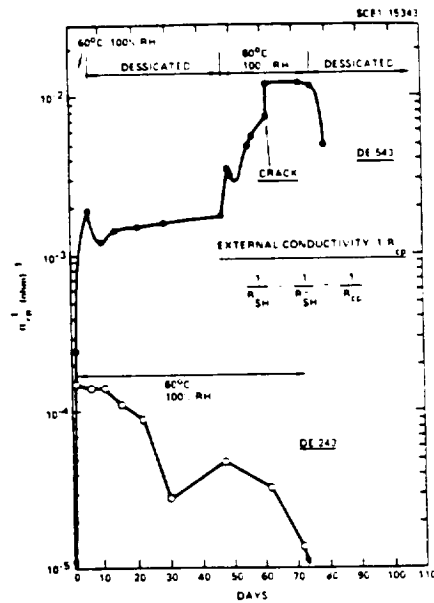


Fig. 12 The influence of hydrothermal stress on R_{CD}^{-1} for two mini modules.

